Fakultät für Maschinenwesen
Lehrstuhl für Angewandte Mechanik

Validation of a Pushbelt Variator Model –
Insights into a non-smooth Multibody System

Kilian Bartimäus Wolfgang Grundl

Vollständiger Abdruck der von der Fakultät für Maschinenwesen der Technischen Universität München zur Erlangung des akademischen Grades eines

Doktor-Ingenieurs (Dr.-Ing.)

genehmigten Dissertation.

Vorsitzender: Univ.-Prof. dr. ir. Daniel J. Rixen

Prüfer der Dissertation:

1. Univ.-Prof. Dr.-Ing. Dr.-Ing. habil. Heinz Ulbrich, i.R.
2. Univ.-Prof. Carlo L. Bottasso, Ph. D.

Die Dissertation wurde am 20. Mai 2015 bei der Technischen Universität München eingereicht und durch die Fakultät für Maschinenwesen am 25. September 2015 angenommen.

Acknowledgement

The following thesis is the result of the scientific work I did over the last four years as a research assistant at the Institute of Applied Mechanics of the Technische Universität München, which was funded by Bosch Transmission Technology B.V.
During the project I got supported by many people, without whom this work would not have been possible.

First of all I want to thank my supervisor professor Ulbrich for his guidance and interest in my research – even after your retirement. You gave me the opportunity to work in a very fruitful environment on an interesting project. Thus, I had the chance to develop my own ideas.
I am also very grateful to his successor professor Rixen. Not only did you give me the freedom to proceed with my research directly at the institute but also you were actively interested in the progress. Thank you for your valuable advice!

Besides I was very lucky to work with the experts of Bosch in Tilburg. Semih Yildiz, Arie van der Velde, Joost Schnackers, Minh-Duc Tran, Paul Faes, Lichao Pan and all the other colleagues of ENA helped me to better understand the pushbelt. Even more: you made it easy for me to work and live abroad in a wonderful atmosphere. I am very thankful for the support I experienced and the friends I found there.

A positive working climate is crucial for the success of such a project and I found this working climate at the institute in Munich. I enjoyed the interesting discussions about scientific challenges, modeling and implementation but also to have a laugh once in a while and to balance work and life. Specifically, I want to name Thorsten Schindler: Thank you for your intensive support, ideas and critical review. And thank you Thomas Cebulla, Semih Yildiz, Lichao Pan and my brother Serafin for further proof-reading.

Finally I want to express my gratitude towards those who were not connected to my research at all but supported me nevertheless. To my friends who understood that I could not always find the time. And last but not least to my family, my parents Anne and Wolfgang and my siblings Eva, Serafin and Lioba: Thank you very much!

Munich, October 2015 *Kilian Grundl*

Abstract

Continuously variable transmissions (CVTs) enable optimal control of the drivetrain and thereby reduce fuel consumption. In addition they increase comfort in stop-and-go drive states. CVTs are therefore an ideal solution for modern car concepts.
Previous work developed detailed nonlinear multibody models of its system's dynamic. This thesis discusses the enhancement and validation of these pushbelt CVT models.
For the efficient simulation of the whole model the dynamics of its parts, their interactions and the numerical treatment are discussed. New models for the ring dynamics and for the contact between curved sheaves and curved element flanks, an identification method for the element's longitudinal contact stiffness, a physical based tracking law as well as methods for computing time reduction improve and enhance the system.
The discussion of numerical aspects covers the number of simulated elements, the usage of non-smooth dynamics and a comparison of different ring models. The chapter physical aspects covers parameter uncertainties, especially the contact parameters for geometry, stiffness and friction. A sensitivity analysis of the system is performed. It yields the identification of these parameters. Furthermore, optimization possibilities are gained.
Local forces between elements, rings and pulleys correlate on a qualitative and quantitative level with measurements. The kinematics in the arcs in terms of spiral running and element pitch angle fit to available data as well. Furthermore, simulation results yield global values, i.e. thrust ratio, efficiency, slip-curves and an endplay tolerance, that match to measurements.
Overall the validation demonstrates the applicability of the model for well identified parameters for stationary and instationary phenomena and its fit – qualitatively as well as quantitatively.

Zusammenfassung

Stufenlose Getriebe (CVTs) ermöglichen die optimale Regelung des Antriebsstranges und tragen damit zur Reduktion des Treibstoffverbrauchs bei. Weiterhin erhöhen sie den Komfort im Stop-and-go-Verkehr. CVTs sind daher eine ideale Lösung für moderne Automobilkonzepte. Frühere Arbeiten entwickelten ein detailliertes nichtlineares Mehrkörpermodell der Systemdynamik eines Schubgliederbandgetriebes. Diese Dissertation diskutiert die Weiterentwicklung sowie die Validierung dieses Modells.
Zur effizienten Simulation des gesamten Systems wird die Dynamik der einzelnen Komponenten, deren Interaktionen sowie die numerische Behandlung diskutiert. Neue Modelle der Ringdynamik und für den Kontakt zwischen balligen Scheiben und balligen Elementflanken, eine Methode zur Identifizierung der Längssteifigkeit der Elemente, ein physikalisch begründetes „Tracking“-Gesetz sowie verschiedene Methoden zur Reduzierung der Berechnungszeiten verbessern und erweitern das Gesamtsystem.
Die Diskussion numerischer Aspekte des Modells beinhaltet die Anzahl der simulierten Elemente, die Anwendung nicht-glatter Kontaktgesetze und den Vergleich verschiedener Ringmodelle. Das Kapitel „Physikalische Aspekte“ behandelt Parameterungenauigkeiten – insbesondere die der Kontaktparameter für Geometrie, Steifigkeit und Reibung. Die Sensitivität des Modells gegenüber diesen wird untersucht. Diese Untersuchung trägt zur Identifikation der Parameter bei und zeigt Optimierungsmöglichkeiten auf.
Lokale Kräfte aus der Simulation zwischen Elementen, Ringen und Scheiben stimmen qualitativ und quantitativ mit Messungen überein. Die Kinematik in den Bögen bezüglich dem Spirallauf und der Elementneigung passen zu vorhandenen Messdaten. Weiterhin werden aus den Simulationen globale Daten gewonnen. Das Kraftverhältnis, die Effizienz, „Schlupfkurven“ und die Toleranz gegenüber Spiel im Band gleichen einander in Simulation und Messung. Insgesamt zeigt die Validierung die Anwendbarkeit des Modells für stationäre wie instationäre Lastfälle. Es können qualitative sowie quantitative Aussagen über das System getroffen werden, die sich in Experimenten bestätigen lassen.

Table of Contents

List of Abbreviations

ALE arbitrary Lagrangian-Eulerian
ANCF absolute nodal coordinate formulation

BC basis case
BTT Bosch Transmission Technology B.V.

COG center of gravity
CPU central processing unit
CVT continuously variable transmission

DAF Doorne Automobiel Fabriek
DOF degree of freedom

EIN element impact noise
EOM equation of motion

FE finite element
FEM finite element method
FFR floating frame of reference
FFT fast Fourier transformation

LCP linear complementarity problem
LRVM large rotation vector method
LS lower strand

MBS multibody system
MBSim multibody simulator
MED medium

NVH noise, vibration and harshness

OD overdrive
OEP operational endplay

PRI primary arc

RCM redundant coordinate method
RE rocking-edge
RPM revolutions per minute

SEC secondary arc
SR speed ratio

TAP turnaround point
TR thrust ratio

UD underdrive
US upper strand

wrt. with respect to

List of Figures

List of Tables

1 Introduction

In 1958 the first Doorne Automobiel Fabriek (DAF)-car with a *Variomatic* was released. Its rubber belt was replaced with a steel pushbelt in the 1970s and the system was then called *Transmatic* which later became the continuously variable transmission (CVT). In 1985 mass production started and the pushbelt has been enhanced over the years.
The share of CVTs on the transmission market will increase from 6 % in 2012 to up to 14 % in 2020 [31]. The continuously ratio coverage enables to operate the engine in an optimal point. In combination with a downsizing of the engine the reduction of fuel consumption in the overall drivetrain can be reached. According to [64] passenger cars create about 10 % of the world wide greenhouse gases. The CVT-system can therefore help to reduce the CO_2 footprint. The increasing urbanization ([42]) will lead to more stop-and-go drive states in modern cities. A CVT avoids discrete shifting, which improves the comfort of the driver.
This analysis shows that the pushbelt CVT is an ideal solution for modern car concepts. A further improvement of the system can increase its efficiency and robustness. Recent research optimizes the system control as well as the tribology. Reliable models, which enable deeper insights into the system, are necessary. They form the basis for design-optimization.
Various models cover particular aspects of the pushbelt CVT dynamics. Restrictive assumptions limit their scope. No all-encompassing model has been derived and validated. The correct representation of the full nonlinear dynamics for transient maneuvers covering spatial motion was the goal of a joint research project between the Institute of Applied Mechanics of the Technische Universität München and Bosch Transmission Technology B.V. (BTT)[1]. Preceding PhD-theses [6, 25, 54, 9] form the basis for this contribution. The pushbelt CVT is represented as a multibody system (MBS) modeling the dynamics and interactions of its parts separately. Detailed output of the simulations allow for deep analysis of the inner kinematics and kinetics.
Each model demands for validation to prove its significance. This work concerns itself with the analysis of the chosen approach. The single submodels are discussed of which some are enhanced. Furthermore, the overall models are analyzed in different aspects. Due to the approximation of the models with computer technology, the numerical influences are a crucial factor. Parameter uncertainties limit the range of informative value of the model. A sensitivity study yields this range. It furthermore demonstrates the analysis possibilities of the model. On the one hand the inner mechanics can be analyzed. On the other hand global measures and transient dynamics can be used for future optimization. For this goal, the validation of the model is necessary.

This chapter introduces the geometric setup and the working principle of a pushbelt CVT. A current research overview follows together with literature remarks concerning MBSs. The most important equations are given. Prior work, on which this thesis relies on, is finally covered in more detail. The overview about the complete thesis concludes this chapter.

[1] formerly “Van Doorne Transmissie“

1.1 Geometric Setup and Working Principle

Figure 1.1: Pushbelt CVT ©BTT. It shows the two pulleys – each with a loose and a fixed sheave – and the pushbelt consisting of two rings and about 400 steel elements.

This work analyzes the dynamics of a pushbelt CVT as it is depicted in Figure 1.1. In the following the geometric setup is described. Thus, the main working principles are explained using basic modeling ideas of MBSs. The notions valid for this thesis are introduced to serve as a basis for a general and clear description.
Besides other works, e.g. [13, 26, 6], the understanding of the working principle can be supported by three dimensional visualizations, e.g. videos or animations. These type of media cannot be included here. Two examples – besides many more which can be found in the world wide web – are:

- Animation of BTT, the manufacturer of the pushbelt [17]
- Animation of DrivelineNEWS.com [15]

Figure 1.2 shows an overview about the general kinematics of the system with the most important external and internal forces. A torque M is transmitted from a *primary* pulley (Index P), i.e. the driving side, to a *secondary* pulley (Index S), i.e. the driven side. The pulleys have the axle distance d_A. The respective wrapped angles are called primary arc (PRI) and secondary arc (SEC). A pushbelt is clamped in both pulleys. It consists of about 400 elements that are guided by two ring-packages or rings, each consisting of about 6 - 12 layers.
The ratio between the angular speeds ω_P of the primary and ω_S of the secondary pulley

$$i_S = \frac{\omega_P}{\omega_S} \tag{1.1}$$

is called speed ratio (SR). The underdrive (UD) configuration is defined by $i_S > 1$ and the overdrive (OD) configuration by $i_S < 1$. Ratios for $i_S \approx 1$ are referred as medium (MED) configuration.
The SR is controlled by the ratio of the two clamping forces, i.e. the thrust ratio (TR),

$$i_F = \frac{F_P}{F_S} \tag{1.2}$$

and due to the V-shape of the pulley-sheaves and the element flanks respectively.
A geometric ratio

$$i_{g*} = \frac{r_{S*}}{r_{P*}} \tag{1.3}$$

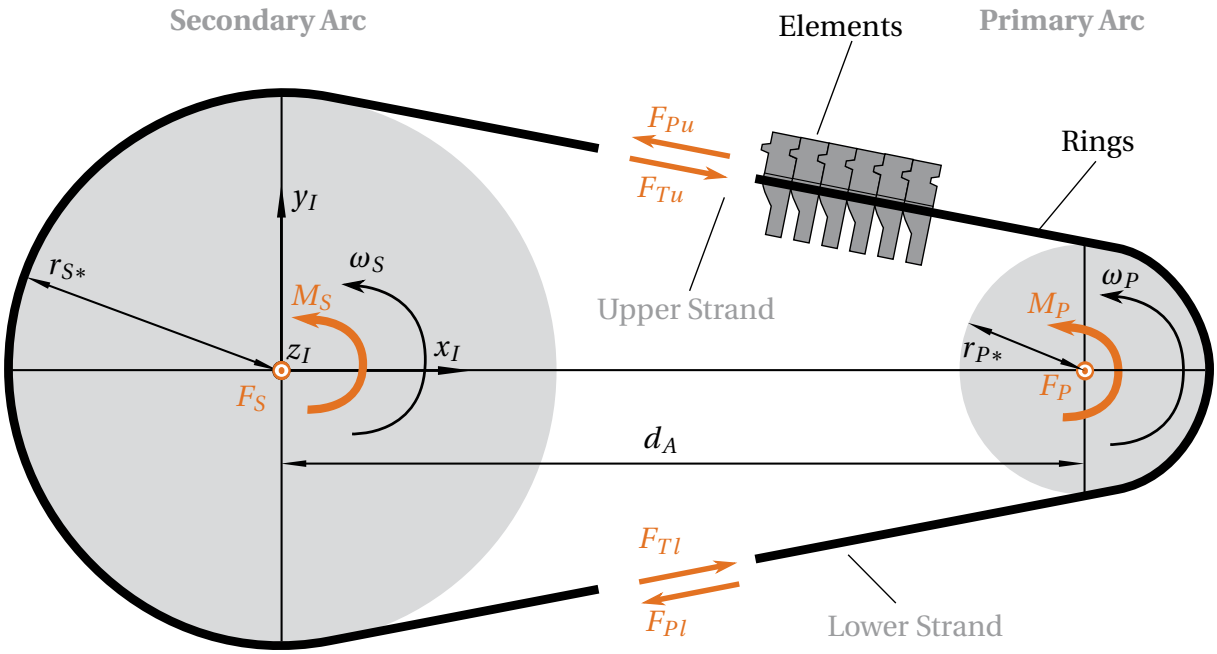

Figure 1.2: Overview of the pushbelt CVT with the most important external and internal forces

is defined as the ratio between the SEC-radius r_{S*} and the PRI-radius r_{P*}. Different measures for the radii are possible using either ring or element kinematics. On each pulley the forces are applied due to hydraulic pressure on the respective loose sheave, which can move along the shaft. The other sheave of the pulley is fixed on the shaft.

Along the belt four main parts are separated. Within the upper strand (US) (Index u) and lower strand (LS) (Index l) the forces are transmitted with two dominating effects. On the one hand push-forces (F_{Pu} and F_{Pl}) are active between the elements. On the other hand tension forces within the rings (F_{Tu} and F_{Tl}) contribute to the overall equilibrium. The push-forces between the elements do contribute in the torque transmission in case of $F_{Pu} > F_{Pl}$, which is the intended behavior. In case of $F_{Pu} < F_{Pl}$, the push-forces work against the torque as the difference in ring-tensions contribute more than the applied torque. In case of $F_{Pu} = F_{Pl}$ the *transition torque* is applied to the system. The strand with the higher push-force is called push-strand. Otherwise it is referred to as the loose-strand.
If no push-forces are acting in one of the strands an operational endplay (OEP) exists. It is defined as the sum of all (positive) gaps between the elements. It affects the dynamic behavior of the system and depends on the assembly of the belt as well as the applied loads.
In the two arcs the torques are transmitted via frictional forces. These act between elements and sheaves as well as between elements and rings. For the default configuration the elements run in from a loose-strand, i.e. the LS in this case. Thus, the elements transmit low (or no) push-forces at the first part of the PRI– the so called *idle arc*. Push-forces rise in the *active arc* of the PRI after the turnaround point (TAP),. These push-forces are reduced to the level of the loose-strand in the SEC. However – depending on the configuration[2] – the forces can increase in the first part of the arc yielding another TAP.

For the force transmission the elements are the key part. All contact forces are transmitted via the elements. Figure 1.3 shows a sketch with the contact positions. The torque is transferred into the belt at both flanks on the left and on the right side. It is distributed on the one hand

[2] i.e. boundary conditions, contact positions, stiffness as well as friction values

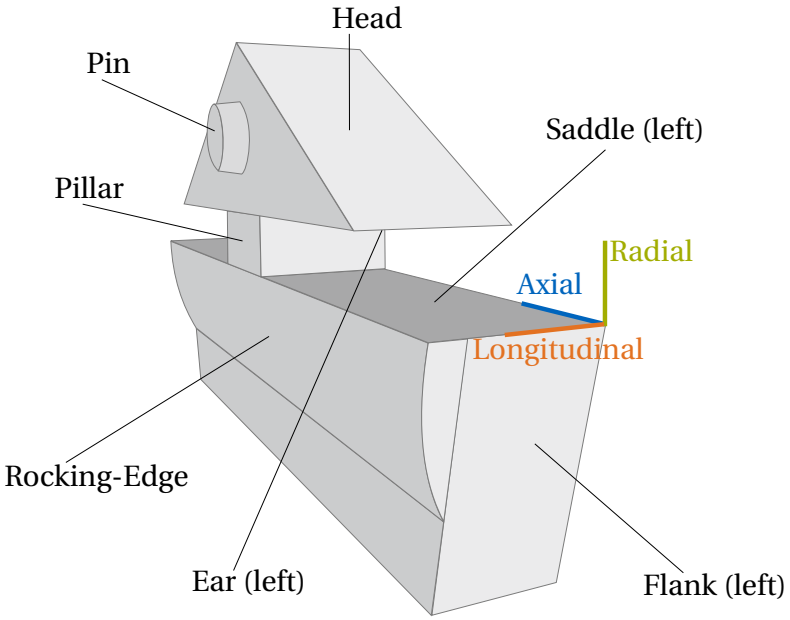

Figure 1.3: The element with local directions

via contact forces among the elements themselves either at the rocking-edge (RE), the head or the pin. On the other hand the contacts on the saddle or the ear introduce tension forces[3] in the rings.

Three local directions are defined for the element. The *longitudinal* (sometimes also *tangential*) direction points from the back to the front of the element. The *radial* direction points from the bottom of the element to the head. The third direction is defined as the *axial* direction from the left flank of the element to the right flank. It is therefore also (disregarding small rotations of the element) the axial direction of the axes in the PRI and the SEC.
With the three local directions three rotation directions are defined which follow the standard definition in automotive or aeronautics. *Pitching* is the rotation around the local axial direction, *rolling* around the longitudinal direction and the element *yaws* around the radial direction.

1.2 State of the Art

In the last decades different research groups and authors have contributed to the development and enhancements of CVTs. This development is driven by both, measurements of the system and its modeling. This section gives the state of the art with literature focusing on models of pushbelt CVTs. Models concerned with the stationary behavior and the ones focusing on the shifting dynamics are separated. It emphasizes that two different approaches exist in the literature to model these two different modes of the CVT. Finally, current research topics are presented.
The model of this thesis combines both modes into one detailed model. Non-smooth multibody dynamics is utilized for it. Thus, the well-established theory in this field is introduced. The section concludes with a detailed summary of prior work, on which this thesis is based on.

[3] which can carry up to 40% of the transmitted torque [65]

1.2.1 Pushbelt CVT

A detailed overview about the dynamic modeling of CVTs and thus a good starting point for further literature research show SRIVASTAVA ET. AL. (2009) [65]. In the following, a short chronological overview is given pointing out the most important works concerning pushbelt CVTs. Thereby stationary models and those who analyze the shifting dynamics are separated. The most recent research is given at the end.

Stationary Models

DITTRICH (1953) compares in [13] experimental results of conical belt drives to theoretical calculations based on the theory of EYTELWEIN (1808) [18]. He identifies the effect of spiral running and discusses the necessity of over-clamping that leads to a loss of efficiency [61]. He recognizes the complexity of the system and thus draws mainly qualitative conclusions.

GERBERT (1985) discusses the pushbelt mechanics in a planar steady-state model focusing on the velocity distribution of the elements and rings. The model uses Coloumb friction, omits inertia of the elements and regards an uncoupled plate deformation. Low and high torque states are distinguished and their influence on the push-forces as well as on the arc mechanics, i.e. idle and active arc, are discussed. The results show the basic effects in a pushbelt CVT that can be found in measurements – especially concerning the separation of rings and elements.

VAN ROIJ and SCHAERLAECKENS (1993) discuss the force equilibria within the pushbelt [73, 74, 75]. Three separated models are derived to compute the clamping forces. The UD configuration before transition torque is treated as well. Based on the resulting force distribution the effects on internal losses are given.

FUIJ, KUROKAWA, KANEHARA and KITAGAWA (1993 - 1995) did a remarkable effort in measurements for the CVT variator which are published in four parts [22, 23, 35, 36]. Besides global analysis of thrust- , torque- and speed-ratio, local measurements have been carried out. They yield the forces acting between the elements, rings and sheaves and give a qualitative reference. Stationary and shifting cases are measured and evaluated.

SATTLER (1999) develops in his thesis a planar CVT model with a continuous belt for stationary situations. The focus is set on the dynamic situation in the two arcs omitting the dynamics in the strands. Besides a parameter variation the work validates the model with measurements concerning global output values like thrust ratio and efficiency [51].
All in all the model is well suited for chains. However, certain effects in the pushbelt, e.g. separation of the elements or the interaction of the elements with the rings, are missing.
SUE (2003) enhances the model of SATTLER to enable faster calculations. He analyzes the effect of different sheaves on the efficiency of the system [69].

SRNIK (1999) develops the first fully dynamic model of a chain-type CVT [68]. He uses the theory of non-smooth MBS. It considers transient dynamics as well as oscillatory effects. The separated modeling of the single pins in the chain identifies the polygonal effect to be a important driver for oscillations in the system. A detailed deformation representation of the sheaves with the pins yields a good correlation with measurements.
SEDLMAYER (2003) enhances the model of SRNIK using a spatial representation. He shows, that the misalignment of the pulleys leads to higher internal forces in the chain and analyzes optimization strategies to reduce these.

SHIMIZU ET. AL. (2000) model the pushbelt CVT as a spatial finite element (FE) system, however quantitative or qualitative results are missing [60].
SAITO ET. AL. (2002-2011) choose a similar approach as in [60]. They use FEs for the single layers of the rings, rigid or flexible elements and rigid sheaves comprising a deflection motion [48, 49, 50]. Simulation times comparable to "the [...] time as [...] for durability testing" [49, p. 228] yield promising results. Yet, it stays unclear which contact forces and geometries are used and which model assumptions are made to gain the results. An analysis of the stresses within the rings shows the influence of misalignment and suggests improvement possibilities in design. Different stiffness as well as geometry changes are analyzed concerning local stresses within the parts and the efficiency of the full variator.

BULLINGER (2005) models a pushbelt CVT as a planar but fully dynamic MBS. He remarks that elements should be modeled separated [6, p. 82]. Due to a lack of appropriate algorithms, he chooses a quasi-continuous model of the pushbelt covering the single ring layers as well as the single elements. Using an Eulerian description for the kinematics he is able to model stationary cases efficiently and to validate his results with measurements from the literature.

LEBRECHT (2007) derives a simplified model to enable the coupling to drivetrain models and fast analysis of transient dynamics. He correlates the results to the models of SRNIK, SEDLMAYER and BULLINGER to measurements. Furthermore, he compares chain and pushbelt CVTs in terms of efficiency and force distribution. Finally, he analyzes the noise, vibration and harshness (NVH) properties of both types and points out the influence of Stribeck friction on the NVH behavior.

GEIER (2007) develops a planar dynamic CVT model. He separates the dynamics of the elements and the rings [25] and enables transient dynamics. Based on this SCHINDLER (2010) derives a spatial pushbelt CVT model using MBS [54, 57]. CEBULLA (2014) enhances the model of SCHINDLER in [9]. This work is based on these models. Detailed summaries are covered in Subsection 1.2.3.

Shifting analysis

SUN (1988) develops on basis of results of GERBERT a planar but transient model of the pushbelt CVT assuming one dimensional continuous elements and ring-layers [70]. Neglecting the pulley and ring deformation he is able to derive a set of implicit equations and considers ratio- as well as torque changes. He discusses his results qualitatively.

IDE (1995) analyzes the shift behavior and builds a heuristic model based on measurements [30]. CARBONE ET. AL. (2005 - 2007) develop a theoretical model for the transient dynamics of chain or pushbelt CVTs, which represents the *creep mode* as well as the *slip mode* [7, 8]. The one-dimensional model using an in-elastic band with kinematical prescribed spiral running shows good correlation with performed measurements. It is successfully used in further applications [62].

SRIVASTAVA (2005 - 2007) develops a model for the transient dynamics of a continuous one-dimensional metal V-pushbelt CVT [66, 67]. Focusing on high-speed applications the influence of inertia effects is treated neglecting belt deformation but incorporating sheave deformations kinematically.

Recent Research

Whereas the improvement of models for pushbelt CVTs has slowed down in the recent years, research treats more the overall behavior of the system. The focus is set on reducing the safety factor for control and increasing the efficiency.
VAN DER SLUIS ET. AL. (2013) gives an overview about the state of the art for pushbelt CVT development together with current research focus [63]. Based on "Key Performance Indicators", i.e. efficiency and comfort, he points out the latest improvement strategies. Higher friction coefficients between elements and sheaves as well as enhanced control to reduce safety reduce losses. The identification of noise sources helps to improve the comfort.

IDLER (2014) employs in his thesis the scuffing for CVT variators using pushbelts and chains in combination with different variator systems [31]. He enhances the models of SATTLER and SUE as well as of TENBERGE concerning shifting with experimental data for the spiral running and the bearing forces. Furthermore, he develops a formula for the traction coefficient to respect the normal force influence on the friction. Based on a model for the local surface temperature, he enables the prediction of scuffing in CVTs.

JI ET. AL. (2014) are interested in the differences of the dynamic behavior of the system for micro- and macro slip states [34]. With a simple model, which neglects deformation effects, they suggest a mechanism to identify the state the variator online by using external vibrations. The comparison to measurements yield qualitative correlation.

LEE ET. AL. (2014) suggest a logic to optimize the clamping forces and thus enhance efficiency [40]. With a simple force based model tests on a hardware in the loop and a field vehicle show improved results.

VAN DER NOLL ET. AL. (2015) investigate on the NVH behavior of the variator [44]. They correlate the element impact noise (EIN) phenomenon with eigenmodes of the pulley-sheaves and the running-in frequency of the elements in the belt. Optimization strategies suggest a randomized element order. Experiments are performed successfully.

1.2.2 Multibody Dynamics

As discussed in the previous section, different models of CVTs exist. Most of them are limited in one or more aspects. Some effects are neglected, e.g. misalignment, transient dynamics or pulley deformation. For a deep understanding of the complete system, it is necessary to model the full dynamics of a pushbelt CVT. This thesis uses the theory of MBS including nonlinear and non-smooth dynamic effects. An introduction to the theory of MBS is given in this section such that the models discussed in the following chapters can be explained. As the implementation is done in the software MBSIM the theoretical discussion is based on its idea of MBSs [21, 55].

Literature Remarks

Many authors discuss the treatment of systems as a MBS. Different textbooks are available that show the derivation of the equations of motion (EOMs) for smooth or non-smooth modeling. It is not possible to list all works. The following examples for different approaches may serve the reader as a reference. 1997 SCHIEHLEN and SHABANA summarized in two articles the state

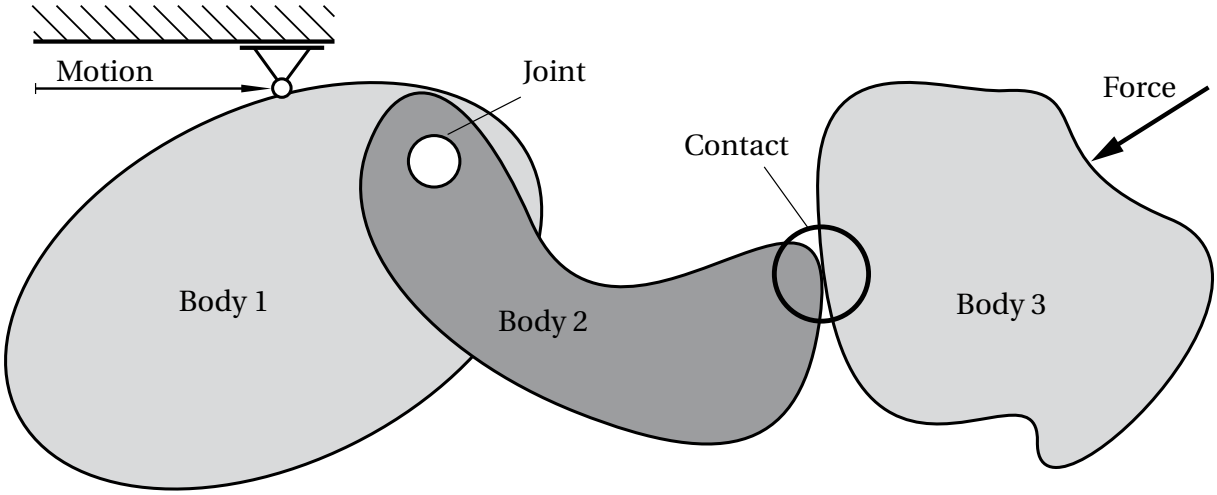

Figure 1.4: Overview of a MBS with three bodies connected with joints or contacts and excited with forces or prescribed motion.

of rigid and flexible MBSs referencing more than 200 other works [53, 59].

An overview about the whole field of smooth dynamics is given in [58]. SHABANA introduces the basic concepts of dynamical systems to set up a MBS. The EOMs for rigid bodies with bilateral constrained conditions are derived. A special focus is set on deformable bodies using the floating frame of reference (FFR)-formulation or the absolute nodal coordinate formulation (ANCF)-method to represent nonlinear deformation fields of deformable bodies. GLOCKER discusses in his thesis rigid body systems with friction and impacts theoretically [27]. He introduces the fundamental formulations for unilateral and bilateral non-smooth contacts with tangential laws, e.g. friction, and derives the EOMs, which are then measure differential equations. He treats coupled and partly elastic impacts. An even broader basis for the theory and numerical treatment of non-smooth system can be found in [1]. ACARY and BROGLIATO treat non-smooth phenomena also in electrical circuits.
FÖRG develops a numerical framework for general, i.e. spatial and non-smooth MBSs [20]. He derives the EOMs with the constrained conditions and shows numerically efficient solution algorithms using proximal functions which yield a nonlinear equation system. ZANDER treats flexible MBSs with non-smooth effects on the basis of FÖRG [78]. He points out the necessity of locality for the discretization of a flexible body when treating impacts.

Theory

Dynamics A MBS consists of n rigid or deformable bodies as sketched in Figure 1.4. The kinematics of every body i is defined by a mathematical model with a set of degrees of freedom (DOFs) which are the generalized positions q^i and the generalized velocities u^i. Both can be summarized in vectors for the whole system as

$$q^T = \begin{bmatrix} q^1 & \dots & q^n \end{bmatrix} \qquad u^T = \begin{bmatrix} u^1 & \dots & u^n \end{bmatrix} \qquad z^T = \begin{bmatrix} q^T & u^T \end{bmatrix} \tag{1.4}$$

where z denotes the state vector of the MBS.
Forces λ or impulses Λ couple the motion and define the change of acceleration or velocity of the bodies respectively. Generally two different kinds of coupling laws can be chosen for joints, contacts, external forces and prescribed movements.

Single-valued laws define the reaction force explicitly[4] from the state vector and the time t.

$$\lambda = \lambda(z, t) \tag{1.5}$$

No impulses are covered.
Set-valued laws constrain the motion by a condition.[5] This induces, that the system may change in a non-smooth way, i.e. there are jumps in the velocity. Impacts, i.e. impulses, have to be taken into account as well with

$$(\lambda, \Lambda, z, t) \in \mathcal{N} \tag{1.6}$$

where $\mathcal{N}$ summarizes all set-valued conditions of the system which have to be fulfilled by the state, the forces and impacts at every time.
The EOMs for the whole non-smooth system are then a measure differential equation with

$$\dot{q} = Tu \tag{1.7a}$$
$$M\dot{u} = h + W\lambda \tag{1.7b}$$
$$M_k(u_k^+ - u_k^-) = W_k\Lambda_k \tag{1.7c}$$
$$(\lambda, \Lambda_k, z, t) \in \mathcal{N} \tag{1.7d}$$

where $T = T(q)$ is the transformation between generalized velocities and positions, $M = M(q)$ the mass matrix of the system and $h(z, t)$ the smooth right-hand side vector. The wrench matrix $W = W(q)$ defines the direction on how forces or impacts, which result from a set-valued reaction, project into the directions of the generalized velocities.
Equation (1.7b) shows the smooth velocity change for the system whereas (1.7c) contains the non-smooth velocity changes for times t_k, the times of an impact within the system.

Integration For a numerical integration of (1.7) it is necessary to discretize the EOMs in time. The half explicit time-stepping scheme on velocity level of [20, section 4.4.1] has proven most sufficient for the present model. It is summarized shortly in the following.
Starting from time t_i with the state z^i one approximates with the time step size Δt^i the generalized positions of the next time step with

$$q^{i+1} \approx q^i + T(q^i)u^i\Delta t^i \qquad \Rightarrow \tilde{z}^i = \begin{bmatrix} q^{i+1} \\ u^i \end{bmatrix} \tag{1.8}$$

yielding an intermediate state $\tilde{z}^i$ which is used for the evaluation of the following equations. The constraints for the continuous motion (1.7b) and non-continuous motion (1.7c) can be treated simultaneously as continuous forces can be interpreted as an impact for a finite time step. The velocities of the next time step are approximated with $\tilde{z}^i$.

$$u^{i+1} \approx u^i + M^{-1}(q^{i+1})\left(h(\tilde{z}^i, t^{i+1})\Delta t^i + W(q^{i+1})\Lambda^{i+1}\right) \tag{1.9}$$

The relative velocities γ that are associated with the impulses Λ depend on the generalized velocities and can be written as

$$\gamma^{i+1} = (W^{i+1})^T u^{i+1} + w^{i+1} \tag{1.10}$$

[4] For practical examples [20, p. 18]
[5] e.g. in normal contact direction a non-negative distance between the contact partners is enforced

where w^{i+1} is a time dependent vector.[6] Inserting (1.9) in (1.10) leads to a linear equation between the impulses Λ and the relative velocities γ that are in general complementary to each other. The mass-action-matrix[7] is defined to be

$$G = W^T M^{-1} W \tag{1.11}$$

which plays a central role for the non-smooth solution.[8] For this time-stepping algorithm G is symmetric.
Projection functions reformulate the complementarity problem of equations (1.9) and (1.10) to a nonlinear system.

$$F(\Lambda^{i+1}, \gamma^{i+1}) = 0 \tag{1.12}$$

1.2.3 Prior Works

Three works, based subsequently on each other, are the direct background for this thesis. All are summarized here in detail emphasizing the most important parts. GEIER modeled a planar pushbelt CVT using independent kinematics of the elements. SCHINDLER enhanced the model using spatial dynamics for all parts of the system. CEBULLA finally focused on implementing new force laws and optimizing the kinematical description.

Dynamics of Push Belt CVTs

The works introduced in Subsection 1.2.1 model specific effects of the CVT system. Depending on the application some major effects are omitted that are important for a detailed analysis of a pushbelt CVT. GEIER is the first to incorporate all main phenomena within a planar system in *Dynamics of Push Belt CVTs* [25].

The elements can move independently from the rings and are only coupled by physically based contact laws. The contact kinematics defined on one element can be evaluated fast as they are mostly based on analytical kinematics. For the contact between element and ring a minimal distance has to be found with a nonlinear function. The rings are modeled with the redundant coordinate method (RCM) using co-rotated-FEs. Each FE has an internal set of DOFs, which describes a nonlinear rigid body movement in a floating reference frame and in addition local deformations. Besides deflection, also elongation of the rings is possible with this approach. The FEs are coupled due to a global coordinate set. For the planar case the transformation function is explicit to get the local coordinate set out of the global one. The reader is advised to [78] for further details. Besides the detailed modeling of the rings, also a quasi-statical deformation of the pulley set is included. Spiral running is therefore represented well. All submodels are formulated in a time independent manner such that transient behavior could be studied.

In the model the number of elements could be chosen freely. Based on 160 elements that are used in the simulation a number of about 650 DOFs and about 1440 contact points result.[9] The results are compared qualitatively to literature values. Local forces and kinematics could

[6] Normal impacts with an elastic part are not of interest here but discussed in [27, 20].
[7] also called “Delassus-Matrix”
[8] The time step is not given as it is a general definition for time-stepping algorithms
[9] Up to 1500 DOFs and 3500 contacts are possible in case of 400 simulated elements [25, p.81].

be validated as well as global trends for stationary conditions. Further simulation results show qualitatively good results. The model therefore has proven successful for the simulation of a pushbelt CVT disregarding spatial effects.

Spatial Dynamics of Pushbelt CVTs

SCHINDLER covered also spatial effects in *Spatial Dynamics of Pushbelt CVTs* [55]. The elements are modeled dynamically as rigid bodies with six DOFs. Elastic deformations are covered in the contact laws. The element-element interaction is modeled as a nonlinear function. The element-sheave interaction uses a linear penalty function. Tilting deformation of the sheaves is constrained by linear force laws to cover the coupled deformation of the flat pulley-sheaves and the shafts. Flexible sheaves based on a Reissner-Mindlin plate theory using FE are developed but no results are given. Two rings are simulated using an extended RCM including out of plane movements. In the spatial case of the RCM model the internal FE and the global coordinate sets are coupled in a nonlinear system. It is solved during each time step in the simulation [54, p. 23]. The elements are bound bilaterally to the rings in normal direction with a set-valued contact law. Compared to the planar case the contact kinematics gets more complex. Spatial conditions have to be covered leading to more search directions along the surfaces. Due to the increased number of DOFs of about 1200 combined with around 2100 contact points[10], the simulation costs increased.[11] To reduce computational time, a stationary belt model based on [51] is derived. The transition time at the beginning of each simulation could be shortened compared to a full run up. Parallelization techniques are tested for single simulations. A parallel computation of different load cases has been found to be more efficient.

Results are compared to values of literature and to measurements conducted by BTT. All in all correct trends are presented for global as well as for local values. However, improvements are suggested concerning the ring model, the element-pulley interaction and possible model order reduction techniques. The work offers a basis for a deeper analysis of spatial effects within a pushbelt CVT.

Spatial Dynamics of Pushbelt CVTs: Model Enhancements to a Non-smooth Flexible Multibody System

CEBULLA focused on central processing unit (CPU) time reduction to further improve the models described in Subsection 1.2.3. Due to the complex contact kinematics and the high number of DOFs, the key part of the model concerning CPU time are the rings. A spatial rod model, which is presented in [38], follows the theory of COSSERAT and uses finite differences for the discretization. It shows promising results and therefore is adapted for the usage within the CVT model. The planar version is described in *Spatial Dynamics of Pushbelt CVTs: Model Enhancements to a Non-smooth Flexible Multibody System* [9]. A planar version of the pushbelt CVT is therefore set up to test and validate additions to the model.
A coupled contact law for the quasi-static representation of the pulley-sheave deformation in the spatial case has been derived and added to the model. For the solution of the resulting linear complementarity problem (LCP) a LEMKE algorithm or a reformulated system using proximal functions is suggested. While the same coupling technique of the sheaves is used as

[10] based on 160 simulated elements

[11] Up to 2650 DOFs and 5200 contacts are possible in case of 400 simulated elements.

in [25] different coupling options for the elements are presented. Yet, these have not been validated.
The element-ring contact has been enhanced in two steps. At first the bilateral contact in normal direction at the element saddle has been replaced by two unilateral contacts at saddle and ear. This yields a remarkable CPU time reduction [9, p.129]. In a second step, the penalty function for the axial movement of the rings on the saddle has been changed from a stiff bilateral function to a heuristic model for the so called ring-tracking. The effect of this model has not been tested. To cover production uncertainties, tapered elements have been added to the model. An adapted initialization process is given to reduce the transition phase to a stationary point in the simulation. Different settings of the boundary conditions are enabled and the necessary equations are derived theoretically. Simulation results are compared to values from literature and measurements from BTT.

Altogether CEBULLA extended the model of SCHINDLER in many points and shows improvements of different submodels. Yet, a detailed analysis of the model is missing. The present work discusses the described models with different submodels in detail with respect to (wrt.) their numerical and physical behavior. New submodels have also been added where the analysis showed necessity for improvement.

Summary of the model

The three works above lead consecutively to a complex and detailed model of a metal V-pushbelt CVT. The most important properties and assumptions are summarized here in a compact manner.

- Spatial effects, e.g. misalignment, are modeled besides a planar version.
- Transient dynamics, e.g. torque or speed run up situations as well as shifting movement, are covered.
- The elements are treated as single, i.e. non-continuous, rigid bodies covering nonlinear deformation due to contact-laws quasi-statically.
- The sheaves are treated as single rigid bodies with a coupled deformation, leading to e.g. spiral running.
- The rings are modeled as one (planar model) or two (spatial model) flexible bodies regarding elongation, in- and out-of-plane bending along the belt.
- Contacts, i.e. normal forces and friction forces, are modeled either non-smooth or regularized possibly using nonlinear functions, e.g. element deformation or Stribeck friction.
- No overall kinematical assumptions are made concerning contact situations in the arcs, e.g. separation of active or idle ar or separation of the elements in the loose-strand. Yet, the effects result out of dynamic simulation.

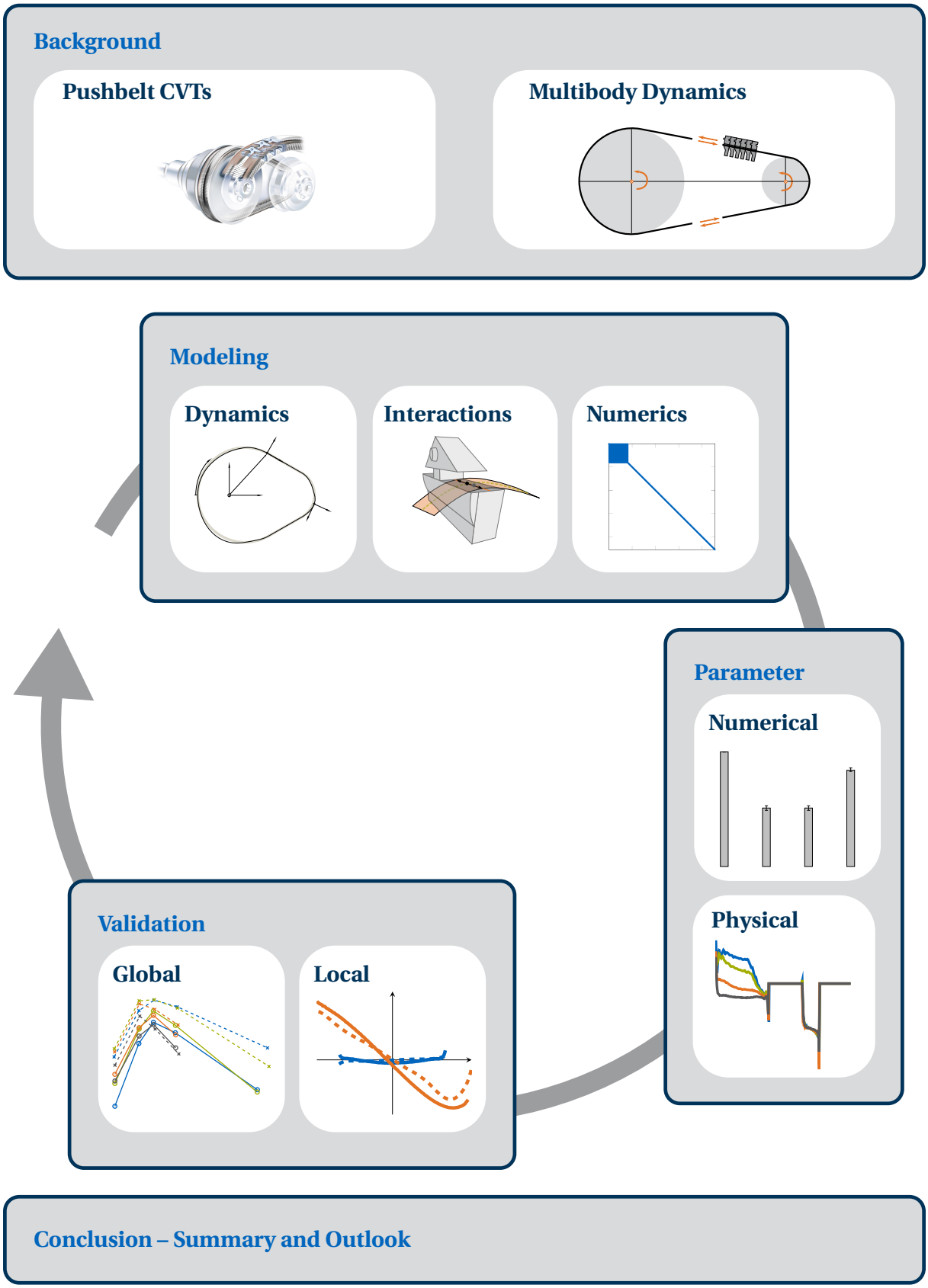

Figure 1.5: Overview of the thesis

1.3 Structure of the Work

An overview about this work is visualized in Figure 1.5. After motivating the thesis the system pushbelt CVT is described in Section 1.1 to introduce the most important concepts to the reader. The current research state is given in Section 1.2. A literature overview for pushbelt CVTs shows the state of modeling at the time of writing. Models exist to investigate on specific settings of the CVT. Yet, a detailed model covering all major effects is still missing. To enable such a model the method of MBS is chosen. The well-established theory is summarized. A detailed model of this system has been set up and enhanced in the past which is described at last. It forms the starting point for this work.

The validation of models is an iterative process. Comparing to measurements combined with qualitative discussion of the physical interpretable behavior of a first simple model yield improvement ideas for the next one. Eventually a model should consider all relevant effects being as simple as possible to be interpretable after all [71].
The iterative process is in fact a loop in which every part affects the others leading to new ideas for either modeling, simulating or validating. The sequence for this thesis starts with the modeling in Chapter 2, then discusses the sensitivity on numerical and physical parameters in Chapters 3 and 4 respectively to finally validate the state of the model in Chapter 5. It is emphasized that the results of this work can only be seen in context of all these chapters.

Following this introduction the dynamical models are discussed in Chapter 2. Three aspects are discussed separately, i.e. the dynamics of the single parts, their interaction and the resulting numerical challenges.
Efficient models demand rigid dynamics of the elements and sheaves respecting their deformation in interactions. The rings however deform nonlinear dynamically. A specific model covering the overall motion with a minimal number of DOFs is derived, which enables fast integration. Selective adaption of the dynamical representation, e.g. spatial motion or spiral running, allows for efficient integration within specific applications.
Interaction models are crucial for the correct representation of the force equilibrium. The adaption of the element's thickness leads to a varied stiffness which is respected in the contacts. The contact kinematics for curved surfaces of sheaves and elements are derived to enable geometrical adaptions. The coupled deformation of the two pulley-sheaves due to the contact to all elements in one arc is suggested furthermore. The nonlinear deformation of the elements in longitudinal direction is respected with a special force law. An updating process using a special measuring device, i.e. the Push-Force-Tester, is performed to gain precise parameters. The spatial interaction between element-saddle and ring is analyzed in means of ring-tracking. Former models are discussed and a new one is suggested, which respects the normal force influence.
The computation of the models on a CPU leads to numerical issues, which are treated at last. A kinetics based initialization scheme shortens the transition phase and thus the simulation time. The application of modern solution schemes for the complementarity problem between elements and sheaves reduces the simulation time further in every time step. Finally, the usage of sparse matrix algebra in combination with the specific properties of the integration scheme yields faster integration when non-smooth force laws are used in the model.
The post-processing steps conclude the chapter which serve as basis for the further analysis of different aspects of the system.

Models are tested on their qualitative output as well as on their sensitivity on parameters. Numerical aspects are treated in Chapter 3. To save simulation time less elements are used in

simulation than in reality. The influence of this is studied at first to find a minimal number of elements and to show the difference to a reference simulation, i.e. the overall quality. Then the influence of different contact laws is studied using either single- or set-valued functions which affects both the simulation time as well as the physical output behavior. Finally different dynamical models for the rings are compared in means of CPU costs and physical output. A further analysis tests the applicability of the approach for spatial simulation.

Besides numerical based parameters, also physical based parameters are not known exactly. Their impact on the system's behavior is discussed in Chapter 4. This forms the basis for two improvements. On the one hand the parameters can be updated for precise outputs of the model. On the other hand it offers optimization strategies for future belt designs.
The number of elements that are used within the belt assembly is not known precisely. The parameter is set by experience. However, small changes lead to different system outputs which are treated in Section 4.1.
In Section 4.2 the most important parameters for the contact between element-flank and pulley-sheave are discussed. The contact position along the flank is unknown as well as the stiffness in axial direction. Both influence the system's behavior strongly.
The same holds for the contact in-between the elements. The geometry for the head depends on the element specification. Thus the contact point is uncertain in terms of radial as well as longitudinal position. Both aspects are discussed in Section 4.3.
Finally, the friction parameters for the contacts element-pulley and element-ring are analyzed in Section 4.4.

The model is validated in Chapter 5 based on the discussion of the previous chapters. Force distributions along the belt and kinematics in the arcs are compared qualitatively for a broad spectrum. Furthermore, quantitative measurements are compared for the most important local forces.
Global measures, i.e. descriptive values for certain stationary cases, are compared for varying boundary conditions. The trends for the thrust ratio and efficiency yield quantitative matches for a variator with well identified parameters. Other variator setups show the necessity for an updating process. Furthermore, the influence on external loads and the robustness against e.g. wear are validated with measurements.
At last, instationary effects are treated. On the one hand the gear-rattle noise can be related virtually to the frictional curves. On the other hand shifting situations are compared to values from the literature qualitatively.

Finally, the work is summarized in Chapter 6. Based on the conclusion an outlook on further research possibilities is given.

2 Modeling

Many iteration steps have been done leading to the current detailed model during the validation process of the model. The single refinement steps for different aspects of the model are given in the following chapter. Thereby, three types of modeling aspects are separated.
At first the dynamics is addressed in Section 2.1. Preliminary considerations discuss the three parts within the CVT, i.e. elements, sheaves and rings.
The rings are a crucial concerning computational time [54, p. 68]. Many DOFs are necessary and complex contact kinematics have to be used solving nonlinear equations each time step. A further dynamical submodel for the rings is introduced. The kinematics is specifically derived for the CVT application. The DOFs could be reduced and a faster contact search is enabled. The global and local kinematics are separated which makes it easy to interpret the results. These different levels of detail in the model enable also new strategies for specific applications.

The contacts between the single bodies are discussed in Section 2.2. Existing models are presented shortly to motivate enhancements. New models concerning contact kinematics and contact laws are given for element-element-, element-ring- and element-sheave-contact. Parametric options are analyzed and discussed qualitatively wrt. the results in the CVT model.

Finally, the reduction of the computational costs is treated in Section 2.3. The solution process of the coupled contact law between elements and sheaves is optimized. Different models lead to either one or two contact points. The impact on the solver is discussed. Conclusions suggest which model should be used.
The initialization process is enhanced as well. Kinetic models are used to enhance the estimate of the stationary condition at the beginning of the simulation. Thereby, the transition phase, i.e. oscillations due to initialization errors, is shortened.
The solution of the set-valued conditions is treated at last. Improved algorithms reduce CPU costs when the presented time-stepping integration scheme (Subsection 1.2.2) is applied.

For discussion and validation, the post-processing steps are finally given in Section 2.4. Averaging techniques are used to separate trends along the arc from local effects. Based on these, global values are gained which are used as general comparison numbers.

2.1 Dynamics

2.1.1 Preliminary Considerations

The modeling of the dynamics of the single bodies in a MBS is the first step to gain a complete model. Each body may be represented with six rigid DOFs. Possible deformations are

accounted for with quasi-statical non-impulsive contact force laws. The numerical treatment is typically more robust as for flexible-body dynamics. Faster simulation times result as less DOFs are used.
Yet, the dynamical response of sub-parts of the system may be an important effect that has to be modeled. Flexible models are utilized. The number of DOFs increases and thus the simulation time.

Elements

The elements are the key part within the model. The longitudinal as well as the axial deformation do influence the dynamics significantly (Chapter 4). These deformations can be represented very well with single-valued contact laws [25]. A deformable representation also would increase the simulation time substantially affecting about 200 to 400 bodies. Therefore, rigid body dynamics is chosen incorporating the deformations within the contact laws to gain short integration times.

Sheaves

The pulley-sheave deformation is known to be the main driver for the spiral running. Their deformation is well approximated by quasi-statical contact models [9]. However, the EIN is assumed to be coupled to the eigenmodes of the pulley-sheaves. This gives reasons to model also these bodies deformable [44].
The sheave model described in [54] has found to be not efficient. Therefore, also an FFR based model for the sheaves has been derived and tested in [77]. A full finite element method (FEM) model of the pulley has been used to gain modal modes. NURBS[1] interpolation is used to enable contact kinematics. Both approaches show the typical problems of deformable bodies. In particular the simulation time increases. Due to modal reduction the locality of the contact cannot be provided exactly influencing the dynamics.
Altogether, elastodynamic sheaves are not used to ensure efficient and robust integration. The dynamic feedback to the overall behavior of the system could not be tested. A one-way coupling, i.e. using the forces from the simulation to excite e.g. a full dynamic FE model of the pulleys, is possible to study particular effects e.g. the EIN.

Rings

For the rings a deformable model is necessary. Spiral running within the arcs and dynamic oscillations within the strands should be respected. A change of the ratio has to be covered to enable shifting dynamics. As the ring models derived in [54] and [9] lead to numerically stiff or ineffective models, a new ring model is specifically derived for CVTs in Subsection 2.1.2. Using a mixed parameter description for global and local deformations and avoiding internal constraints leads to a minimized number of DOFs and a robust model.

[1] see [47]

2.1.2 ALE Ring Model

Ring models are crucial within the complete CVT. Spatial and nonlinear deformation has to be represented efficiently to enable fast integration. Due to many contacts between elements and rings locality of the deformation should be preserved.
Different techniques exist in the literature to represent nonlinear behavior of one dimensional bodies. Four different models have been tested within the CVT. This section summarizes the ideas of the RCM, the large rotation vector method (LRVM) or the ANCF. For the LRVM and the ANCF planar models are presented as difficulties are apparent in this case already. Additionally, the main results are given that motivate the development of a new model. Eventually, the EOMs of a model based on the arbitrary Lagrangian-Eulerian (ALE) technique are derived, which takes into account the disadvantages of the other models. All models are implemented in multibody simulator (MBSim) [21].

Literature Models

RCM Model In [25] a planar model for the beam dynamics uses a co-rotational approach. A local set of DOFs q_l describes the deformation of a FE of a beam with linear material properties. The assembly is done via a global set of DOFs q_g. An explicit relation between the local and the global DOFs exists. Thus, nonlinear kinematics can be represented globally. Qualitatively a good correlation between measurements and simulation could be achieved.

For the model in [54] a spatial enhancement is derived using the same ideas. Yet, the relation between q_l and q_g cannot be resolved explicitly. A root-finding algorithm has to be applied for each FE at every time step. This leads to an increased simulation time.
Furthermore, the time step is limited as otherwise the root finding algorithm might not succeed. Using more FEs leads to smaller time step sizes for a robust simulation. A stiffness-like phenomenon is observed. It is not classical stiffness as an internal transformation is affected. Stabilization techniques could not be applied successfully for the root finding algorithm and therefore other modeling ideas have been tested.
In [54] 12 FEs are used as a compromise between robustness and calculation time. However, practical tests with the planar model of [25] show that this might be too few FEs to represent the curvature change between arcs and strands. Numerical induced oscillations result in the strands. Based on these observations another ring model is needed for spatial integration.

LRVM Model LANG ET. AL. showed in [38] a promising formulation based on LRVM. Cosserat theory is used to represent nonlinear deformations of rods in the field of MBS. The LRVM separates a position field and a rotation field with two sets of DOFs. Finite differences are used to discretize the EOM and a staggered grid between positional nodes and rotational nodes promises enhanced performance.
These are used to express the different terms for the energy formulation that can be used with the Lagrange II formalism to derive the discretized EOM. In [9] the EOMs for a planar model are given. A contour description is introduced to represent non-smooth contact situations. A difficulty of the LRVM becomes apparent. Either the positional field or the rotational field could be used to define the local kinematics for the points, i.e. normal and tangential directions of the contact frame, that are used to project external forces into the generalized directions.

The model does not comprise two full coordinate sets and the difficulty of the RCM beam is

not apparent. However, the material properties, i.e. steel, in combination with the unfavorable geometry, i.e. thin layers of the rings, lead in practice to a very stiff behavior. A first approach with nonlinear reduction techniques to filter high frequency ranges was not successful. It is a field of ongoing research [10]. Different choices for the contour description could not improve the behavior.

ANCF Model The ANCF technique uses the nodal deformation and the slopes, i.e. their spatial derivatives, at these positions as DOFs. The DOFs are interpolated in a global frame with global ansatz functions. Thereby, necessary rotations for e.g. beam elements can be represented in an isoparametric way. Rigid body modes are incorporated exactly. For the planar model the mass matrix is constant which is a major benefit. The inverse or a decomposition must not be calculated every time step which is a main driver for simulation time. The implementation for the model of this work follows [58, chap. 7].

Neither two coordinate sets nor a separation of positional and rotational fields are used which lead to difficulties in the discussed models using RCM or LRVM. The simulation time is reduced due to the constant mass matrix. Using this model within the full CVT model yields overall good yet oscillatory results. Besides, the mass matrix is – depending on the formulation – not constant for the spatial case.

Basic Ideas of the ALE Model

As one can see from the previous discussion general beam formulations have difficulties when applied in the present CVT model. In the following a specific model for belt drives is derived which addresses the discussed problems.
A pushbelt CVT consists of two major kinematical degrees. On the one hand the ratio defines – together with the belt length and the pulley distance – the two arc radii and the strands. On the other hand the rotation speed defines the belt speed and thus the travelling along the curve. Yet, the kinematics are not fully described with these DOFs. Deformations within the arcs, e.g. spiral running, or between the pulleys, e.g. misalignment, are small deviations from this reference description.

To represent the belt speed as a DOF, an Eulerian description is used. With it the tangential movement of a mass particle can be projected to a fixed position in space. This technique is called ALE. It is a coordinate transformation. For a closed one dimensional continuum the transformation is performed generally in Appendix A. Also the equations for the Lagrange II formalism are derived.
The ALE formulation is also used by PECHSTEIN and GERSTMAYR (2013) in combination with ANCF elements for a planar model [45]. Similar ideas have been used in [24] and [6]. However the reference kinematics were fixed and only planar DOFs are used. In the following, a spatial model using a planar reference curve is described which is referred to as the ALE model within the thesis.

The following description is general. It is not restricted to CVT belt applications but could be used for all one dimensional systems with a nonlinear reference kinematics and only local deformations.

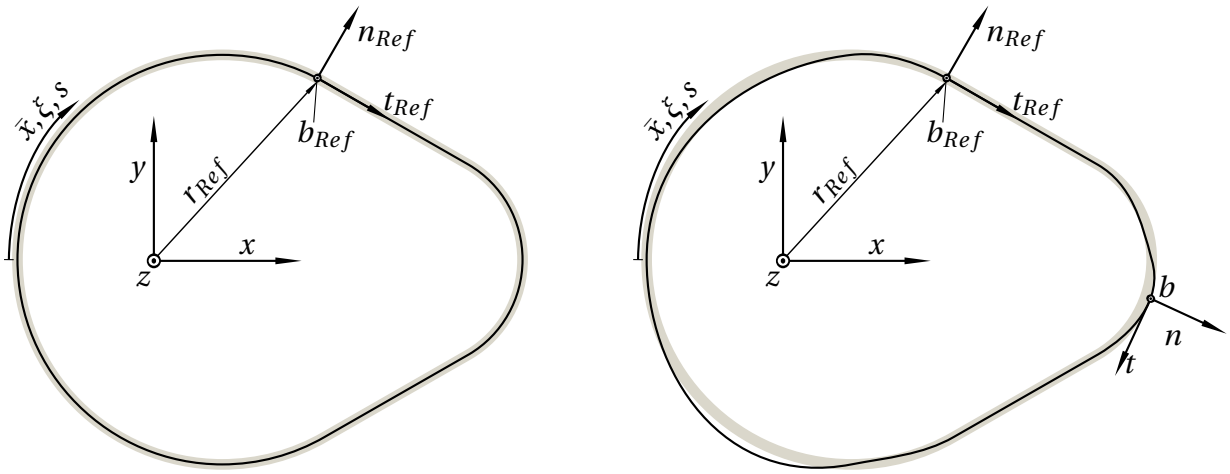

(a) Reference curve without deformations (b) Reference curve with deformations

Figure 2.1: CVT kinematics described by a reference curve

Kinematics

Consider a planar belt drive with a fixed belt length L (Figure 2.1) and a constant cross-section A. A reference curve $r_{Ref}(\Theta, \xi)$ is described along $\xi \in [0, L[$ in a fixed frame with axes x, y and z. The current reference may be described with the scalar Θ. For the CVT, it is a measure for the ratio between the two arcs. For each reference position a frame holding the tangential t_{Ref}, normal n_{Ref} and binormal b_{Ref} is attached.
A tangential drift s and the corresponding time derivative $\dot{s}$ define the position of a particle along the curve $\bar{x}$ with

$$\bar{x}(\xi, t) = \xi + \int_0^t \dot{s}(\tau) d\tau = \xi + s(t) \tag{2.1}$$

where ξ describes the original position of the particle. Therefore $\bar{x}$ depends on time.

$$\frac{\mathrm{d}\bar{x}}{\mathrm{d}t} = \dot{s}$$

The variable Θ and s describe only the reference motion (Figure 2.1a). Additional coordinates are introduced which enable a small displacement r_f around the reference position r_{Ref} (Figure 2.1b). The vector q_f^i holds the coordinates of node i which describe this deviation in the three possible spatial directions. These DOFs are interpolated by local ansatz functions $\mathbb{S}^i(\xi)$.

Position The position of a particle is given by

$$r = r_{Ref} + r_f = r_{Ref} + \mathbb{A} \sum_i \mathbb{S}^i q_f^i = r_{Ref} + \mathbb{A}\mathbb{S} q_f = r_{Ref} + \mathbb{B} q_f \tag{2.2}$$

where $\mathbb{A}(\xi, \Theta)$ is introduced as a general transformation matrix for the directions of the local DOFs. Three general different possibilities exist to choose $\mathbb{A}$:

1. The most simple option would be to choose a constant $\mathbb{A}$, e.g. as the unity matrix. It does then neither depend on ξ nor Θ.

2. A second option would be to choose $\mathbb{A}$ only depending on Θ, e.g. as the direction matrix of the node where the local deformations are measured via q_f. This would mean that the local DOFs are the node deformations in local tangential, normal and binormal direction.

3. A third option is to choose $\mathbb{A}$ to depend on Θ and ξ, e.g. $\mathbb{A} = \left[t_{Ref}, n_{Ref}, b_{Ref}\right]$ as the orientation matrix that changes over the arc with ξ. This would change the interpretation of the local DOFs always in the local tangential, normal and binormal direction respectively.

In this work the equations are derived for the most general third case to serve as basis for general applications.

Velocity To get the absolute velocity the material derivative[2] has to be applied.

$$\begin{aligned} v &= \frac{\mathrm{d}r}{\mathrm{d}t} = \frac{\mathrm{d}r_{Ref}}{\mathrm{d}t} + \frac{\mathrm{d}\mathbb{A}}{\mathrm{d}t}\mathbb{S}q_f + \mathbb{A}\frac{\mathrm{d}\mathbb{S}}{\mathrm{d}t}q_f + \mathbb{A}\mathbb{S}\dot{q}_f \\ &= \frac{\mathrm{d}r_{Ref}}{\mathrm{d}\xi}\dot{s} + \frac{\mathrm{d}r_{Ref}}{\mathrm{d}\Theta}\dot{\Theta} + \frac{\mathrm{d}\mathbb{A}}{\mathrm{d}\xi}\dot{s}\mathbb{S}q_f + \frac{\mathrm{d}\mathbb{A}}{\mathrm{d}\Theta}\dot{\Theta}\mathbb{S}q_f + \mathbb{A}\frac{\mathrm{d}\mathbb{S}}{\mathrm{d}\xi}\dot{s}q_f + \mathbb{A}\mathbb{S}\dot{q}_f \end{aligned}$$

Using the vector of generalized coordinates and generalized velocities

$$q^T = \begin{bmatrix} s & \Theta & q_f \end{bmatrix}, \qquad \dot{q}^T = \begin{bmatrix} \dot{s} & \dot{\Theta} & \dot{q}_f \end{bmatrix} \tag{2.3}$$

the velocity can be written as

$$v = \begin{bmatrix} r'_{Ref} + \mathbb{B}'q_f & \frac{\mathrm{d}r_{Ref}}{\mathrm{d}\Theta} + \frac{\mathrm{d}\mathbb{A}}{\mathrm{d}\Theta}\mathbb{S}q_f & \mathbb{A}\mathbb{S} \end{bmatrix} \dot{q} = \mathbb{P}\dot{q} \tag{2.4}$$

where

$$\mathbb{P}(q) = \begin{bmatrix} r' & \frac{\mathrm{d}r}{\mathrm{d}\Theta} & \mathbb{B} \end{bmatrix} \tag{2.5}$$

is the interpolation matrix between the generalized velocities $\dot{q}$ and the velocity of the mass particles depending only on the generalized positions q. In the following the most important steps are listed where additional equations are given in Appendix B.

Kinetic Energy

The equations for the kinetic energy $\mathcal{T}$ are derived in Appendix A. In the following, the single terms are specified. The gradient of the kinetic energy wrt. generalized coordinates is given by

$$\frac{\partial \mathcal{T}}{\partial q_k} = \rho A \int_0^L v^T \frac{\partial v}{\partial q_k} d\xi = \rho A \dot{q}^T \mathbb{I}_{PTdPdqi}\dot{q} \tag{2.6}$$

where the integral

$$\mathbb{I}_{PTdPdqi} = \int_0^L \mathbb{P}^T \frac{\partial \mathbb{P}}{\partial q_k} d\xi$$

[2]The change in position of a mass-particle has to be derived which is described by $r(\bar{x})$. The equation is written in Eulerian view and thus the material derivative has to be used.

has to be evaluated in each time step.
The time derivative of the gradient of the kinetic energy wrt. to generalized velocities becomes

$$\frac{\mathrm{d}}{\mathrm{d}t}\frac{\partial \mathscr{T}}{\partial \dot{q}_k} = \frac{\rho A}{2}\int_0^L \frac{\partial}{\partial t}\frac{\partial}{\partial \dot{q}}\left(v^T v\right) d\xi = \frac{\rho A}{2}\int_0^L 2\frac{\partial}{\partial t}\left(v^T \frac{\partial v}{\partial \dot{q}}\right) d\xi = \frac{\rho A}{2}\int_0^L 2\frac{\partial}{\partial t}\left(\dot{q}^T \mathbb{P}^T \mathbb{P}\right) d\xi \tag{2.7}$$

$$= 2\rho A \dot{q}^T \mathbb{I}_{PTdPdt} + \ddot{q}^T \rho A \mathbb{I}_{PTP} \tag{2.8}$$

where the first integral is defined as

$$\mathbb{I}_{PTdPdt} = \int_0^L \mathbb{P}^T \frac{\partial \mathbb{P}}{\partial t} d\xi \tag{2.9}$$

and the second term yields the symmetric mass-matrix $\mathbb{M}$.

$$\mathbb{M} = \rho A \mathbb{I}_{PTP} = \rho A \int_0^L \mathbb{P}^T \mathbb{P} d\xi \tag{2.10}$$

Elastic Energy

The elastic energy $\mathscr{V}$ is defined following [33] with

$$\mathscr{V} = \frac{1}{2}\int_0^L \gamma^T \mathbb{C}_\gamma \gamma d\xi + \frac{1}{2}\int_0^L \kappa^T \mathbb{C}_\kappa \kappa d\xi = \mathscr{V}_\gamma + \mathscr{V}_\kappa \tag{2.11}$$

where γ and κ are the deformation quantities and the matrices $\mathbb{C}_\gamma$ and $\mathbb{C}_\kappa$ hold the constitutive laws. The Eulerian description is used directly as other terms vanish (Appendix A). The partial derivatives are given by

$$\frac{\partial \mathscr{V}_\gamma}{\partial q_k} = \int_0^L \gamma^T \mathbb{C}_\gamma \frac{\partial \gamma}{\partial q_k} d\xi, \qquad \frac{\partial \mathscr{V}_\kappa}{\partial q_k} = \int_0^L \kappa^T \mathbb{C}_\kappa \frac{\partial \kappa}{\partial q_k} d\xi \tag{2.12}$$

with the strain energy $\mathscr{V}_\gamma$ and the curvature energy $\mathscr{V}_\kappa$. The constitutive correlations for an isotropic material are used with

$$C_\gamma = \begin{bmatrix} EA & 0 & 0 \\ 0 & GA_n & 0 \\ 0 & 0 & GA_b \end{bmatrix} \quad \text{and} \quad C_\kappa = \begin{bmatrix} GI_t & 0 & 0 \\ 0 & EI_n & 0 \\ 0 & 0 & EI_b \end{bmatrix} \tag{2.13}$$

where E is the Youngs modulus, G the shear modulus and A_n and A_b the shear areas in normal and binormal direction respectively. The quantities I_n and I_b are the area moments of inertia for bending around the normal and binormal direction respectively and I_t is the torsional area moment of inertia. Off-diagonal coupling terms are neglected.

Strain energy For the strain energy the material strain measure is used with

$$\gamma = A_{IK}^T r' - \begin{pmatrix} 1 & 0 & 0 \end{pmatrix}^T \tag{2.14}$$

where the rotation matrix

$$A_{IK} = \begin{bmatrix} t & n & b \end{bmatrix} \tag{2.15}$$

holds the local tangential t, normal n and binormal b directions of the neutral phase[3] following the Frenet-Formulas.

$$t = \frac{r'}{\|r'\|} = n \times b \qquad n = \frac{t'}{\|t'\|} = b \times t \qquad b = \frac{r' \times t'}{\|r'\| \, \|t'\|} = t \times n \tag{2.16}$$

With this definition of the tangential direction t the Kirchhoff assumption is fulfilled. The cross section is not able to rotate relatively to the neutral phase which avoids possible numerical stiff behavior [38, Remark 3.4]. The complete strain energy can be derived.

$$\frac{\partial}{\partial q_k} \mathcal{V}_\gamma = EA \int_0^L (1 - \frac{1}{\sqrt{r'^T r'}}) r'^T \left[\begin{bmatrix} 0 \\ 0 \\ 0 \end{bmatrix} \quad \frac{\mathrm{d}r'}{\mathrm{d}\Theta} \quad \mathbb{B}'_1 \quad \dots \quad \mathbb{B}'_n \right] d\xi = EA \mathbb{I}_{W\gamma}$$

Curvature energy The measure for the curvature is defined as

$$\kappa = \begin{pmatrix} \tau \\ \kappa_n \\ \kappa_b \end{pmatrix} \tag{2.17}$$

where τ measures the torsion and κ_n and κ_b measure the curvatures in the two planes that are spanned between the tangential vector t and the normal n or the binormal b respectively. The bending and torsional energy derivatives follow.

$$\begin{aligned} \frac{\partial}{\partial q_k} \mathcal{V}_\kappa &= \frac{\partial}{\partial q_k} \mathcal{V}_t + \frac{\partial}{\partial q_k} \mathcal{V}_n + \frac{\partial}{\partial q_k} \mathcal{V}_b \\ &= GI_t \int_0^L \tau \frac{\partial}{\partial q_k} \tau \, d\xi + EI_n \int_0^L \kappa_n \frac{\partial}{\partial q_k} \kappa_n d\xi + EI_b \int_0^L \kappa_b \frac{\partial}{\partial q_k} \kappa_b d\xi \\ &= GI_t \mathbb{I}_{\mathcal{V}t} + EI_n \mathbb{I}_{\mathcal{V}n} + EI_b \mathbb{I}_{\mathcal{V}b} \end{aligned}$$

The single measures have to be found, which is discussed in the following.

For the curvature in the t_{Ref}/n_{Ref}-plane it is crucial to couple the reference deformation and the overlaid effects. Only due to this, the full physics of the ring can be represented. Otherwise, the elastic forces of the reference DOFs would only affect the movement of the reference motion, i.e. the forces would not be projected into the generalized direction of the overlaid DOFs. This would not lead to a circular shape of the curve in case of no external forces. The ratio would shift independently.
To approximate the curvature in the t_{Ref}/n_{Ref}-plane, the second derivative of the position is projected along the reference normal direction.

$$\kappa_n = n_{Ref}^T r'' \quad \text{with} \quad r'' = r''_{Ref} + \mathbb{A}''\mathbb{S}q + 2\mathbb{A}'\mathbb{S}'q + \mathbb{A}\mathbb{S}''q$$

This approximation yields correct measures for the reference part and linearized overlaid measures for the additional deformations. The derivatives wrt. the generalized coordinates follow.

$$\frac{\partial}{\partial s} \kappa_n = 0 \tag{2.18a}$$

[3] These directions do not coincide with the directions from the reference curve as they regard for the local deformations

$$\frac{\partial}{\partial\Theta}\kappa_n = \frac{\partial n_{Ref}^T}{\partial\Theta} r'' + n_{Ref}^T \frac{\partial r''}{\partial\Theta} \tag{2.18b}$$

$$\frac{\partial}{\partial q_{fi}}\kappa_n = n_{Ref}^T \frac{\partial r_f''}{\partial q_{fi}} = n_{Ref}^T \left(\mathbb{A}''\mathbb{S}_i + 2\mathbb{A}'\mathbb{S}_i' + \mathbb{A}\mathbb{S}_i''\right) \tag{2.18c}$$

With the derivatives of $\mathbb{A}$ (Appendix B) one can show that (2.18c) simplifies to

$$\frac{\partial}{\partial q_{fi}}\kappa_n = \begin{bmatrix}0 & -1 & 0\end{bmatrix}\mathbb{S}_i + 2\begin{bmatrix}-1 & 0 & 0\end{bmatrix}\mathbb{S}_i' + \begin{bmatrix}0 & 1 & 0\end{bmatrix}\mathbb{S}_i'' \tag{2.19}$$

for any planar reference curve. Consequently, only the tangential and normal deformation have an influence on the curvature energy.
Analogously, the binormal curvature measure in the t_{Ref}/b_{Ref}-plane is approximated.

$$\kappa_b = b_{Ref}^T r''$$

The derivatives wrt. the generalized coordinates follow

$$\frac{\partial}{\partial s}\kappa_b = 0 \tag{2.20a}$$

$$\frac{\partial}{\partial\Theta}\kappa_b = \underbrace{\frac{\partial b_{Ref}^T}{\partial\Theta}}_{=0} r'' + b_{Ref}^T \frac{\partial r''}{\partial\Theta} \tag{2.20b}$$

$$\frac{\partial}{\partial q_{fi}}\kappa_b = b_{Ref}^T \frac{\partial r_f''}{\partial q_{fi}} = b_{Ref}^T \left(\mathbb{A}''\mathbb{S}_i + 2\mathbb{A}'\mathbb{S}_i' + \mathbb{A}\mathbb{S}_i''\right) = 0 + 0 + \begin{bmatrix}0 & 0 & 1\end{bmatrix}\mathbb{S}_i'' \tag{2.20c}$$

in the case of a planar reference curve. Thus, only the binormal deformation has an influence on this curvature energy.

The torsion

$$\tau = b^T n' = n^T b'$$

is generally defined for spatial curves. Here the reference curve is planar. No torsion is incorporated. Therefore, the following approximation is used for the torsion measure which just takes into account the binormal change due to the overlaid deformations.

$$\tau \approx n_{Ref}^T b'$$

External Forces

External forces from joints or contacts have to be projected into the generalized directions. The Jacobian of translation $\mathbb{J}_T$ has to be found which relates the global free directions with the generalized directions. According to (2.4) it is the transformation matrix $\mathbb{P}$.

$$\mathbb{J}_T = \frac{\partial v}{\partial \dot{q}} = \mathbb{P}$$

Possible link torques are not covered.

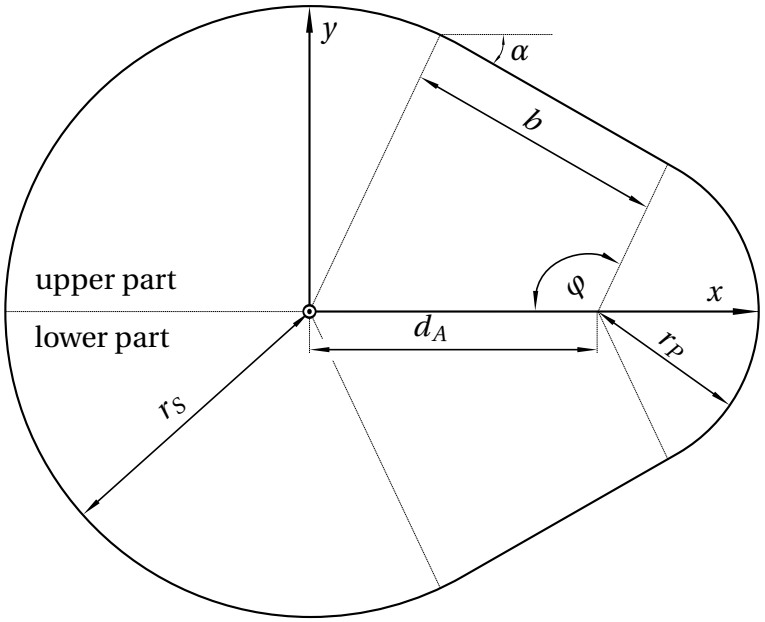

Figure 2.2: Kinematics of a simple reference curve

Equations of Motion

Summarizing the previous findings, one gains the EOMs

$$\mathbb{M}\ddot{q} = h \tag{2.21}$$

where the mass matrix is defined by (2.10) and the right hand side vector h follows with two parts of the kinetic energy and four parts of the potential energy.

$$h = h_{\mathcal{T}1} + h_{\mathcal{T}2} + h_{\mathcal{V}1} + h_{\mathcal{V}2} + h_{\mathcal{V}3} + h_{\mathcal{V}4} \tag{2.22a}$$
$$h_{\mathcal{T}1} = -2\rho A\dot{q}^T \mathbb{I}_{PTdPdt} \tag{2.22b}$$
$$h_{\mathcal{T}2} = \rho A\dot{q}^T \mathbb{I}_{PTdPdqi}\dot{q} \tag{2.22c}$$
$$h_{\mathcal{V}1,k} = -EA\mathbb{I}_{\mathcal{V}\gamma} \tag{2.22d}$$
$$h_{\mathcal{V}2,k} = -EI_n\mathbb{I}_{\mathcal{V}n} \tag{2.22e}$$
$$h_{\mathcal{V}3,k} = -EI_b\mathbb{I}_{\mathcal{V}b} \tag{2.22f}$$
$$h_{\mathcal{V}4,k} = -GI_t\mathbb{I}_{\mathcal{V}t} \tag{2.22g}$$

Kinematics of the Reference Curve

The derived EOMs are valid for any belt system with a planar reference curve. For the application within the CVT system the following reference curve is chosen. To be consistent with the general kinematic description – especially concerning (1.3) – the following values should carry the index ref. It is omitted in this subsection for the sake of clearness. All kinematical values refer to the center line of the beam model.

It consists of four parts which are depicted in Figure 2.2:

- primary arc with radius r_P and with length $b_P = 2r_P(\pi - \varphi)$
- upper strand with length $b = d_A \cos\alpha$
- secondary arc with radius r_S and with length $b_S = 2r_S\varphi$
- lower strand with length b

with the relations

$$\alpha = \arcsin\left(\frac{r_S - r_P}{d_A}\right) \quad \text{and} \quad \varphi = \arccos\left(\frac{r_P - r_S}{d_A}\right).$$

The ratio parameter Θ is chosen such that symmetric properties can be used for numerical evaluation. It holds the following relationship to the geometric ratio of the reference curve $i_{g,ref} = \frac{r_S}{r_P}$.

$$\Theta = \frac{1 - i_{g,ref}}{1 + i_{g,ref}} \quad \Leftrightarrow \quad i_{g,ref} = \frac{1 - \Theta}{1 + \Theta} \tag{2.23}$$

The nonlinear function to calculate the primary radius for a specific geometric ratio, i.e. a specific value of Θ, is

$$0 = L - 2b - b_P - b_S \tag{2.24}$$

where the constraining parameters to the system are d_A – the distance between the pulley axles – and L – the total length of the ring.
In a preprocessing step the arc-radii for different Θ are computed solving the nonlinear system (2.24). The primary radius r_P over the ratio parameter Θ with at least[4] C^2-continuous splines is interpolated. An explicit dependency $r_p(\Theta)$ results. The further kinematic description over the arc follows also explicitly and is C^1-continuous in ξ.

For a given interpolated function of the primary radius $r_P(\Theta)$, the positional description over the arc length ξ for the upper part is given by

$$r^u = \begin{pmatrix} r_x^u \\ r_y^u \\ 0 \end{pmatrix} = \begin{cases} \begin{pmatrix} -r_S\cos(\varphi_S) \\ r_S\sin(\varphi_S) \\ 0 \end{pmatrix} & \text{if } 0 \le \xi \le \varphi r_S \\ r_{S,end} + \xi_T t_T & \text{if } \varphi r_S < \xi \le r_S\varphi + b \\ \begin{pmatrix} d_A - r_P\cos(\varphi_P) \\ r_P\sin(\varphi_P) \\ 0 \end{pmatrix} & \text{if } \varphi r_S + b \le \xi \le \frac{L}{2} \end{cases} \tag{2.25}$$

with the following definitions

$$\varphi_S = \frac{\xi}{r_S}, \qquad \xi_T = \xi - r_S\varphi, \qquad \xi_P = \xi - r_S\varphi + b, \qquad \varphi_P = \varphi + \frac{\xi}{r_P},$$

[4] See (B.1)

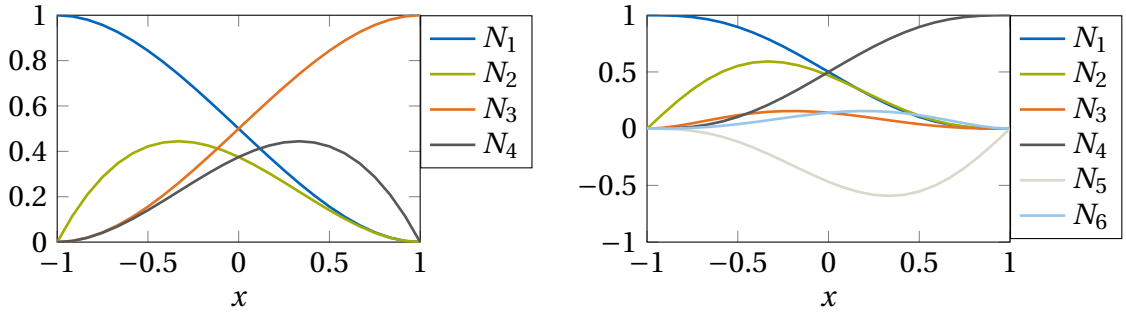

Figure 2.3: Sketch of the Hermite ansatz functions for the C^1-continuous case (left) and C^2-continuous case (right) case.

$$r_{S,end} = \begin{pmatrix} -r_S \cos\varphi \\ r_S \sin\varphi \\ 0 \end{pmatrix}, \qquad r_{P,start} = \begin{pmatrix} d_A - r_P \cos(\varphi) \\ r_P \sin(\varphi) \\ 0 \end{pmatrix}, \qquad t_T = \frac{r_{P,start} - r_{S,end}}{\left| r_{P,start} - r_{S,end} \right|}.$$

The lower part follows due to symmetry.

$$r^l(\xi) = \begin{pmatrix} r_x^u(\xi - L) \\ -r_y^u(\xi - L) \\ 0 \end{pmatrix} \tag{2.26}$$

Ansatz functions

The ansatz functions for the FE are integrated over the whole length L. Hermite interpolation ansatz functions are chosen to respects the necessity of C^1-continuity for the planar case without torsion and C^2-continuity for the spatial case. The Hermite polynomials are used as they are depicted in Figure 2.3. The formulas follow for

... the C^1-continuous case

$$N_1 = \frac{1}{2} - \frac{3}{4}x + \frac{1}{4}x^3, \qquad N_3 = \frac{1}{2} + \frac{3}{4}x - \frac{1}{4}x^3$$
$$N_2 = \frac{l_e}{8} - \frac{l_e}{8}x - \frac{l_e}{8}x^2 + \frac{l_e}{8}x^3, \qquad N_4 = \frac{l_e}{8} + \frac{l_e}{8}x - \frac{l_e}{8}x^2 - \frac{l_e}{8}x^3$$

... the C^2-continuous case

$$N_1 = \frac{1}{2} - \frac{15}{16}x + \frac{5}{8}x^3 - \frac{3}{16}x^5, \qquad N_4 = \frac{1}{2} + \frac{15}{16}x - \frac{5}{8}x^3 + \frac{3}{16}x^5,$$
$$N_2 = \frac{l_e}{32}\left(5 - 7x - 6x^2 + 10x^3 + x^4 - 3x^5\right), \qquad N_5 = \frac{l_e}{32}\left(-5 - 7x + 6x^2 + 10x^3 - x^4 - 3x^5\right),$$
$$N_3 = \frac{l_e^2}{64}\left(1 - x - 2x^2 + 2x^3 + x^4 - x^5\right), \qquad N_6 = \frac{l_e^2}{64}\left(1 + x - 2x^2 - 2x^3 + x^4 + x^5\right)$$

where l_e is the element length.

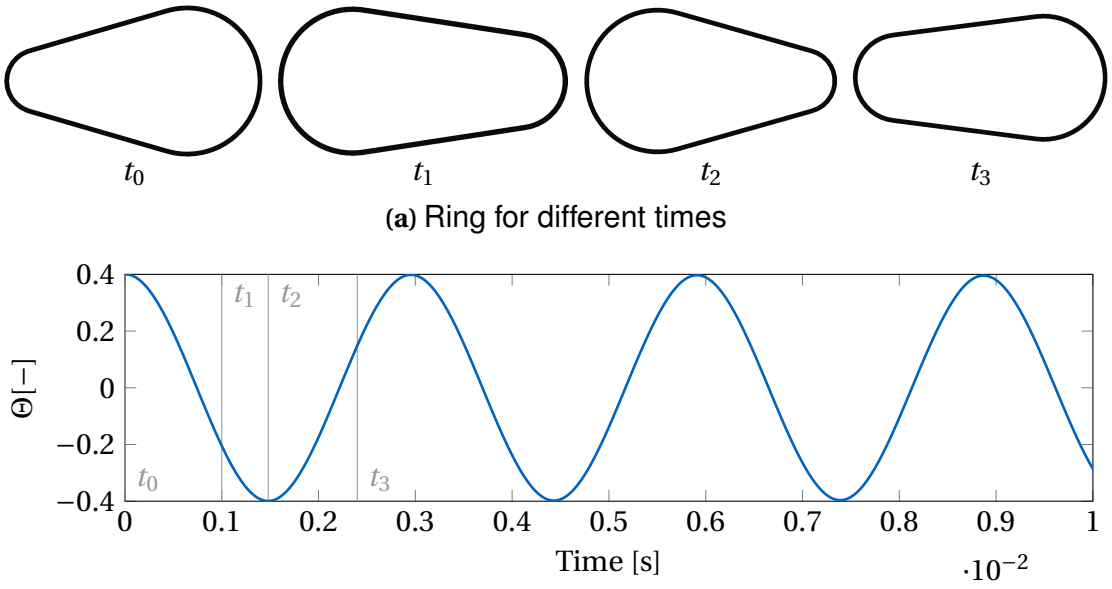

(a) Ring for different times

(b) Oscillation of reference parameter Θ

Figure 2.4: Time development of reference oscillation

Remarks

The equations are implemented and tested qualitatively in the following. The first virtual experiment tests the dynamics of the reference kinematics only, i.e. $q_f = 0$. The parameters follow a real ring such that the stiffness is incorporated. The starting condition is $\Theta = 0.4$, $s = 0$ and $\dot{\Theta} = \dot{s} = 0$, i.e. an OD-ratio of $i_g \approx 0.4286$ is set. Results are depicted in Figure 2.4a for the deformation of the ring. Four different time points are given where t_0 is the start position. At t_1 an intermediate state is given. One can see that the ratio changes over time and oscillates around the neutral state $\Theta = 0$. This oscillation is given in Figure 2.4b. The parameter s stays zero – it is only numerically affected. Keeping in mind, that the local deformations are blocked, this is the expected result.

For a general model with all DOFs, one would expect a circular shape as neutral state. Therefore, another experiment is performed adding the local deformations. Thereby, another problem rises. As the local deformations build a full space, the position is redundantly described taking into account also the reference DOFs. Practically, the mass matrix becomes singular. Therefore, two local DOFs directions are locked, i.e. one node is fixed at its reference position. It moves due to the reference coordinates within the xy-plane. For this experiment and for the whole work the first node is chosen, which is at $\xi = 0$.
The same parameters are chosen as before. Cubic ansatz functions within eight FEs are selected. All generalized positions and velocities $q = \dot{q} = 0$ at $t_0 = 0$. The positional development is depicted in Figure 2.5 for four different times in chronological order. One can see that at t_1 the ring shows a reasonable behavior. Similar to a rubber band, it starts to form a circular shape. The strands deform outwards. At t_2 however, no reasonable development is observed. The first node[5] can only move with the reference DOFs, i.e. Θ in this case. To form a circular shape, the left node has to move to the center, i.e. Θ increases. The typical shape of the CVT ring for $\Theta > 0$ can be seen as Θ influences the deformation over the whole arc. Yet, the deformation develops further yielding an oval-like shape again at t_3, which is the expected

[5] here on the left side of the ring

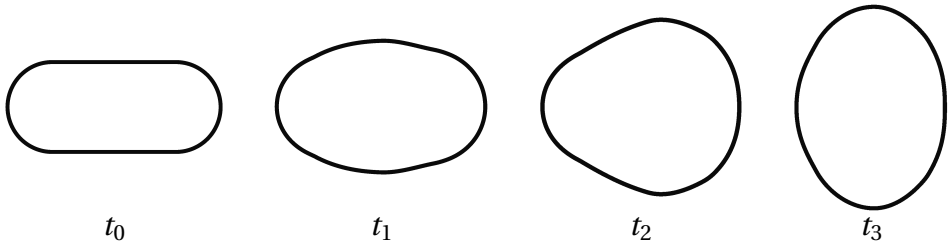

Figure 2.5: Time development of a deformable ALE ring with 8 FEs and cubic hermite ansatz functions.

behavior.
With this example two points should be emphasized. On the one hand the presented model relies on the description of the reference curve. One could say that the model assumes an external force distribution that yields a shape similar to the one of the reference configuration. Only small deviations from the reference are assumed. Then the motion is reasonable ($t_0 \rightarrow t_1$). On the other hand the model has all DOFs of a general model and develops (qualitatively) correct, as one can deduce from the above discussion for $t_1 \rightarrow t_3$.

Further Consideration

The presented model has been developed for the application within a spatial pushbelt CVT. The idea – known from e.g. the FFR-method – was to describe the nonlinear reference motion and additional small deviations separately. This idea leads to successful tests as shown above and which is confirmed later in this work. The possibilities that result for further applications are therefore given here in addition.

Application to other belt systems The presented approach is not restricted to the pushbelt CVT system. It could be used for any belt system with a closed one-dimensional curve and a reference kinematics.

Separated integration The separation of the reference and the overlaid deformation also enables the possibility to separate these DOFs in the integration. It can be assumed that the two reference DOFs change only slowly compared to overlaid deformation and must not be updated in every time step. It reduces the simulation costs and might increase robustness of the overall system as the dynamical coupling of the DOFs is reduced.

Reduction A nonlinear reduction technique, i.e. the proper orthogonal decomposition, could not be performed successfully for the LRVM model in the CVT application. The coupling of the overall movement within the framework of Lagrange description with local small deformation is assumed to be the reason for this as the technique needs to identify both movements separately. Following this consideration, the Eulerian framework in combination with the reference curve description offers the possibility to only reduce the overlaid deformations with techniques known from linear systems.

Overlaid deformation fields The evaluation of the presented integrals is time consuming and yields the most computational costs. For an overall good approximation the two reference DOFs give good results (Section 3.3). However, the spiral running in the arcs is not represented which results in small deviations.

From the overall state of the variator it is possible to approximate the kinematics of the ring. The small deviations could be set as a quasi-static overlay omitting their dynamic integration. Besides the spiral running, this idea can be adapted for the misalignment. The deviations of the rings can be deduced from the sheave positions as it is done for the initialization in [54]. The stiff behavior in binormal direction must not be treated dynamically. Therefore, the spatial dynamics of the elements would still be included and thus the influence of it on the system can still be studied.

2.2 Interactions

The torque transmission is driven by friction in the CVT. The interaction models, i.e. the contacts, are thus a major task within the corresponding MBS. Assumptions concerning the kinematics, e.g. surfaces of the contacting bodies, as well as on the kinetics, e.g. the local contact stiffness, determine the trajectories of the simulation. The models of the prior works are analyzed in this section, which yields enhancement ideas that are derived.

The thickness of the element is discussed at first in Subsection 2.2.1. A variable number of simulated elements leads to variable stiffness and has a remarkable influence on the global output of the simulation. Adjustment formulas solve the problem of varying stiffness.
For the element-pulley contact a new contact kinematics enables further variator geometries as discussed in Subsection 2.2.2. Simplifications are introduced wrt. to the solution of the coupled contact force law for the planar case.
The longitudinal stiffness of the belt influences the OEP within the variator and thus the efficiency of the whole system. To represent the stiffness in the element-element contact correctly, measurements of a specified test-setup are compared to simulations in Subsection 2.2.3. Numerical optimization techniques are used to enhance the parameters of the local stiffness curves.
Finally, the contact between elements and rings is discussed in Subsection 2.2.4. Nonphysical effects arise within the prior spatial model that are solved with a new contact kinematics. The ring-tracking law of [9] is addressed at the end. A new model respecting the normal force influence on the tracking behavior is presented.

2.2.1 Element Thickness

In the simulation N_E number of elements are used whereas the belt comprises N_{E0} elements in reality, which yields the ratio ι.

$$\iota = \frac{Ne0}{Ne} \tag{2.27}$$

The thickness and inertia are adjusted accordingly [54, p. 19]. The stiffness for the contacts is affected as well which is addressed in the following.

In the simulation an element carries the force $F_s(g)$ where g is the contact penetration, i.e. the gap. Kinematic compatibility between different simulations is required, e.g. the simulations use the same sheave stiffness for all cases. This requires the same deformation and thus the same g. For contacts where the force function is proportional to the element thickness t with $F_{sim}(g) \propto t$ the adjustment of (2.27) has to be taken into account.

Consider the force function $F_m(g)$ of a measured element for its complete virtual[6] length $\hat{l}$. The change of the length is identified with $\Delta\hat{l} = g$. Due to Hooke's law, this stiffness can be related to the geometrical and material properties of the element with

$$F_m \propto \sigma_m \hat{A}_m = \hat{A}_m E_m \varepsilon_m = \hat{A}_m E_m \frac{\Delta\hat{l}}{\hat{l}_m} = \hat{A}_m E_m \frac{g}{\hat{l}_m} \qquad \Rightarrow F_m \propto \frac{\hat{A}_m}{\hat{l}_m}$$

where σ is a tension measure, ε a strain measure, E_m the Youngs modulus and $\hat{A}_m$ the virtual cross section of the measured element. One realizes, that the thickness t of the element either affects $\hat{l}$ or $\hat{A}$ – depending on the specific contact situation. The contact force on the simulated element differs from a contact force on the real element.
In the simulation three contacts are affected where the local force function is influenced in different ways.

Contact to sheaves It is required that the sheaves deform in the same way for different simulations to guarantee the same force distribution along the arc and thus e.g. the same spiral running. Here the element flank is in contact and therefore the virtual cross sections $\hat{A}_{ElSh}$ change with ι. Thus, the element in the simulation has to carry a higher[7] load.

$$F_{s,ElSh} \propto \iota F_{m,ElSh} \tag{2.28}$$

In case of two contact points on one flank, e.g. a front and a rear contact, $\hat{A}_{ElSh}$ is halved.

Contact to rings The kinematic influence of this contact situation is of minor significance. To achieve same running radii, the virtual cross section, i.e. saddle and ear, $\hat{A}_{ElLS}$ changes with ι. The following adaption is suggested.

$$F_{s,ElLS} \propto \iota F_{m,ElLS} \tag{2.29}$$

Contact to elements To represent the OEP correctly one has to adapt the element-element force function. For the contact to other elements the thickness of the elements affects the virtual length $\hat{l}$, i.e. $\hat{l}_s = \iota\hat{l}_m$. It carries less load for the same penetration.[7] As the transmitted force is prescribed by the boundary conditions, the practical implication is, that a simulated element gets compressed more the thicker it gets, i.e. for decreasing N_E.

$$F_{s,ElEl} \propto \frac{1}{\iota} F_{m,ElEl} \tag{2.30}$$

It is clear that with N_E more than the discussed points are varied. One major influence is that the dimension of the system for the solution of the coupled contact law increases. The solution gets more precise with increasing N_E and a varied force distribution is found. This is not included theoretically.
Here simulations test the system using only simple regularized contact laws with decoupled deformations. Two simulations are performed. One uses $N_E = 160$ and the other $N_E = 220$. For both cases either the adaption is used or not. The results are shown in Figure 2.6.

[6] Virtual indicates here, that the length is the deformation direction within the element
[7] Assuming $N_E < N_{E0}$

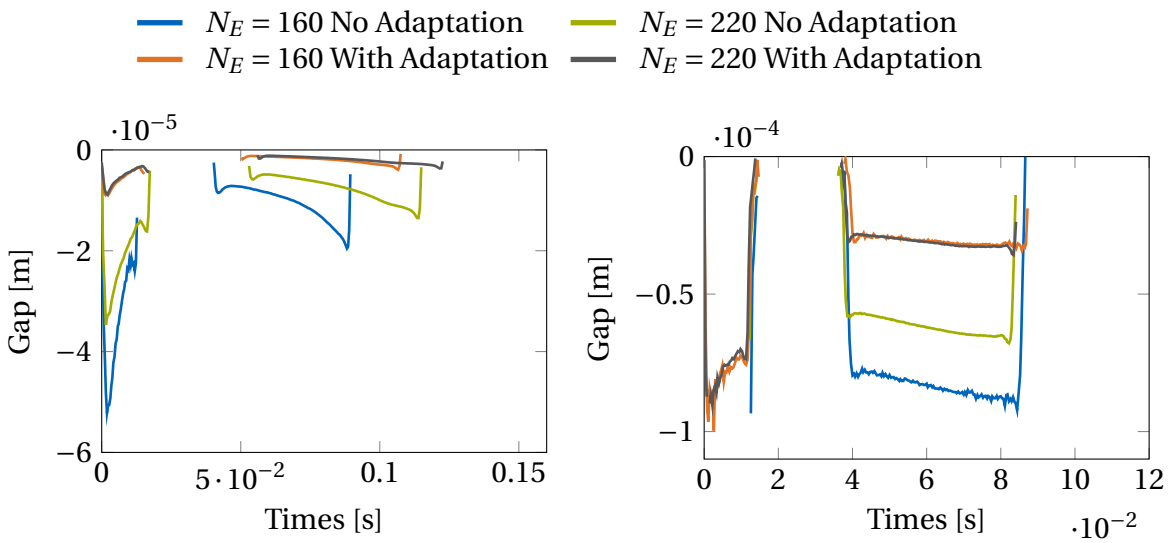

(a) Compression at the element-pulley contact on the right flank.

(b) Compression at the element-ring contact.

Figure 2.6: Contact gaps of simulations with or without the stiffness adaption

Both plots prove the ideas of the discussion to be valid. For simulations where the adaption is used, the contact gaps are the same disregarding small deviations. Simulations without the adaptions and using a different number of elements, i.e. elements with different thicknesses but same stiffness values, have different penetrations changing the overall kinematical output. The gap is overall smaller for simulations with the adaption. The adaption should lead to kinematics resulting from the "real" situation, i.e. the measured force function $F_{m,*}$. As more elements exist[7] less penetration results confirming the above considerations.

2.2.2 Element-Pulley

It is clear, that the correct representation of the element-pulley interaction plays an important role within the CVT. Sheave deformation is a major effect, which causes spiral running. Friction limits the transmittable torque for a certain clamping force. The kinematics influence the misalignment and the local force directions.
Curved sheaves are used in chain CVTs [31, p. 56]. They can eliminate misalignment in case of optimal geometry [19]. Specific contact kinematics between arbitrary convex sheaves and a spherical flank contour are derived in the following. Different coupling models of the force laws are introduced in Subsection 2.3.2.

Curved Sheaves

In prior models only flat sheaves are considered [25, 54, 9]. To enable generally curved pulley-sheaves a polynomial description for the radius $r(x)$ is used along the local height direction x as given in Figure 2.7a with

$$r(x) = \sum_{i=0}^{n} a_i x^i \tag{2.31}$$

where n is the order of the polynomial and a_i the polynomial coefficients. The frame xyz with the origin O_F is attached to the frustum and is used for the following considerations. Its

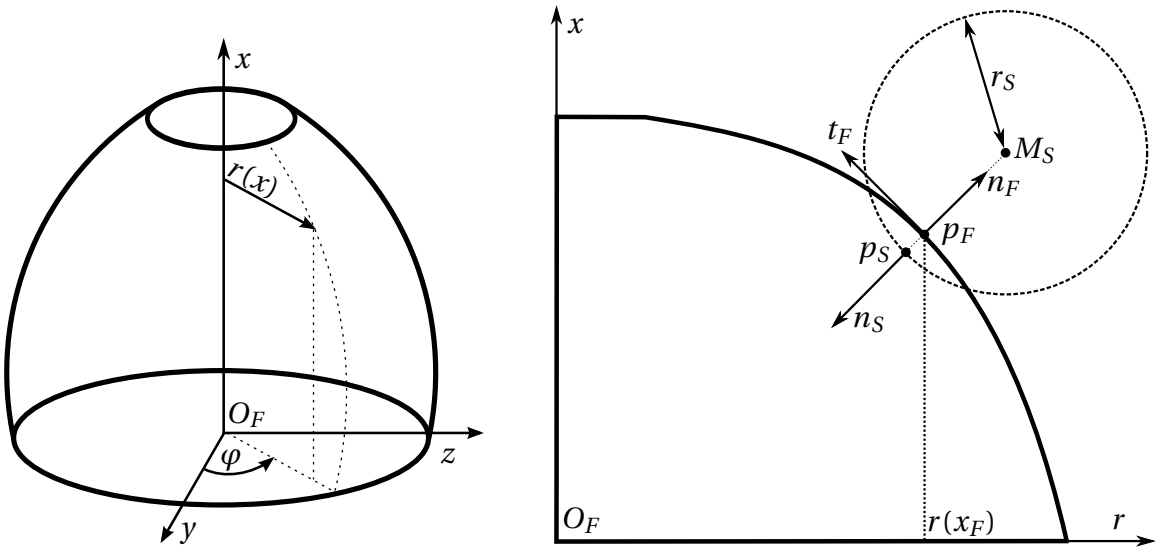

(a) Generally curved sheave

(b) Contact kinematics: polynomial frustum and sphere

Figure 2.7: Generally curved sheave represented as polynomial frustum in contact with spherical element flanks.

index is omitted. The flanks of the elements are described with a sphere to respect possible slight curvatures of the flank as well [54].
Figure 2.7b shows the kinematics between polynomial frustum and sphere. The point $M_S^T = \begin{bmatrix} m_{s_x} & m_{s_y} & m_{s_z} \end{bmatrix}$ is the center of the sphere with the radius r_S. At the contact positions p_* the respective normal n_* points outwards. The tangent to the frustum is t_F. As the normal to the sphere n_S runs through M_S, the contact problem can be reduced to a planar circle-polynomial contact. The plane is defined by x and M_S. The azimuthal coordinate can be determined by $\varphi_F = \tan^{-1}(\frac{m_{s_y}}{m_{s_z}})$. It follows for the planar point on the frustum

$$p_F = \begin{pmatrix} x_F \\ r(x_F) \end{pmatrix} \qquad \text{and} \qquad t_F = \frac{\partial}{\partial x} p_F = \begin{pmatrix} 1 \\ r'_F \end{pmatrix}$$

with the tangent t_F to the point in the plane where $r'_F = r'(x_F)$ being the derivative of the radial coordinate wrt. x. The midpoint of the sphere in the plane (index 2D) follows.

$$M_{S_{2D}} = \begin{pmatrix} m_{s_x} \\ \sqrt{m_{s_y}^2 + m_{s_z}^2} \end{pmatrix} = \begin{pmatrix} m_{s_x} \\ r_s \end{pmatrix} \tag{2.32}$$

The vector $p_F - M_S$ is collinear to the normal n_S and thus has to be orthogonal to t_F.

$$\left(p_F - M_{S_{2D}}\right) \cdot t_F = 0 \quad \Leftrightarrow \begin{pmatrix} x_F - m_{s_x} \\ r_F - r_S \end{pmatrix} \cdot \begin{pmatrix} 1 \\ r'_F \end{pmatrix} = 0 \quad \Leftrightarrow x_F - m_{s_x} + r'_F r_F - r'_F r_S = 0 \tag{2.33}$$

Equation (2.33) is sufficient to find the x-coordinate on the frustum. Thus all kinematics are defined. Remark that for $r_S = 0$ the description is valid for a point contour, e.g. chosen as fixed point on the element flank, as well.

Coupling the flanks

CEBULLA uses a coupled force law to represent the sheave deformation along the arc using Maxwell influence numbers [71, 29, 11]. Besides the stiffness of the pulley-sheaves – repre-

sented by $C_{sh,l}$ for the loose sheave and $C_{sh,f}$ for the fixed sheave – the axial stiffness c_{ax} of the elements is incorporated as well in the matrix C_{ax} in [9, eq. (5.57)][8] yielding

$$\begin{pmatrix} g_l \\ g_f \end{pmatrix} = \left(\begin{bmatrix} C_{sh,l} & 0 \\ 0 & C_{sh,f} \end{bmatrix} + \begin{bmatrix} C_{ax} & 0 \\ 0 & C_{ax} \end{bmatrix} \right) \begin{pmatrix} \lambda_l \\ \lambda_f \end{pmatrix} + \begin{pmatrix} \tilde{g}_l \\ \tilde{g}_f \end{pmatrix} \tag{2.34}$$

where g_* are the contact gaps after applying the contact forces λ_* and $\tilde{g}_*$ are the contact gaps before the contact. The influence matrix $C = \sum_* C_*$ couples the forces and local deformations. For a diagonal matrix C the single contact positions are decoupled and the solution of λ is gained explicitly. This is referred to as regularized contact law. The representation of (2.34) decouples the left and the right flank of one element, i.e. C is block-diagonal. Both flanks may deform differently. Different flank forces result, i.e. $\lambda_l \neq \lambda_f$, and lead to a movement of the element. In the planar case the kinematics of the element is constrained in the axial direction thus the local force equilibrium might not be fulfilled everywhere.
GEIER uses a coupling of both flanks yielding an overall element deformation.

$$g_{l/f} = \left(C_{sh,l} + C_{sh,f} + C_{ax} \right) \lambda_{l/f} + \tilde{g}_{l/f} \tag{2.35}$$

The influence matrices of the loose sheave $C_{sh,l}$ and fixed sheave $C_{sh,f}$ are added together. This yields the same contact forces at the left and the right flank, i.e. $\lambda_l = \lambda_f$. This halves the system dimension or practically leads to one instead of two LCPs for each pulley.

2.2.3 Element-Element

A special feature of the present model is the separation of single elements. This implies, that the belt is not continuous and the elements may separate, e.g. in the loose-strand. Thus, for this strand there is no contribution to the global torque equilibrium due to push-forces, e.g. $F_{Pl} = 0$ in Figure 1.2. The length of the elongated rings, the number of elements in reality N_{E0}, the variator shape and the compression of these due to the applied loads determine the OEP. While the material parameters of the rings can be measured well, the correct representation of the element's compression is a more delicate task. Production uncertainties yield nonlinear stiffness behavior.
Experiments were conducted to measure an overall stiffness. The setup is explained at first which is referred to as Push-Force-Tester. Then, the model is derived using the same submodels as for the full simulation. It is used to update of the crucial parameters in a second step.

Push-Force-Tester – Setup

In Figure 2.8a the setup of the experiment is sketched. The belt with n elements is clamped between a left and a right hinge point. The rings are clamped with a construction where c_{cl} measures its stiffness. It is chosen to be much stiffer as the combined belt stiffness such that its effects on the system is neglected. The clamped ends do rotate with the hinges, such that the tangents at the end of the rings point towards the respective hinge point. The elements

[8] Here the index el is changed to ax to emphasize that it is indeed the axial stiffness acting of the element and that the deformation is depending on the respective direction.

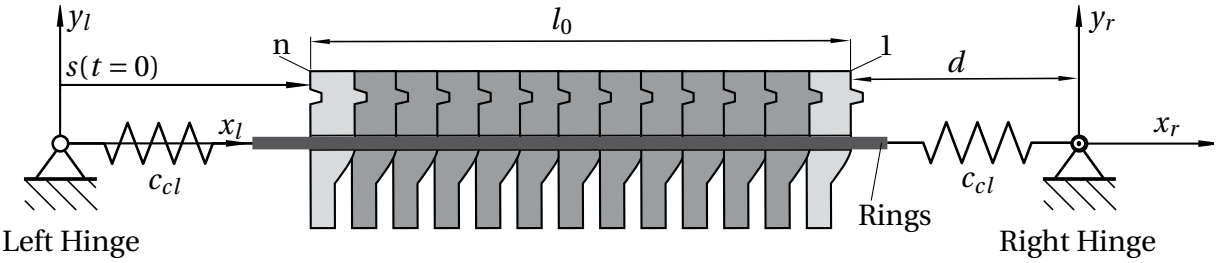

(a) Setup of Push-Force-Tester before the compression

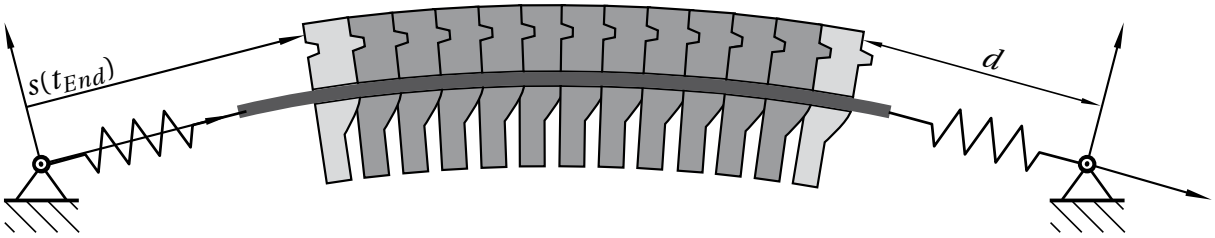

(b) Possible condition of Push-Force-Tester after the compression

Figure 2.8: Setup of the Push-Force-Tester before and after the compression forming a "cats back".

are guided by the rings. Element 1 at the right end is fixed, such that it only rotates around the right hinge point and has the constant distance d to it. Element n at the left end rotates with the left hinge point. Its distance from it is prescribed with $s(t)$. At the beginning, the assembly is arranged such that there are no forces acting between the aligned elements. The stack up has the length l_0. The rings are prestressed with a force F_{PS}. The compression leads to contact forces at the RE and the head. To minimize the compression energy, the belt deforms and builds up a curvature. Either a "cats back", i.e. a deformation upwards (Figure 2.8b), or a "dogs back", i.e. a deformation downwards, could be formed. It depends on the relation of the stiffness at the head and the RE as well as on the geometric design, i.e. the distances of these two contact points to the saddle or the ear.

In the experiment the clamping force F_{CL} at element 1 is measured. The nondimensional deformation measure $\xi_{PFT} = \frac{s(t)}{l_0}$ is used. A force function $F_{CL}(\xi_{PFT})$ results. Measurements were conducted by BTT. The elements show a nonlinear deformation behavior as exemplary shown in Figure 2.9. This curve can be approximated by

$$F(\xi) = \begin{cases} 0 & \forall \xi < 0 \\ a\left(\mathrm{e}^{k\xi} - 1\right) & \forall 0 \le \xi < \xi_0 \\ c\xi + d & \forall \xi \ge \xi_0 \end{cases} \tag{2.36}$$

with the Eulerian number e and the parameters c, ξ_0 and k. The values of a and d ensure C^1-continuity between the exponential and the linear part. The parameters can be interpreted as follows:

c Is the linear stiffness parameter and holds when the belt shows no (measurable) nonlinear behavior.

ξ_0 Is a non-dimensional parameter holding the transition point from linear to nonlinear part.

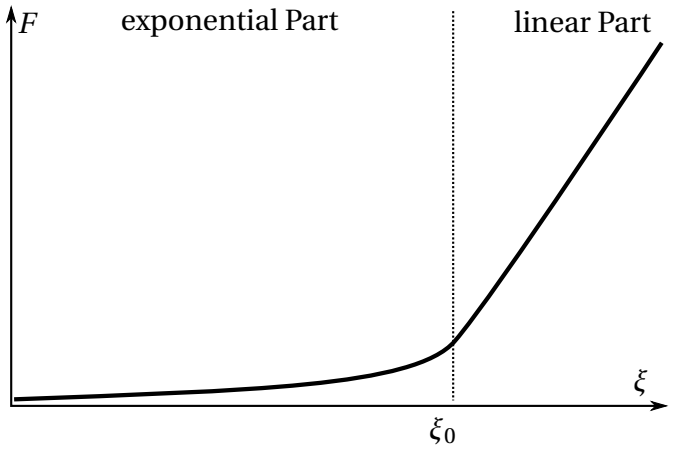

Figure 2.9: Example curve gained from Push-Force-Tester measurements

k Is a measure for the nonlinearity in the exponential part. The lower this value the steeper the increase in the nonlinear part.

Push-Force-Tester – Model

The discussion above addresses the global deformation of the belt. It is assumed, that the measured nonlinearity of the overall system is driven by the deformation of the elements. Thus, for the local deformation at RE and head the same function is used. The function is evaluated at

$$\xi = \frac{g}{t_{loc}}$$

where g is the contact penetration, which is gained during simulation. The medium local thickness t_{loc} takes into account the thicknesses of the two neighboring elements which may differ for head or RE. Thereby, the considerations of Subsection 2.2.1 are respected. The contact law does not assume elements with equal thicknesses as done in [25, 54, 9]. It can be used with a belt consisting of different elements as in [44].
The Push-Force-Tester system described above has been modeled with the same objects as used in the full CVT system. The new contact law is used, as the parameters are physically better interpretable as e.g. in [54, eq. (2.174)].

Updating

The model is used to determine the six[9] stiffness parameters. Besides the combined deformation of the head and the RE, the measurement includes also deformation energies from the rings. The local contact laws are therefore not directly gained from the global measurement curve but optimization of the single parameters has to be preformed. Standard integration schemes, which take into account the full dynamics of the system, appeared to be inefficient. The system shows numerically very stiff behavior. Only very slow movements of element n are possible to guarantee a quasi-static output.
A quasi-static integrator[10] has been applied to the system which is described in the following.

[9] three at the RE and three at the head

[10] The author wants to acknowledge the support of his student worker Zhan Wang for the implementation.

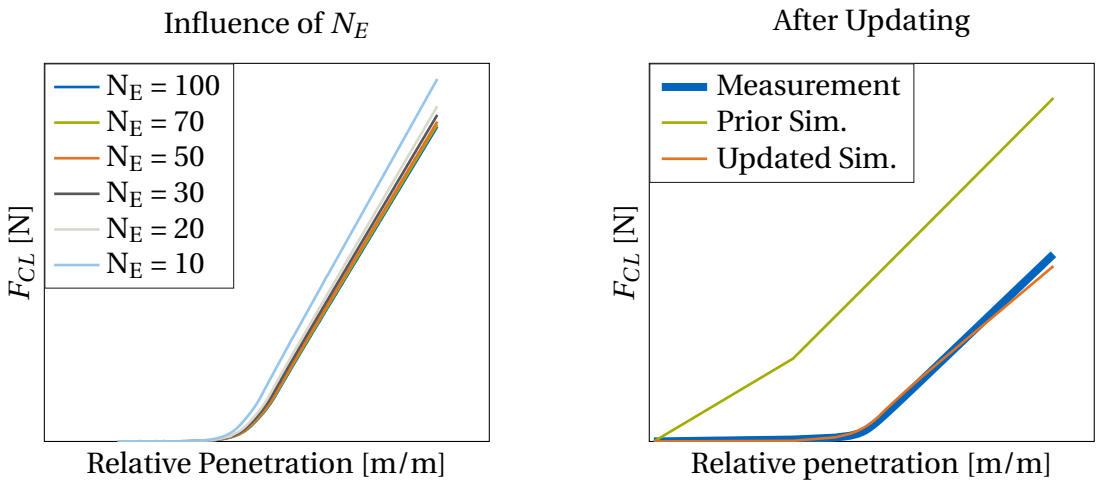

Figure 2.10: Results of the simulations using the Push-Force-Tester system. Measurements were made available by BTT.

The generalized velocities u and their time derivatives $\dot{u}$ are set to zero for a static result. Equation (1.7) is solved as a nonlinear system such that the solution to the following system has to be found.

$$0 = h(q) + W(q)\lambda \tag{2.37a}$$

$$0 = f(q) \tag{2.37b}$$

In (2.37b) the constrained conditions are represented with nonlinear functions f using proximal point projections as in (1.12). Remark that only the generalized positions q have to be found.
A Newton algorithm as in [72, Algorithm 2.11] is used and the stop criteria compares the infinity norms of (2.37a) and (2.37b) separately concerning respective tolerances, i.e. tol_h and tol_f. In practice, the algorithm converges robustly only when all set-valued force laws are regularized. Is the whole system in the linear part, i.e. $s(t) > \xi_{PFT} l_0$, a linear extrapolation for the generalized positions with

$$q^i \approx 2q^{i-1} - q^{i-2}$$

is used as starting point for the Newton algorithm for time step i. It reduces the iteration steps up to 80%.

To enable a fast updating process, the influence of N_E is analyzed to minimize it. The results are shown in Figure 2.10 on the left side. It can be seen that the less elements are used in the simulation the stiffer the behavior of the system gets. The elements get thicker as less are used. The contact kinematics at the RE limit the movement stronger, i.e. the cat's-back is formed only with higher loads. Therefore, the rings bend less for the same load but elements compress stronger yielding a stiffer behavior in the linear part.
Two conclusion can be drawn. On the one hand it is evident that the nonlinearity of the Push-Force-Tester is not solely driven by the elements. On the other hand it makes clear that also the geometric changes due to N_E affect the system. This is discussed in Section 3.1 concerning the CVT system. For the updating process a compromise of $N_E = 30$ is chosen. The final force deviates less than 4% to the reference value of the simulation with $N_E = N_{E0} = 100$.

An optimization process is performed to identify the parameters. The MATLAB function `fmincon` from the Optimization Toolbox [43] is used. The results are shown in Figure 2.10 on

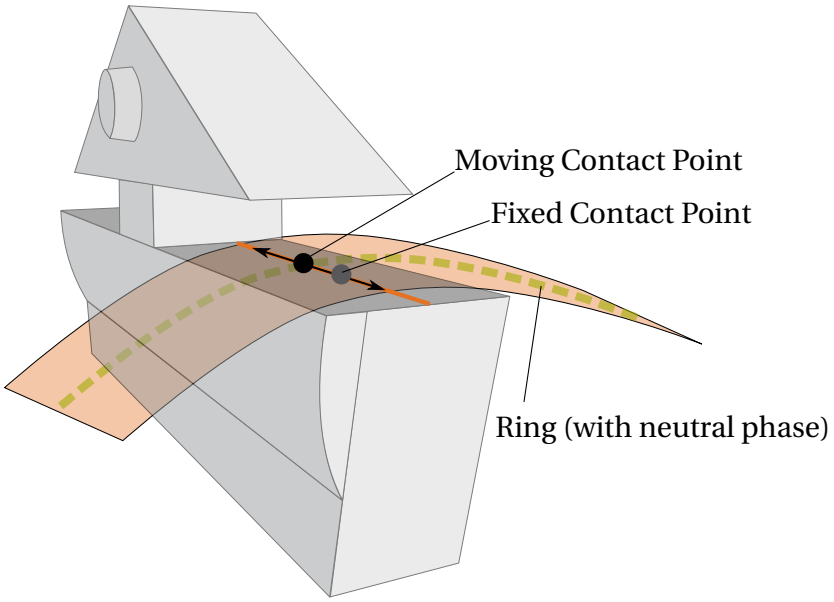

Figure 2.11: Contact situation between element and ring

the right side. It can be seen that the prior models of [25, 54, 9] used stiffer elements whereas the updated parameters show a very good match with the measurement curve that is within measurement uncertainty.
The updating process yields parameters for the RE- and head-contact law. For both contact positions the parameters are nearly the same, i.e. $\frac{F_{\text{head}}(\xi)}{F_{\text{RE}}(\xi)} \approx 1 \forall \xi$. To quantify the differences between both contact positions more measurement data should be made available. Besides the stiffness curve itself, the partition of head and RE forces could be used. Furthermore, kinematic data, e.g. the ring lift, could be used to identify not only the stiffness-parameters but the geometric data of the elements as well.

2.2.4 Element-Ring

The interconnection between elements and rings is locally a delicate problem and should be analyzed in detail. In this work however suitable models for the application within MBSs are needed which cannot represent all details. In [54, 9] predefined contact points on saddle and ear of the element were used yielding good results within a planar simulation. For the spatial representation however this model is not suitable anymore. This section treats two improvements concerning the element-ring contact situation. The contact kinematics is analyzed. It is found that a fixed point should be replaced by a line search to avoid unphysical torques around the neutral phase of the ring. The detailed analysis of the stress distribution between element and ring discusses tracking effects and leads to an improved tangential tracking law.

Contact Kinematics

In contrast to the planar model, rings and elements move relatively in axial direction in the spatial case. Figure 2.11 visualizes the situation where the ring moves towards the pillar of the element. For a fixed contact point the contact normal force leads to a torque around the neutral phase. Yet it is clear, that the ring is in contact with the complete saddle in reality. This

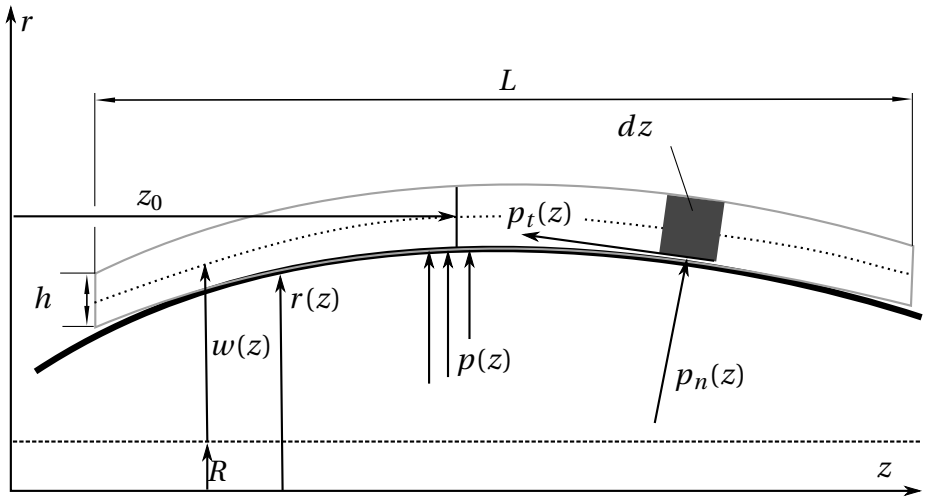

Figure 2.12: Tracking situation between element and ring

should be represented by a pressure distribution along the axial direction.
A discretization of the line with a certain number of contact points is impractical. The kinematical update of the contact kinematics are dominated by the search between element and ring. It is already a main driver of the computational cost [54, p. 68]. These costs are avoided by an enhanced contact kinematics resulting in one contact point. Instead of a one dimensional search along the center line of the ring, a two dimensional search including the axial direction is used. This ensures that the contact point is always at the center line of the ring. No unphysical torques lead to torsion in the ring. Virtual experiments with a simpler pulley set show a numerical stabilized behavior.

Ring Tracking

Misalignment between the two pulley sets deform the rings in axial direction. The inner tension in the ring, that tends to bend it straight, is in equilibrium to external forces applied on the element saddle. In [54, 9] linear and nonlinear tracking laws depending solely on the axial position of the ring are used. Both disregard the actual underlying mechanics. The external force is a result of the contact between ring and saddle and with it depends on the normal pressure between both. In the following, a tracking law based on the local force distribution is derived which is applicable within MBSs.[11]

Background Assume the general contact between a belt and a ground as given in Figure 2.11. The surface of the ground is described in a local coordinate system with $r(z)$ and changes in direction of the width z. A belt runs over this surface. On an infinitesimal part of the belt dz at position z a pressure acts in normal direction $p_n(z)$ and in tangential direction $p_t(z)$.

Point of Departure BENSON and D'ERRICO couple the deflection of a web $u(z) = R + w(z)$ with the radial forces $p(z)$ [5, eq. (24)]. The height h of the web is neglected in the kinematics and w is the local change from R which symbolizes a reference radius. At this reference radius hoop stresses within the web vanish. They are functions of h, the width of the web L, the

[11] The author wants to thank Maximilian Noll for his contributions to this topic.

Young's Modulus E, the tension force in hoop direction T within the web and the average web deflection $u_a = \frac{1}{L}\int_0^L u(z)dz$.
The local gap $g(z) = u(z) - r(z)$ is defined as the distance between web and surface. For boundary conditions using two free ends ([5, eq. (12)]) and at the same time demanding a rigid surface with a complementarity condition between g and p, a finite difference discretization yields a nonlinear complementarity problem

$$Ag - b_c = p, \qquad 0 \le p \perp g \ge 0 \tag{2.38}$$

where the matrix $A(g)$, the vector $b_c(g)$ are functions of the gap.
Remark that the theory assumes symmetry of the underlying surface which is not satisfied for arbitrary element saddle geometries.

Tracking Law The solution of (2.38) is a distribution of radial stress $p(z)$ with

$$p = p(z, T, E, \nu, h) \tag{2.39}$$

where ν is the Poisson ratio of the material.
To calculate the tracking force, an infinitesimally thin slice of the belt with height h, depth b and thickness $\mathrm{d}z$ is considered. The radial stress can be split up in a component $p_n(z)$ normal to the element surface and a component $p_t(z)$ tangential to the element surface with

$$p_n = \cos(\alpha)p \qquad p_t = \sin(\alpha)p \tag{2.40}$$

where $\alpha(z) = \arctan(\frac{dr}{dz})$ is the local angle to the z direction. Integration yields

$$F_n = b\int_{z_l}^{z_u} p_n \,\mathrm{d}z \qquad F_t = b\int_{z_l}^{z_u} p_t \,\mathrm{d}z, \tag{2.41}$$

where F_n is the normal force and F_t the tracking force. The borders z_u and z_l depend on the web position z_0 and the ring width $L = z_u - z_l$.
The dynamic simulation yields a normal force F_n between element and ring that is used as input for the tangential tracking law. The tension T is linked bijectively to F_n in practice for the derived equations and thus can be found iteratively.
Altogether, the tracking force $F_t(F_n, z_0)$ can be found as a nonlinear function of the normal force F_n and the axial position z_0. This function is evaluated offline before integration. It is used as a characteristic field. With this technique more advanced fields due to further developments can be taken into account.

Results and Discussion One tracking field is discussed here to examine the results. The parameters $E = 1.8e^{11}\frac{N}{m^2}, \nu = 0.3 h = 0.185mm, w = 9.75mm$ and $b = 1m$ are used for the ring.[12] A circular surface with

$$r(z) = \sqrt{R_S^2 - z^2}$$

for the element's saddle with a radius of $R_S = 250$mm is considered. The ring position is changed between $z_0 \in [-w, w]$ where $z_0 = 0$ denotes the highest position of the element saddle. The resulting tracking field is shown in Figure 2.13. The tracking force F_t is always directed against the axial position of the ring. Thus, it pushes the ring always to the center, i.e. the highest position of the saddle. The tracking effect increases with higher absolute values z_0 as well as with increasing F_n. It is pointed out, that no tracking effect is active with this law when no normal force is acting which was not the case in prior models [54, 9]. This is physically appropriate and experimentally observed [16].

[12] As b is linear in the law a unit length is used here and is multiplicated with in the simulation

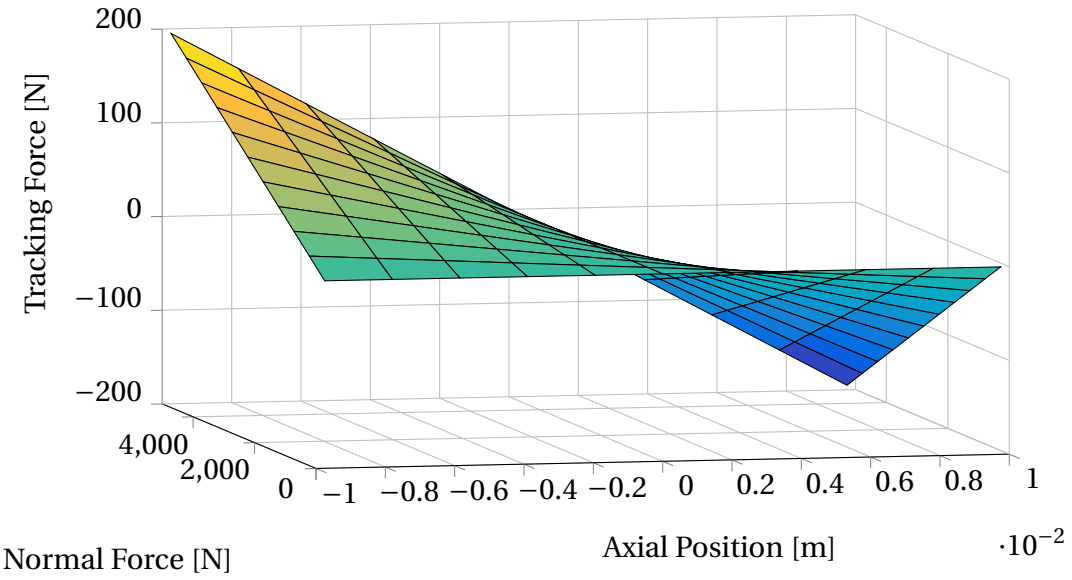

Figure 2.13: Tracking field depending on normal force and axial ring position. Higher normal forces and axial deviation increase the tracking effect.

2.3 Computing Time Reduction

The integration of a fully featured CVT model for one revolution in a stationary point can exceed a week of simulation time on a modern CPU. This simulation time is influenced by many parameters which has been discussed in [54, Section 2.5]. In Subsection 2.1.2 a dedicated ring model is presented. It contributes to the CPU time reduction (Section 3.3). In this section, further drivers of computational costs are identified. Improvements address three points. A kinetic based initialization shortens the transition phase. The coupled force law for the element-pulley contact is enhanced. The influence of contact kinematics on it are discussed, which addresses the physical output as well as the numerics. Finally, the solution for the non-smooth system is optimized. Based on the time-stepping algorithm the special matrix structure could be used to reduce the computational costs.

2.3.1 Initialization

The initialization process approximates a stationary point for given boundary conditions. Errors induce a transition phase in which the system runs into the stationary point. SCHINDLER utilizes basic kinematical correlations and a simplified model of SATTLER to approximate the belt velocities. In [11, p. 5 ff.] the transition phase could be reduced up to 17% for an optimized initialization of the strands in specific cases. This idea is enhanced. Kinetic assumptions, which take into account the forces, help to further shorten the transition phase.

Ring Tension The ring-tension is addressed at first. In [54, p. 47 ff.] the belt velocity along its course is computed using the equations of [51]. The belt force $Z_p (= L_{O_{in}})$ in the strand that runs into the SEC is given in [54, eq. (2.206)]. Assuming that push-forces are transmitted in

the US[13], the belt force gets

$$Z_u = F_{Tu} - F_{Pu} \qquad \Leftrightarrow \qquad F_{Pu} = F_{Tu} - Z_u = F_{Tl} f_e - Z_u$$

with F_{T*} being the tension forces within the rings and F_{P*} the push-forces between the elements (Figure 1.2). The constant $f_e = \exp(\pm\mu_R \varphi_a)$ results from the active arcs φ_a and the friction coefficient μ_R between elements and rings. The third equation for the three unknowns F_{Pu}, F_{Tu}, F_{Tl} is the balance of moments equation on one of the pulleys (Figure 1.2) with

$$-\frac{M_S}{r_S} = \Delta Z \approx Z_u - F_{Tl} \qquad \Leftrightarrow \qquad F_{Tl} \approx Z_u + \frac{M_S}{r_S} \tag{2.42}$$

where M_S is the applied torque at the secondary pulley and r_S as the running radius. The course of the strain $\varepsilon = \frac{F_T}{EA}$ has to be integrated along the rings of length l to gain the mean strain.

$$\bar{\varepsilon} = \frac{1}{l}\int_0^l \varepsilon = \frac{1}{EAl}\int_0^l F_T \tag{2.43}$$

The integral of (2.43) can be divided into the four parts of the belt:

US $\bar{\varepsilon}_u = \frac{1}{EAl_u}\int_{l_u} F_{Tu} = \frac{1}{EAl_u} F_{Tu} l_u = \frac{F_{Tu}}{EA}$

LS $\bar{\varepsilon}_l = \frac{1}{EAl_l}\int_{l_l} F_{Tl} = \frac{F_{Tl}}{EA}$

PRI $\bar{\varepsilon}_P = \frac{1}{EAl_P}\int_{l_P} F_{TP} \approx \frac{1}{EA}\frac{F_{Tl}+F_{Tu}}{2}$

SEC $\bar{\varepsilon}_S = \frac{1}{EAl_S}\int_{l_S} F_{TS} \approx \frac{1}{EA}\frac{F_{Tl}+F_{Tu}}{2}$

Here $\int_l *$ symbolizes the integral over the respective part of the belt. Thus, the mean strain can be calculated with

$$\bar{\varepsilon} = \bar{\varepsilon}_u + \bar{\varepsilon}_l + \bar{\varepsilon}_P + \bar{\varepsilon}_S \approx 2\frac{F_{Tu} + F_{Tl}}{EA} \tag{2.44}$$

and the initial elongation of the ring is approximated with $\varepsilon_0 \approx l\bar{\varepsilon}$.

Flank-Sheave Gap An additional gap g_P between sheaves and elements has been initialized in prior models [54, p.56]. The belt is not constrained by forces between elements and sheaves. This yields contraction of the belt during the first time steps until the contact is closed. The old initialization cannot be used for polynomial sheaves like in Subsection 2.2.2. Therefore g_{P*} is adapted for PRI and SEC individually. The contact kinematics implemented in the system is used directly to initialize the element positions. An initialization, which is independent from the individual contours, is enabled.

Following [6, p. 41], the TR $i_F = \frac{F_P}{F_S} \approx \frac{\varphi_P}{\varphi_S}$ can be approximated for the torque free situation with the arc ratio. The mean gap $\bar{g}_*$ for one sheave is assumed using a force equilibrium between the respective clamping force F_* and the sum of all deformation forces acting within the elements N_* in the respective arc. The formula of a linear spring with the stiffness c_{ax} is used to relate both.

$$\bar{g}_* \approx \frac{F_*}{N_* c_{ax}} \tag{2.45}$$

The ratio between the arc length $l_* \approx r_* \varphi_*$ and the complete belt length l yields $N_* \approx \frac{l_*}{l} N_E$ and thus the mean gaps can be calculated for the two arcs.

[13] which is the default case

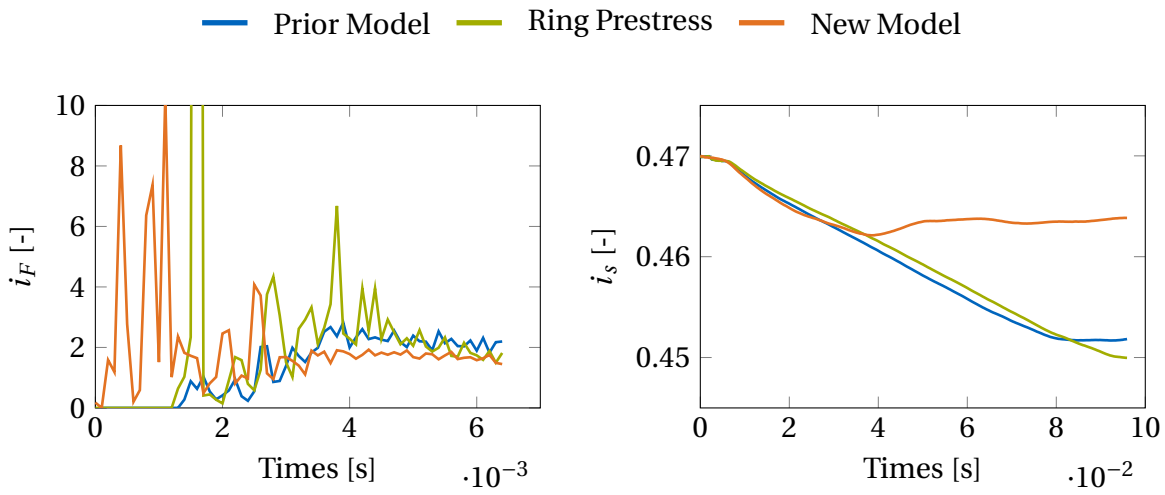

Figure 2.14: Comparison of initialization for overdrive

Primary $\bar{g}_{PP} = \frac{F_S \varphi_P l}{c_{ax} r_P \varphi_S^2 N_E}$

Secondary $\bar{g}_{PS} = \frac{F_S l}{c_{ax} r_S \varphi_S N_E}$

Figure 2.14 shows exemplary results of three models in the same OD configuration. The "Prior Model" of [9] is used as a reference. An intermediate model, i.e. "Ring Prestress", only initializes prestressed rings but the distances to the sheaves are still positive. The "New Model" uses all presented ideas.
The TR stays zero at the beginning of the simulation for the first two models. No contact is active at the SEC. The new model has contact at the beginning and thus the transition phase is reduced about 50%.
It can be seen that due to the combined initialization also the speed ratio converges earlier. This mainly results from the fact that forces are applied on the element-flanks at the beginning. The torque equilibrium is reached earlier and with it a stationary point. Long transition times can be avoided to gain global values. The presented ideas are therefore mainly of interested when gaining only global values.

2.3.2 Coupled Contact

Many contributions prove the representation of the pulley deformation as essential for the precise modeling of the CVT dynamics [13, 51, 69, 6, 25]. Equation (2.34) is used to represent this deformation successfully [9]. Yet, the solution of the system gets more delicate compared to a decoupled contact law. Generally a pivoting scheme, i.e. the Lemke algorithm [52, Chapter 2], or an iterative scheme, i.e. a Newton algorithm, are applied.
This section addresses improvement strategies by analysis of the formulation of the interaction model. Therefore, the solution strategies are compared at first.

Solution Schemes

A representative use case has been chosen to compare the solution schemes. In a planar OD configuration ($i_s \approx 0.4$) with $N_E = 160$ about 8000 LCPs have been solved. One fixed contact

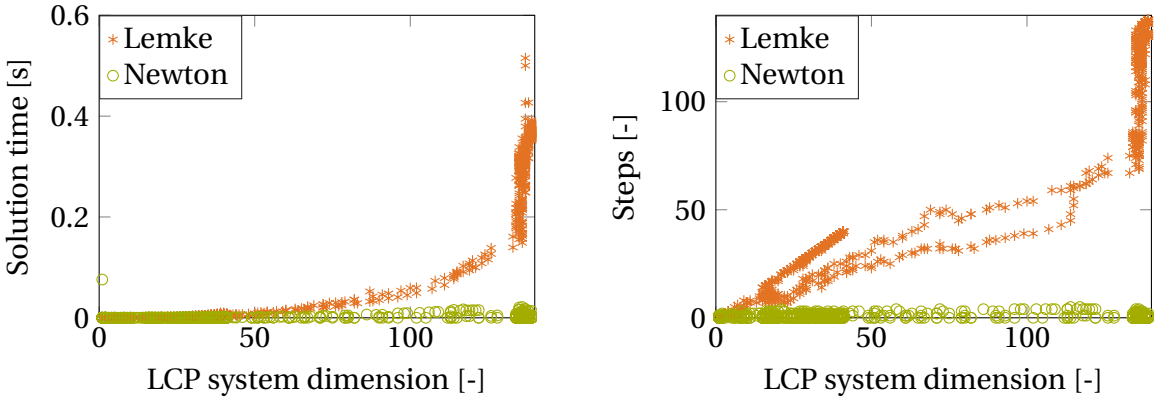

(a) Time consumption for solution of the coupled contact law.

(b) Pivoting steps for the Lemke algorithm or iteration steps for the Newton solver over the system dimension.

Figure 2.15: CPU costs compared for the Lemke algorithm to the Newton iteration if applied to a practical example with a fixed contact point on one flank.

point on each flank is chosen. Solution times for the two schemes are given in Figure 2.15a. For small dimensions n both schemes are comparable. The number of pivoting steps increases with $\mathcal{O}(n^3)$ in the practical examples of the CVT. Thus, the Lemke algorithm needs more simulation time.
The iterative scheme keeps low simulation times even for high dimensions. The iteration can be started with the previous solution of the last time step. In this case it is close to the new solution and the number of iterations stays low. For the application in the presented case, the number of iterations steps is between 0 and 5.

Interaction Model

Different contact kinematics exist to find the contact point on the element-flanks and the pulley-sheaves. Two circular rings interact with the sheave in the model of [54] yielding two contact points at the front and the rear of the flank. In combination with the coupled contact law introduced in [9] this modeling yields numerical problems as well as questionable behavior which is addressed in the following. Two extreme situations are discussed. Either the full flank deformation is coupled, i.e. front and rear deform the same amount. Or the deformation is decoupled completely.

Coupled Flank Deformation Based on the assumption that the element deforms along the whole axial direction and keeping in mind that the element is very thin, a coupling of the whole flank deformation was tested as a natural approach.
Practically, the contact force switches in an oscillating manner between the front and the rear of the flank (Figure 2.16a). No smooth change is apparent. On the one hand this is unphysical. It leads to induced oscillations such that the simulation cannot be finished. On the other hand numerical problems arise. The force changes rapidly at a certain position[14] such that the old solution is not close the new one. An iterative solution scheme needs many iterations as the start value from the old solution is generally useless. It results in higher computational costs – for a robust integration only the Lemke algorithm can be used which results in much

[14] See for example at $t \approx 5.3s$ in Figure 2.16a

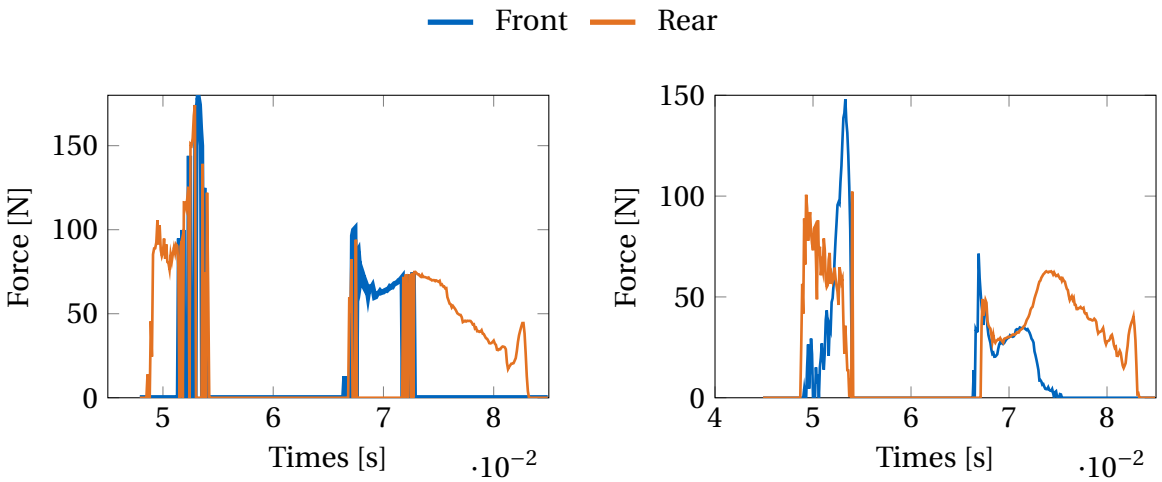

(a) Coupled flank deformation

(b) Decoupled flank deformation

Figure 2.16: Normal forces on the front and rear contact points on the right flank of one exemplary element along the belt in an OD configuration.

higher simulation times. It takes approximately 6.4 times longer[15] to simulate a full CVT model compared to a model with a fixed contact point on the flank.

De-Coupled Flank Deformation Figure 2.16b shows results of a simulation where the front and rear deformation of the flank are decoupled. One can see that the strong oscillations between front and rear vanish compared to a coupled flank deformation – an iterative scheme can be applied. Yet, the contact force is not distributed along the flank, see e.g. $t \approx [7.5s, 8.3s]$ in Figure 2.16b. The force is only acting at the rear of the element. Also, still a full CVT simulation takes ≈ 2.9 times longer[15] compared to a case with a fixed contact point on the flank. The system dimension is doubled and the contact kinematics gets more complex.

Altogether, two contact points on the flank result in much higher simulation times combined with numerical problems as well as physical inaccuracies. Therefore, only one contact point is used in this work.
For planar cases one fixed contact point on the flank may be used as no yawing motion is enabled. Subsection 2.2.2 introduces a spherical model for the element-flank resulting also in only one contact point which suits the needs for spatial simulations. Consider the situation where the element runs into the pulley arc and is yawed wrt. the pulley radial direction as well as rolled wrt. to the azimuthal pulley direction, e.g. driven by misalignment of the pulleys. In this case the contact kinematics is able to find a contact point along the whole flank in contrast to a fixed point on the flank. Thus, the spherical contact point is preferred for spatial simulations taking into account these considerations.

2.3.3 Mass-Action Matrix

This section addresses the numerical optimization for a non-smooth model integrated by a time-stepping algorithm. The mass-action matrix (1.11) has to be computed.[16]

[15] The average of three simulations in OD, MED and US are used as basis

[16] The author wants to thank the student worker Zhan Wang for his valuable contribution in this topic.

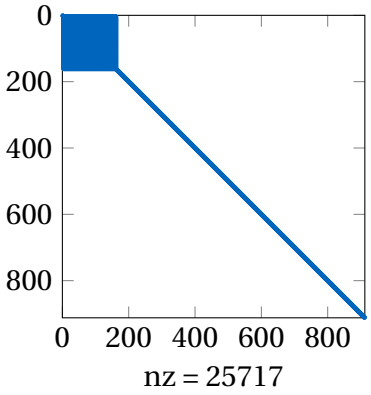

(a) Decomposed Matrix M

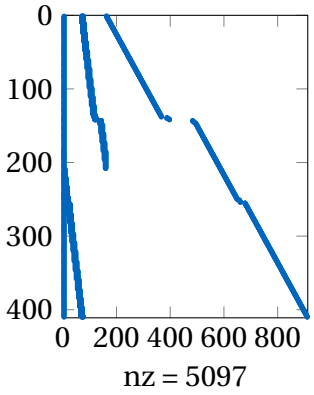

(b) Transposed direction Matrix W

Figure 2.17: Sparsity patterns of the matrices, that are necessary to solve for the impacts in one time step. The value nz is the number of non-zero values which are depicted blue. The zero values in the matrix are white.

As the mass matrix M is a real-valued, symmetric and positive-definite matrix, the Cholesky decomposition yields

$$M = LL^T \tag{2.46}$$

where L is a lower triangular matrix with real and positive diagonal entries. Inserting (2.46) in (1.11) yields

$$G = W^T M^{-1} W = W^T \left(LL^T\right)^{-1} W = \left(L^{-1}W\right)^T \left(L^{-1}W\right) = y^T y \tag{2.47}$$

where

$$y = L^{-1}W \, . \tag{2.48}$$

The calculation of G can be performed in two steps:

1. Solve the triangular system $Ly = W$ represented by (2.48)
2. Multiply y with its transpose to get G as given in (2.47)

In the following these matrices are analyzed for the present model. The used integrator, i.e. a time-stepping scheme, together with the sparse structure of the matrices yield a CPU time reduction in practice.

The pushbelt consists of about 200-400 kinematically decoupled rigid bodies, i.e. the elements, with three[17] or six[18] DOFs. One[17] or two[18] rings, each of about 200 DOFs[19], guide these elements. The two pulleys have one or two DOFs each. They are of minor significance for the following considerations.
The sparsity patterns of a planar simulation with a non-smooth element-ring contact are given in Figure 2.17. Figure 2.17a shows the pattern of the decomposed mass matrix. The upper left corner is dense. It belongs to the ring. For it the decomposition has to be done

[17] for the planar simulation
[18] for the spatial simulation
[19] in case their deformation is considered dynamically

every time step. It is of order $\mathcal{O}(n_r^2)$, where $n_r \approx 200$. The lower right part is the one from the elements. It is constant in time. Thus, the decomposition is of minor importance to the overall CPU time.
Figure 2.17b shows the pattern of the projection matrix W. It is clear that this matrix is sparse as only elements are connected to some DOFs of the rings. No non-smooth interconnection between the elements exists.
Algorithms for sparse matrices[20] are therefore applied to solve (2.48) as it reduces the complexity from $\mathcal{O}(n_{DEN}^2)$ to $\mathcal{O}(n_{z,L} + n_{DEN})$ where n_{DEN} is the dimension of L and $n_{z,L}$ the number of non-zero values in L [12].
As G is symmetric, the full multiplication in (2.47) does not consider the sparsity of y. This avoids long memory access times internally and yields faster computation in practice. It is remarked that for the described non-smooth case about 17% of the whole computational cost result from unnecessary memory access in the G-matrix. Nine simulations[21] have been performed to measure the overall gain for simulation time either with or without the described algorithm. Taking the quotient of the simulation times without the algorithm (t_{wo}^i) or with it (t_w^i) yields an average factor $f^i = \frac{t_{wo}^i}{t_w^i}$ of $f = \frac{1}{9}\sum_{i=1}^{9} f^i \approx 1.7$.

2.4 Post-Processing

In the post-processing interpretable values from the simulation results are calculated. This section describes the single steps. Two levels are separated. The model basically yields local results like contact forces or positions of the elements. Differences between the single outputs of the elements exist. To identify real trends from numerical oscillations the curves are averaged. The common structure of the plots along the arc is explained as well.
Global results classify the state of the system. They are a direct result from the local values. The steps to gain these significant numbers of a simulation are given finally.

For all simulations in this work the boundary conditions are used as described in [54]. They are set by the following values (Figure 1.2).

Primary Speed ω_P The speed of the primary pulley is kinematically prescribed.

Primary Sheave Distance z The distance between the primary sheaves is initially defined by the geometric ratio $i_{g,NP}$, i.e. the ratio of the ring's center lines radii. In case of stationary simulation the axial position is constant. It approximates the speed ratio with $i_S \approx i_{g,NP}$.

Secondary Torque M_S In practice the primary torque M_P is applied. The speed ratio is controlled by a primary clamping force F_P. As this control approach leads to higher computational times, at the secondary pulley a torque is applied. Mostly direct measurement values can be used.

Secondary Clamping Force F_S The values are typically part of the boundary condition definition and can be used directly.

In practice a certain safety S is set for the measurements relating the maximum torque that can be transmitted at a pulley to the applied torque. For both pulleys a safety value is defined

[20] using the `csparse`-library [14]
[21] three different ratios and three different applied torques

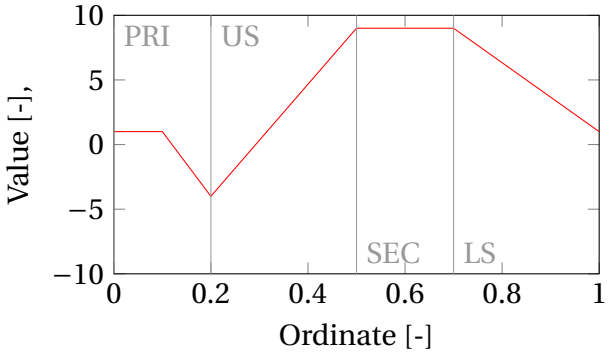

Figure 2.18: Typical structure of the plots

and the final safety S is found by using the smaller of the two values. It is approximated following [46] by

$$S_P = 2\frac{\mu r_{P*} F_P}{M_P \cos\beta} \qquad S_S = -2\frac{\mu r_{S*} F_S}{M_S \cos\beta} \quad \Rightarrow \quad S = \min(S_P, S_S) \tag{2.49}$$

where μ is the friction coefficient, $r_{P*/S*}$ are the running radii at the PRI or the SEC and β the half wedge angle of the pulley-sheaves.[22] From this and together with $i_F \approx 1$ the clamping forces and torques at the SEC can be approximated if no measurement values exist.

2.4.1 Local Results

Structure of the Plots

For the plots of local values, i.e. plots along the belt, typically two versions are given in the thesis. Either it is plotted along the arc of one of the pulley using the local angle in degrees. Or it is plotted along the complete belt using time data, i.e. "Times [s]", as ordinate. It is then scaled to start at $0s$ and ends after one revolution. The structure is sketched in Figure 2.18. It follows the element along the belt starting in the PRI. The positions are marked with a vertical line and the respective acronym if it contributes to the explanation in the text. A full example is given in Figure 2.19.

Space Averaging Element

The model consists of a large number of DOFs. It shows both numerical and physical oscillations. A common approach in measurement is to use average outputs of a certain number of measurements to identify trends more clearly.
In a quasi-stationary point[23] oscillations of different kind[24] influence the output of the local measurements like contact forces. Figure 2.19 shows this effect for normal forces between the elements in the simulation. Along the arc "Element 1", "Element 23" and "Element 45" are given where $N_E = 220$. The curves show different oscillations. A lower frequency is seen in the US, i.e. the push-strand. A high frequency oscillation is in the LS, i.e. the loose-strand. Besides

[22] Only positive values for S_P and S_S are taken into account.
[23] where e.g. thrust ratio and efficiency stay constant
[24] e.g. overall oscillations of the strands

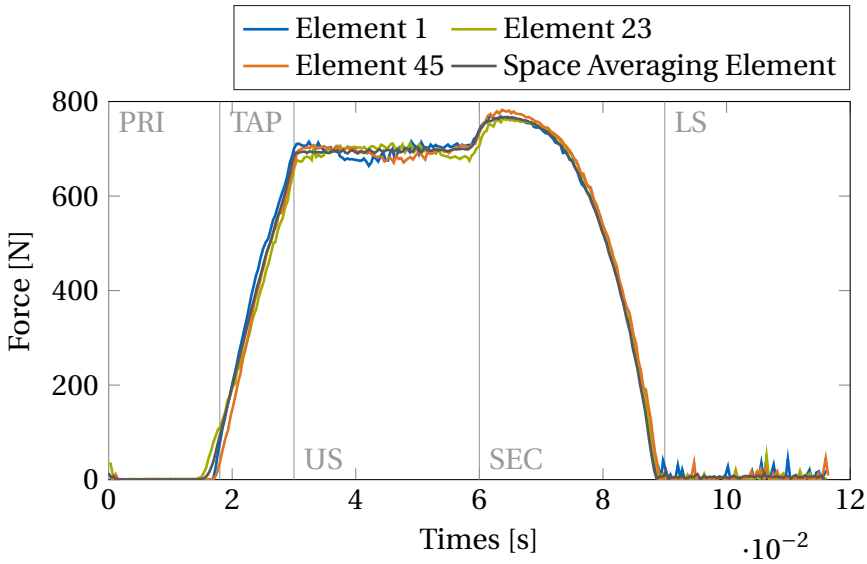

Figure 2.19: Comparison between element-element forces of different simulated elements and an averaged output curve.

the output of the "Space Averaging Element" is plotted. Both oscillations vanish leading to a constant force in the push-strand as expected from theory. Furthermore, the short impacts in the loose-strand are avoided.

To average over the output of the plotted elements the following steps are executed.

1. At first the time t_{st} of a stationary point is identified. Therefore, the oscillations of global values, i.e. i_F and i_s, are analyzed. Their oscillations have to be less then a certain tolerance for a certain number of time steps. Both values, i.e. the tolerance and the number of time steps, have been identified by experience. Only values after t_{st} are taken into account.

2. Due to the contact to the sheaves the transition time points of the elements are found. In case an element passes one of the parts more than once after t_{st} only the values of the last part are taken into account. Then the last turnaround time of the whole belt is identified with t_{lt}.

3. For all elements that are used for the averaging process, a virtual time span for every part is identified, which is the mean time of the respective part.

4. Then a linear interpolation yields the values for every local curve at the time points of the virtual times. For the final value the mean value at this time point is used. This is the value of the "Space Averaging Element".

With the described averaging process it is possible to visualize trends more clearly, e.g. the constant normal force between the elements. One has to keep in mind that also physical effects that are active within the system might not be given in the output curve. In this work it is referred to these situations in case the space averaging also removes other than the numerical oscillations which contribute to the discussion. Convergence tests on global output values, e.g. efficiency, showed that a number of 10 elements lead to sufficient results. Thus, this number of elements is chosen to compute the final output curves shown in the following chapters.

Local Measures

Due to the very detailed modeling, it is possible to generate a variety of different quantities. For the analysis, this work focuses on the most crucial quantities which are listed in the following. In Subsection 2.2.1 it is remarked that the forces on the elements in the simulations differ from the forces within the measurements due to the different thickness. This is regarded in the post-processing such that the force curves show the forces of the real rather than a simulated element.

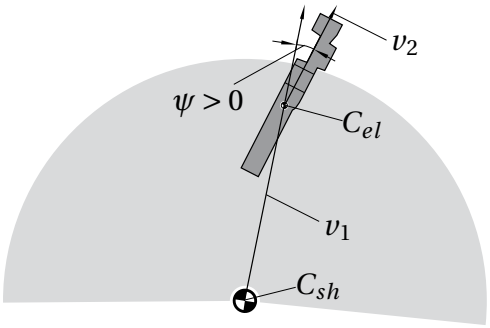

Figure 2.20: Sketch for positive element-sheave pitch angle

Axial force Forces projected in the local axial direction of the element.

Element-sheave pitch ψ This quantity measures the relative pitch angle between the element and its local position in the respective arc (Figure 2.20). The vector from the respective arc center C_{sh} and the center of gravity (COG) of the element C_{el} is called v_1. The local axial direction is v_2. The element-sheave pitch is then defined as

$$\psi = \arccos(v_2 \cdot y_I) - \arccos(v_1 \cdot y_I) \tag{2.50}$$

Thus, it is positive for an element that "leans" forward, i.e. the head is more to the front than the bottom of the element.

Longitudinal force Forces projected in the local longitudinal direction.

Normal force This is the normal force for different contacts. In case of the element-element contact it is the sum of the forces at the head and the RE if not further specified.

Radial force All forces projected in the local radial direction.

Spiral running To gain spiral running the upper surface of the rings is measured in test rigs. Within the simulation the COG of the elements are taken, which yields a different radius. To compare both, the medium radius integrated over the arc is used as reference. The measure for spiral running is the deviation from this radius along the arc.

The positive directions follow [35, Fig. 1] which is again depicted and listed in Figure 2.21.

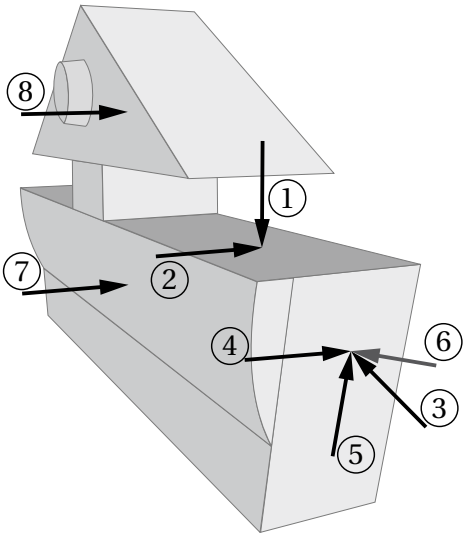

1. The normal force between element and ring
2. The longitudinal friction force between element and ring
3. The normal force at the element-flank
4. The friction force part at the element-flank in longitudinal direction
5. The friction force part at the element-flank in radial direction
6. The axial force in the element resulting from projection of 3 and 5
7. The normal force between the elements at the RE
8. The normal force between the elements at the head

Figure 2.21: Forces with positive direction following [35, Fig. 1].

2.4.2 Global Results

Global values are based on local results and are used to specify different cases. The following measures are used within the work:

Speed ratio i_s It is the average of the fraction of the two angular velocities after t_{lt}[25] as defined in (1.1).

Thrust ratio i_F It is the average of the fraction of the sum of all forces acting on the respective pulley-sheaves in global z_I-direction after t_{lt}[25] as defined in (1.2).

Torque ratio r The torque ratio $r = \frac{M_S}{M_S^*}$ is defined to be the ratio between the actual applied torque M_S and the maximum transmittable torque M_S^*.

Efficiency Different loss mechanisms act during the simulation. To compute the losses the local values of the space averaging element are used as basis. Frictional power-loss is the product of friction force and tangential relative velocity. These are integrated along the belt and divided by t_{lt} to gain the average power loss P_*. Remark the integral is calculated for every contact position (element-element, element-sheave, element-ring) and for every section (PRI, US, SEC, LS) of the belt. Thus, the different sections can be analyzed in detail concerning their influence on the losses. The sum of all losses is divided by the input power P_{PR} that is acting at the primary arc. The difference to 100% yields the local efficiency η_{loc}.

$$\eta_{loc} = 1 - \frac{\sum_* P_*}{P_{PR}} \tag{2.51}$$

All other losses that are acting within the modeled system, e.g. numerical based losses coming from the integration method, cannot be covered. Further losses are active within the whole drivetrain that are affected by the mechanics of the pushbelt CVT, e.g. the losses of the bearings or hydraulic losses that depend mainly on the clamping forces. For these losses post-processing models exist which are provided by BTT. If these values

[25] In case no t_{lt} exists the time after t_{st} is used

are taken into account the efficiency is denoted by η_{glob}.
This work is dedicated to the direct mechanical losses that can be observed from the simulation model. These are analyzed in more detail. The main loss mechanisms within the system are based on friction [2, 3, 4] and are given with their respective abbreviation:

ElPuLoPRI The longitudinal losses for the contact between element and pulley in the PRI.

ElPuLoSEC The longitudinal losses for the contact between element and pulley in the SEC.

ElPuRaPRI The radial losses for the contact between element and pulley in the PRI.

ElPuRaSEC The radial losses for the contact between element and pulley in the SEC.

ElRiLoPRI The longitudinal losses for the contact between element and rings in the PRI.

ElRiLoSEC The longitudinal losses for the contact between element and rings in the SEC.

Endplay The endplay is a general measure to quantify the distance between the elements within the belt. For this work it is defined as the quantity which sums up penetrations and positive distances of the contact gaps of the element-element-contacts. It is therefore a measure for the setup of the belt and does not depend (strongly) on the operation condition. Within the model the endplay can be computed at the RE and the head. The final scalar value results from an average after t_{lt}[25].

Operational endplay v The OEP depends, in contrast to the endplay, on the operating conditions. It sums up only the positive contact gaps and thus measures – depending on a certain belt structure – the changes due to boundary conditions, i.e. loads and speed ratio. The OEP can be measured either at the RE or the head. Due to the arcs mechanics the OEP at the RE is the crucial measure and is denoted as v in the following. The final scalar value results from an average after t_{lt}[25].

The difference $\Delta v_g = v_g^i - v_g^{ref}$ between a global value v_g^i and a reference value v_g^{ref} is used to compare simulation results with different parametric settings[26] in this work. The reference value is either taken by one specific reference parameter setting which is then specified or it is the average value of all parametric cases with the same boundary conditions.

[26] marked by the index i

3 Numerical Aspects

Following the process of Figure 1.5, the models are tested in parametric studies. The quality of the model is analyzed and the sensitivity on the crucial parameters is identified. The numerical aspects are addressed in this chapter.

The influence of the number of elements in the simulations is analyzed in Section 3.1. A minimal number for the simulations is found. It sets the bounds on the accuracy of the model on the global values.
The difference between a smooth and a non-smooth simulation model is compared next. The stiffness between elements and rings is changed as well as their friction description. Besides, the friction between element-flanks and sheaves is analyzed, which yields conclusions on the non-smooth modeling for the system in Section 3.2.
In Section 3.3 different ring models are compared wrt. local and global effects. It is shown, that a specific modeling for the CVT dynamics improves the results. A glance at the spatial outputs shows possibilities for future projects. A compromise between accuracy and computational cost has to be chosen for efficient simulation.

To draw general conclusions about the parametric influence, the boundary conditions are varied as well. The settings are taken from measurements to ensure realistic settings. Three different loads are applied at three different ratios. In experiments the transmitted primary torque $M_P^1 = 30\text{Nm}$, $M_P^2 = 50\text{Nm}$ and $M_P^3 = 100\text{Nm}$ is varied. The values for M_S^* and F_S^* result from measurements of a reference belt. The measurements were conducted by BTT. All simulations run with the same ω_P, i.e. 2000 revolutions per minute(RPM), as the belt speed has a minor influence on the behavior. Altogether, the nine basis cases (BCs) are given in Table 3.1.
The analysis follows the idea to present the global influence on the system behavior at first. Mainly the thrust ratio i_F and the local efficiency η_{loc} are given as the most important global measures. A local analysis follows explaining the main findings. Local and global output curves and values are utilized as examples.

	BC01	BC02	BC03	BC04	BC05	BC06	BC07	BC08	BC09
$i_s[-]$	0.47	1.00	2.42	0.47	1.00	2.42	0.47	1.00	1.30
M_P[Nm]	30	30	30	50	50	50	100	100	100

Table 3.1: Boundary conditions used for the parameter variations. All cases use $\omega_P = 2000$ RPM and a safety value of $S \approx 1.3$.

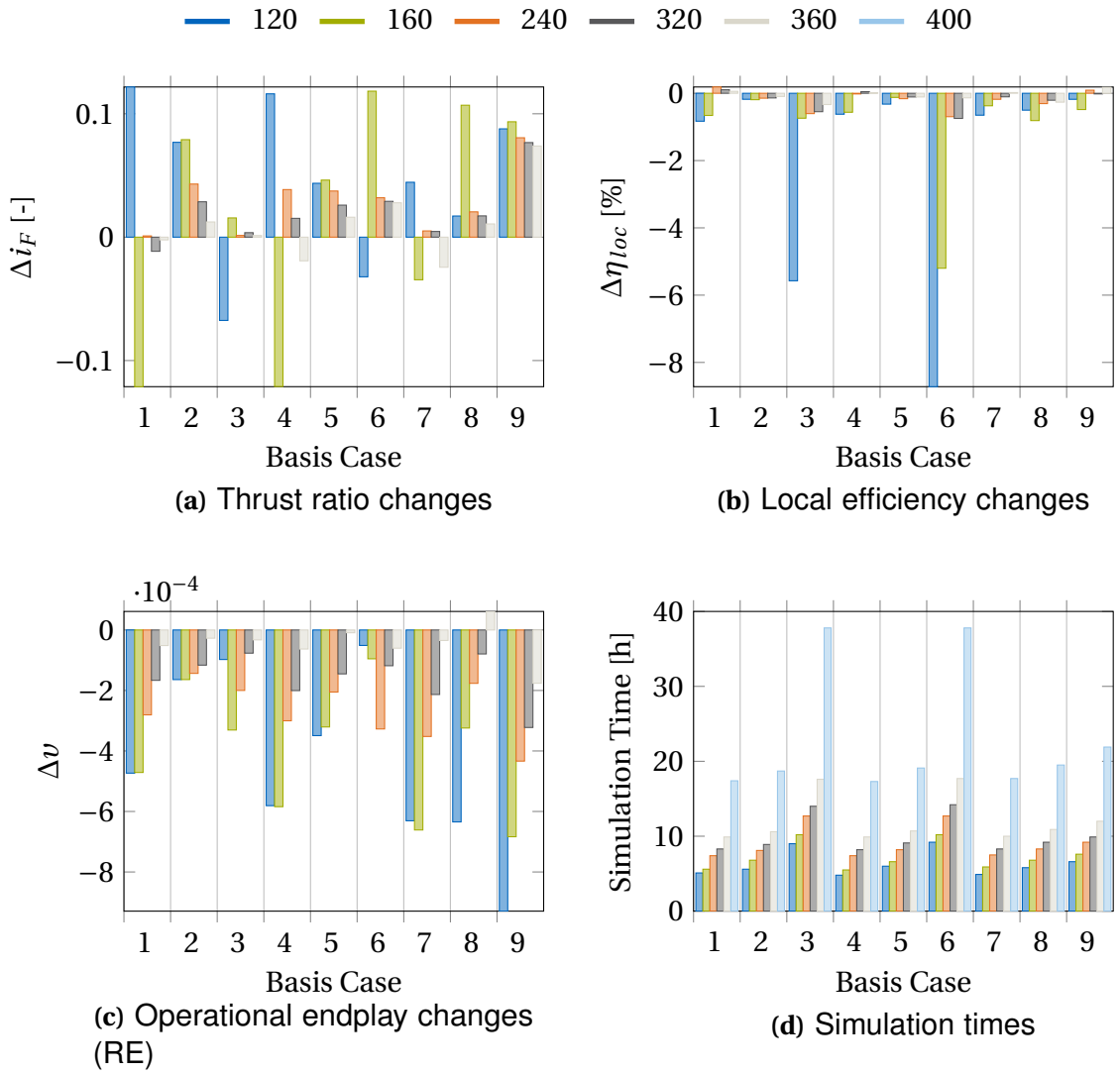

(a) Thrust ratio changes

(b) Local efficiency changes

(c) Operational endplay changes (RE)

(d) Simulation times

Figure 3.1: Simulation results varying the simulated elements N_E for the cases of Table 3.1. The simulation with $N_E = 400$ is used as reference.

3.1 Simulation Elements

To enable precise yet fast simulations, a feature of the model is to choose the number of simulated elements. In Subsection 2.2.1 it is discussed which adaptions are made such that the simulations get comparable. Even though it is possible to reduce the number of elements within the simulation concerning the force laws as well as inertia effects, the geometry cannot easily be adapted consequently. Similar effects can be seen in the Push-Force-Tester in Subsection 2.2.3. The length of the pin as well as the radius in the RE are two examples. This section analyzes the effects due to changes in N_E.
For the comparison, N_E has been increased starting with 120 elements and ending with 400 elements. The results are given in Figure 3.1. The values of i_F, η_{loc} and v are compared to the reference simulation with 400 elements yielding Δi_F, $\Delta \eta_{loc}$ and Δv.

Large changes within the prediction of i_F and η_{loc} can be seen for the cases with small N_E, i.e. 120 and 160 elements (Figures 3.1a and 3.1b). It is also not a monotonous trend for i_F but the values vary around the reference. The error reduces with increasing N_E.

The efficiency η_{loc} however increases with N_E monotonously disregarding minor numerical based exceptions. As never $N_E = 400$ is chosen in this thesis, it can be concluded, that the values for η_{loc}, which are presented in this work, are too high.
Besides the global values, the output of the local values changes. Generally a smoother output can be observed in the local curves by increasing N_E (also [9, section 7.3]). This is a major contribution to higher values of η_{loc}. The oscillations around zero get less yielding reduced numerical errors in the post-processing step.

To analyze the change of the model the OEP is given as well. With increasing N_E it reduces (Figure 3.1c). This results from the change in geometry of the elements. They align closer within the arcs reducing the distance. This increases v. The operational endplay at the head however is not affected.
To cover for this effect a correction is suggested. It is reasonable to treat the simulations with less than 200 elements as exceptions – the solution of the coupled contact law for the sheaves is not precise as only a few contact points are taken into account. Also the geometry is changed compared to the reference of 400 elements. A linear regression yields an operational endplay gain of about $v_{corr} = 2 \cdot 10^{-6} \frac{\text{m}}{\text{element}}$. A correction of the ratio ι of (2.27) is given.

$$\iota_{corr} = (\iota - v_{corr}(\iota - 1)) \tag{3.1}$$

Simulations were carried with this correction. The corrected simulations have a standard deviation σ of only 0.07 for i_F compared to a standard deviation for all cases of 0.19 without the correction. The standard deviations of η_{loc} (0.3% without vs. 0.28% with correction) and v ($1.6 \cdot 10^{-4}$m without vs. $2.8 \cdot 10^{-4}$m with correction) yield similar values in both cases. The correction shows the improvement potential in further adaptions in the model. The number of simulations should be increased for this to identify also nonlinear effects due to this adaption.

The correct representation is an important measure, yet the costs increase with N_E, i.e. the simulation time. These are given in Figure 3.1d. A linear increase of the simulation time can be seen with N_E.
As the elements get more in number they also become thinner. Following Subsection 2.2.1 it is clear that the contact stiffness increases for the element-element contact. Therefore, the overall model gets stiffer. Smaller time steps in the integration are needed as soon as this contact dominates the stiffness within the whole MBS. It was necessary to simulate the model of 400 elements with half the time step size for a robust integration explaining the big step for the last simulation.

It is concluded, that a number of less than 200 elements for the simulation should not be chosen for the discussed reasons. Adapting the thickness of the elements following (2.27) improve the results for a low number of elements. A number of about $N_E = 250$ is chosen as a compromise between accuracy and CPU costs avoiding too high stiffness.
The discussion above shows also the maximum of accuracy of the model. The standard deviations are about $0.05 - 0.1$ for i_F and 0.3% for the η_{loc}.

3.2 Non-Smooth Simulation

The elements and sheaves are modeled as rigid bodies to minimize the number of DOFs. Yet, their deformation plays an important role for the overall mechanics of the system. The sheave deformation is crucial for correct spiral running. The deformation of the elements change

the operational endplay which is an important measure for the longitudinal losses within the system. The element-element and the element-sheave contacts are therefore single valued in normal direction.
It stays unclear how to treat the element-ring contact as the rings are deformable. Besides, the friction may either be regularized or not. This section treats outcomes resulting from different models for the discussed contact description.
Eight cases are separated which are given in Table 3.2. Either the contact-law is set-valued, i.e. non-smooth (NS), or single-valued, i.e. regularized (Reg), at the element-saddle (Sa) or the element-flank (Fl) in normal (n) or tangential (t) direction. For the normal direction at the saddle different stiffness values c_{ElRi} are tested as well.

	Names							
	1e6	1e7	1e8	NSSa	NSRi	NSFl	NSFri	NSALL
Sa_n	1e6	1e7	1e8	1e7	NS	1e7	1e7	NS
Sa_t	Reg	Reg	Reg	NS	NS	Reg	NS	NS
Fl_t	Reg	Reg	Reg	Reg	Reg	NS	NS	NS

Table 3.2: Different cases used for comparison of the non-smooth simulations

For the cases the variants of Table 3.1 are compared. The influence on the dynamics is discussed at first when non-smooth force laws are used for the element-ring contact. Then the influence due to non-smooth friction at the flanks is considered. The CPU costs are analyzed for all simulations such that conclusions can be drawn.

3.2.1 Element-Ring Contact

The contact between elements and rings can be either modeled non-smooth or regularized. The physics are of minor importance compared to the numerical influence. Concerning the CPU costs, the regularization of the contact laws is favorable. Yet, a parameter is introduced that should be chosen correctly. For the cases in Table 3.1 stiffness values c_{ElRi} between $1e4$ and $1e10$ have been varied. Values outside of $c_{ElRi} \in [1e6, 1e8]$ did not yield robust integration. The results are compared to the simulation, which use non-smooth contact laws at the saddle. As reference NSRi is used.

One can see from Figure 3.2 that too low stiffness, i.e. $1e6$, changes the output behavior. The normal penetration gets very large[1] (Figure 3.2c). For higher stiffness this reduces one order of magnitude, which yields a more reasonable results.
With a rigid contact in normal direction the penetration is not zero. The compatibility condition is solved for the relative velocity in the contact. The contact law in (1.6) ensures that the normal relative velocity gets only zero up to a certain tolerance, i.e. $\dot{g} \approx 0$. Small errors in this computation can lead to a penetration on position level, i.e. $g \neq 0$. A so called drift effect, i.e. the contact penetration increases during contact phase and leads also to high penetration values. In OD the compression is very large due to the high F_P. Then, even in the push strands a penetration between saddle and ring is active. This is directly correlated to the large differences in i_F compared to the other cases when a penalizing algorithm is used (Figure 3.2a). A projection of the generalized coordinates for the contact penetration to set this penetration to zero could not be performed robustly for the system. Thus, a deeper

[1] up to 0.15mm

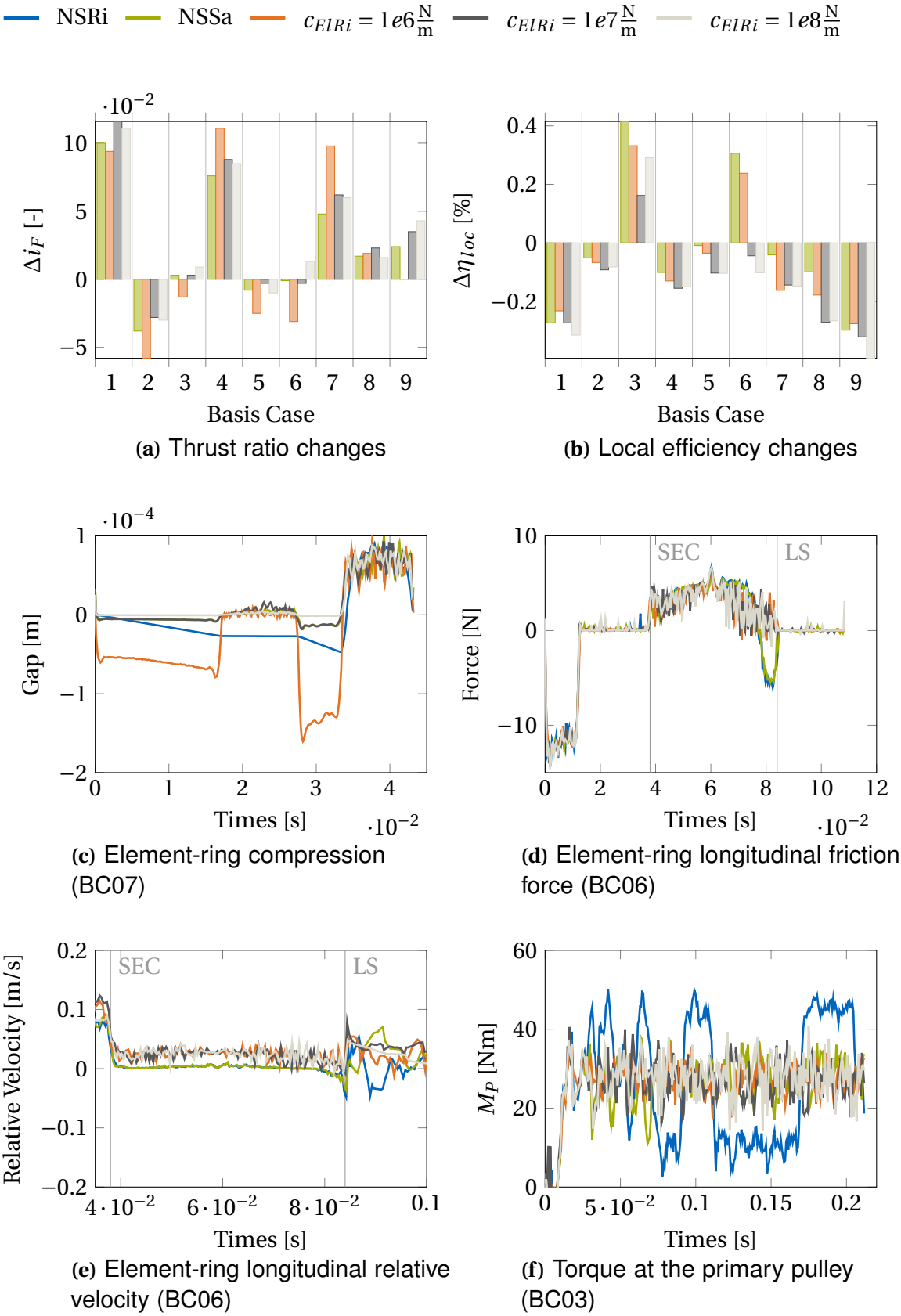

(a) Thrust ratio changes

(b) Local efficiency changes

(c) Element-ring compression (BC07)

(d) Element-ring longitudinal friction force (BC06)

(e) Element-ring longitudinal relative velocity (BC06)

(f) Torque at the primary pulley (BC03)

Figure 3.2: Varying element-ring contact laws. The contact laws and/or stiffness of the element-ring contact is changed. As reference the output of NSRi is used for global values.

analysis is not possible for this phenomenon. For the other cases i_F varies due to minor numerical differences.

The simulations suffer less from oscillations when using non-smooth contact laws. Due to the more precise estimation of the forces, also the direction may change (Figure 3.2d at the end of the SEC). This peak is known from measurements (e.g. Figure C.3). The effect however is clearly related to the non-smooth calculation of the frictional forces. Sticking is represented correctly (SEC in Figure 3.2e). In comparison the regularized contacts oscillate around a relative velocity of zero and yield higher losses.
Taking into account besides the tangential also the normal direction in the non-smooth force law reduces the oscillations and improves the efficiency calculations. However, in UD no stationary point is found which can be seen in Figure 3.2f. The torque at the primary switches between two states, i.e. $M_P \approx 10$Nm and $M_P \approx 45$Nm where the other models suggest a stationary torque of about 30Nm. A stationary situation is not reached which does not allow for e.g. a correct power estimation (BC03 and BC06 in Figure 3.2b).

3.2.2 Flank Contact

The contact at the flank of the element is a crucial part in the system and should be as precise as possible. Here the torque is introduced into the system and thus the frictional forces have to be computed correctly. Non-smooth friction laws can represent sticking correctly which is not the case for standard smooth contact laws. It has proven successful in the case for the element-ring contact. Yet, for the flank contact no sticking is expected. Due to the effect of spiral running the contact slides almost everywhere.[2] However, in the following the results are analyzed resulting from non-smooth friction at the flank.
Introducing non-smooth friction at the flank leads to non-robust solutions of (1.12). The number of the average iterations in one time step for the fixed-point solver increases from about 30 to 2030 for the example of BC01. For many time steps no solution is found that fulfills the tolerance. The integration proceeds after a maximum of 10000 steps. Practically, this leads to increased simulation times.
As a contact force acts at the left and the right flank and the element is modeled as rigid body, two forces project into the same generalized direction. It is therefore not unique how to choose these. Additional impact laws using more conditions to find a unique force could be introduced. The iteration steps could be reduced and a solution might be found within the tolerances. This is subject of current research [41].

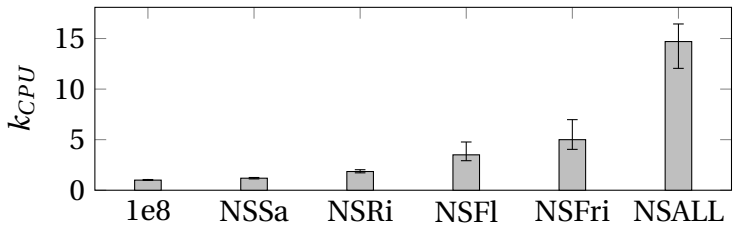

Figure 3.3: CPU costs for different non-smooth simulations. As reference the smooth simulations are used (Table 3.2).

For the results in Figure 3.3 the case "1e8" (Table 3.2) is used as reference.[3] The average

[2] sticking could happen at the TAP
[3] The three smooth simulations are performed in the same simulation times.

factor k_{CPU} is the average fraction between of the simulation time of one case to the reference simulation time. The additional error bars denote the maximum and minimum deviation which results from the simulation of the cases defined by Table 3.1. For the reference case the other smooth simulations are used to compute the deviations.
Constraining the system with a set-valued force law yields longer simulation times as discussed in Subsection 2.3.3. A practical analysis showed that for the present system it is furthermore not possible to increase the time step size. The systems stiffness is dominated by other effects, e.g. the ring dynamics as well as the discussed single valued contact laws.
However, different constraining directions have a high influence on the solution. If the tangential direction at the saddle is treated with a set-valued force law the computation takes about 20% longer. If the tangential direction at the flanks is treated with a set-valued force law the computation takes about 350% longer. Combining the force directions lets the simulation time increase much more than linear. With respect to the CPU costs it is therefore beneficial to choose regularized contacts as long as the results of the simulation are considerably valuable.

Keeping the above discussion in mind and taking into account the current state of the model in combination with the available solvers, smooth contact laws are preferred everywhere except for the element-ring contact. There it leads to more precise results for the friction contact law.

3.3 Ring Models

In Subsection 2.1.2 different ring models are presented. In this section two points are discussed. At first four ring models are compared in a planar simulation. Based on the conclusions spatial simulations are compared to a planar reference.

3.3.1 Planar Comparison

This section presents the results from simulations with four different ring models which are all implemented in [21]. The LRVM model of [9, section 6.2] showed a very stiff behavior in the CVT application. In the current implementation it could not be tested. Improvements are suggested in [38] and are part of current research [10].
The four other models for the comparison are given in the following. The number of FEs for the three deformable models are chosen such that local effects are represented well. Thus, they are comparable to the other models. Thereby, the numbers of DOFs are as close as possible.

RCM It is the planar RCM implementation of the model of [25]. In the simulation 32 FEs are used, which yields 160 DOFs.

ANCF It is the planar implementation of the ANCF-theory of [58]. Forty FEs yield 160 DOFs.

ALE0 It is the planar implementation of Subsection 2.1.2 without local deformation. It only considers the two reference DOFs s and Θ.

ALE Compared to the ALE0 model it also considers local deformations with 157 DOFs and 40 FEs.

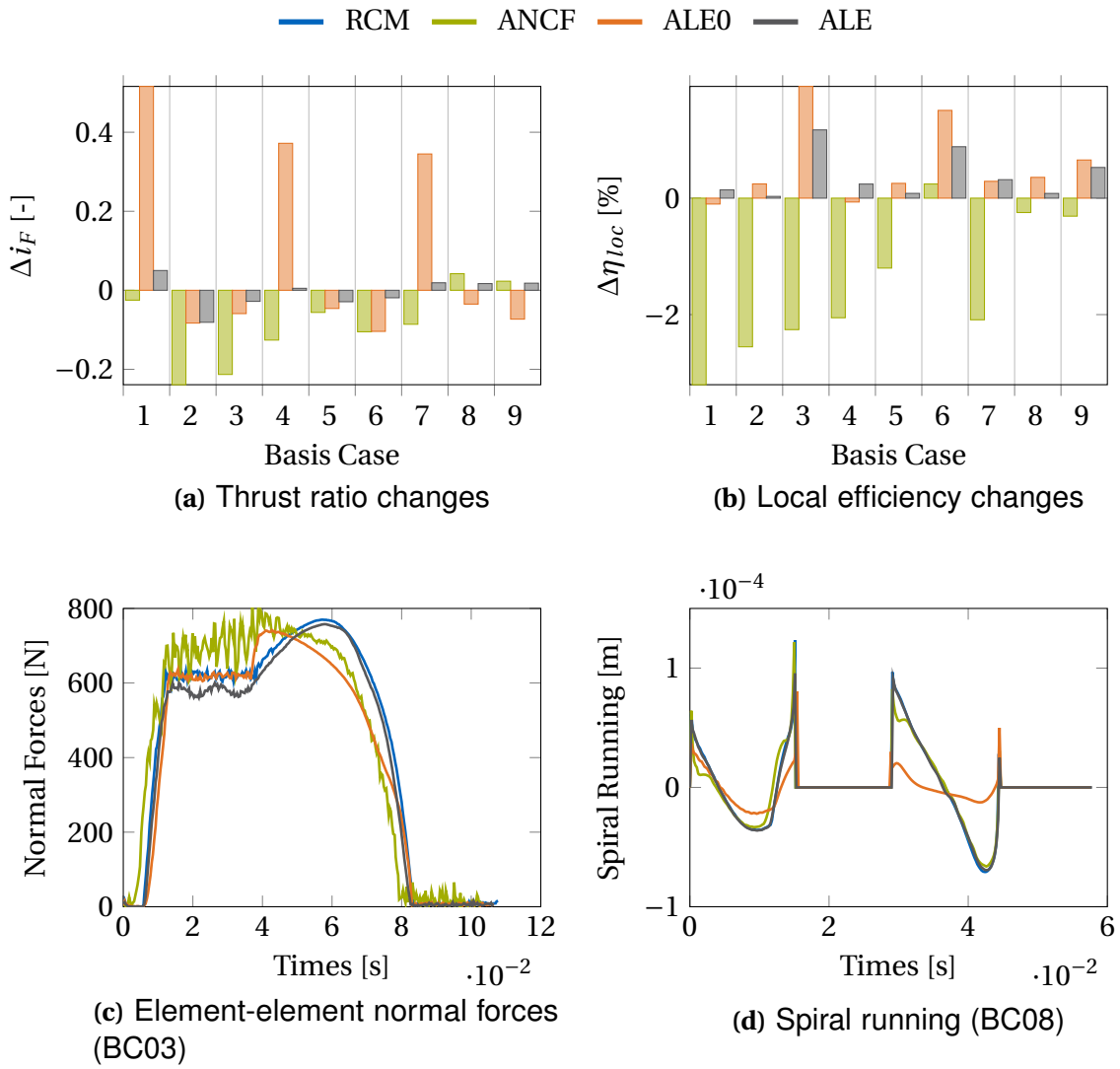

(a) Thrust ratio changes

(b) Local efficiency changes

(c) Element-element normal forces (BC03)

(d) Spiral running (BC08)

Figure 3.4: Comparing different ring models. The results gained with the RCM model are used as reference.

In Subsection 2.1.2 different options to choose the direction matrix $\mathbb{A}$ are introduced. For the application within the CVT the first option, i.e. the matrix is chosen to be the unity matrix and therefore constant, has proven to be most suitable. This results in less evaluated derivatives reducing the CPU time. Furthermore, Θ is not constant but oscillatory. This would change $\mathbb{A}$ and therefore the interpretation of the DOFs in every time step. Thus, the local DOFs "see" the oscillations in Θ resulting in numerical problems [28].

Figure 3.4 shows different aspects of general conclusions that could be drawn comparing the results of the cases in Table 3.1. Thereby, the output with the RCM model is used as reference as it was successfully tested in prior work [25, 9]. It can be seen that all models converge globally to the same level, i.e. a similar thrust ratio and efficiency (Figures 3.4a and 3.4b). Yet, the ALE0 model yields in OD very high values for the TR whereas the ANCF model yields low values for it in MED and UD configurations. Furthermore, higher losses compared to the other models result when using the ANCF model.
Figure 3.4c shows the reason for this. The ANCF model is very stiff and high oscillations result. For the efficiency computation this results in many oscillations around a zero level (e.g. after

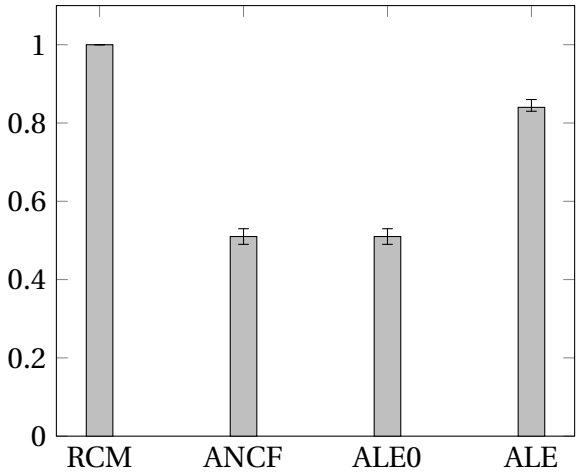

Figure 3.5: Average CPU costs for beam models where RCM is the reference. The error bars show the maximum deviations from the average value.

$t = 0.08s$) – even though these are smoothed due to the space averaging technique. This leads to errors within the numerical integration of the efficiency values. The ALE0 model deviates from the other three concerning spiral running (Figure 3.4d). As the model does not support local deformations along the belt only the contact stiffness enables small deviations from the circular arc. Therefore, the tendency is the same as for the other ring models. This also influences the axial force distribution along the arcs, which offers an explanation for the differences concerning i_F.

For the nine cases of Table 3.1 the computational times are compared in Figure 3.5. Again the simulation times of the RCM model are used as reference. The ANCF and the ALE0 model take up only about the half of the simulation time. The full simulation of the ALE model about 80% of the reference simulation time.

Altogether, the ALE model is a good reference model. The simulation time is reduced by ensuring a good correlation with an already validated RCM model. Depending on the application it is easy to adjust the level of detail reducing the simulation times even more. Therefore, the ALE model is chosen as standard model for the other simulations.

3.3.2 Spatial Analysis

For the RCM model a spatial variant is implemented [54, 21]. The time-step size is limited, i.e. spatial simulation could not be performed in a reasonable time. The additional considered DOFs lead in combination with the stiff material and the unfavorable geometry to very stiff behavior. Numerical standard damping strategies could be used, but with it global DOFs are damped as well. The rings stop to move which is an unfavorable behavior. More dedicated damping strategies which damp only those DOFs that do not contribute to a rigid-body movement, could not be applied successfully.
Due to the Eulerian description within the ALE model, a spatial reference deformation respecting the misalignment can be added on kinematic level. This is not possible for the other models as Lagrange coordinates are used. This technique avoids high stiffness in axial direction.
Using this technique in combination with the ALE0 beam, simulations can be performed

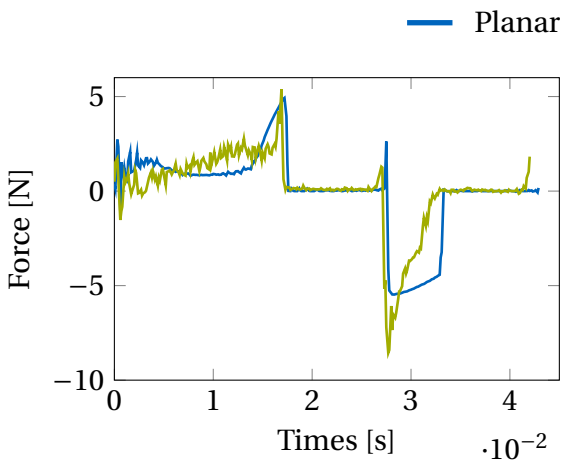

(a) Element-ring frictional forces in longitudinal direction (BC01)

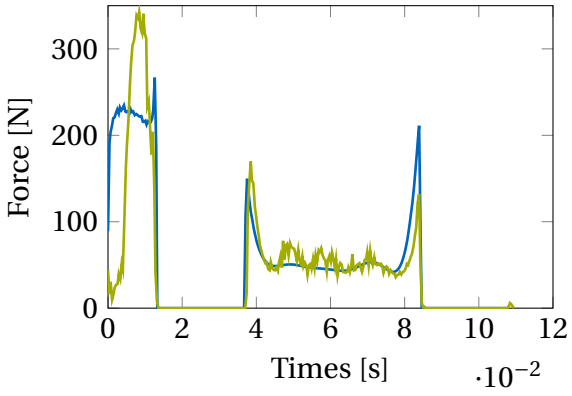

(b) Element axial forces (BC06)

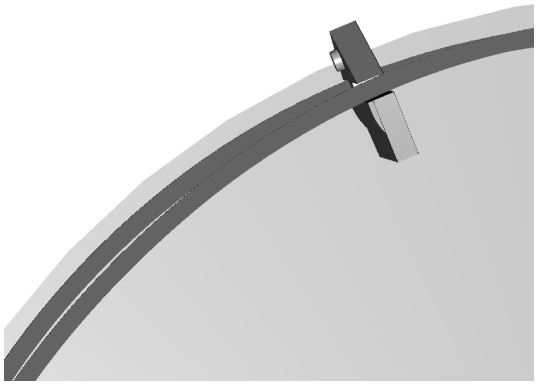

(c) Distorted element due to spatial ring deformation

Figure 3.6: Exemplary curves comparing results from spatial and planar models.

robustly which is not the case for any other of the mentioned models.
Comparing the nine cases of Table 3.1 a spatial simulation takes at average 8.1 times longer than the planar reference. Local and global curves show strong numerical oscillations which are not apparent in the planar case (Figure 3.6). The overall trends are presented well along the belt. Locally however, deviations arise, e.g. at the idle arc in the PRI.
It is remarked that including ring deformation leads to distorted results. The differences in stiffness between loose and fixed sheave in both arcs yields a rolling of the element (Figure 3.6c). The rings deform at the left and the right side differently which finally terminates the simulations. All in all there is a demand for further research. No results from spatial simulations are used in this work.

4 Physical Aspects

The models sensitivity on numerical parameters is treated in the previous chapter. Physical parameters are treated separately in this thesis. Their value cannot be measured exactly, e.g. contact stiffness or friction. Thus, they are varied to show the models sensitivity on them. This serves two major goals. On the one hand it shows the uncertainty of the model and thus the updating possibilities of it. On the other hand it offers the basis for further improvement strategies for future design.
This chapter discusses the quality of the complete model on basis of the variations of the most crucial parameters. It is intended to show possible variations of the model's output when the parameters are not known. Again the nine cases of Table 3.1 are used to draw general conclusions. They are sorted wrt. the ratio in Table 4.1.

OD	MED	UD
1,4,7	2,5,8	3,6,(9)

Table 4.1: The basis cases (Table 3.1) sorted with respect to the speed ratio. The applied torque increases in each column with the number.

Due to production uncertainties, the assembly conditions of the belt is not precisely known. Thus, the influence of the endplay, i.e. the number of elements on the belt is studied at first in Section 4.1. The connection between elements and pulleys is analyzed in Section 4.2. Different contact positions as well as the element's axial stiffness show an impact on the overall system behavior. In contrast to the RE, where the contact geometry is defined due to the circular shape, the contact geometry at the head is not defined precisely. The radial and the longitudinal variation of the contact point yields high influences on the system behavior as demonstrated in Section 4.3. Finally, the friction coefficients are analyzed. Due to production and assembly the contact parameters vary, which changes the influence functions. This is treated finally in Section 4.4.

4.1 Real Elements

In Section 3.1 the influence of the number of simulated elements N_E is studied. The right choice is important to get valuable results. Another important measure is the number of elements N_{E0} that are really within the belt. Practically, the belts get assembled by experienced workers. A test where the belt is lifted with sticks clamped in the assembled belt is used to evaluate if the right number of elements are used. This test cannot be simulated. It depends on the correct representation of the element-element force, which is discussed in Subsection 2.2.3 as well as the friction values. The push-forces between the elements are in the exponential

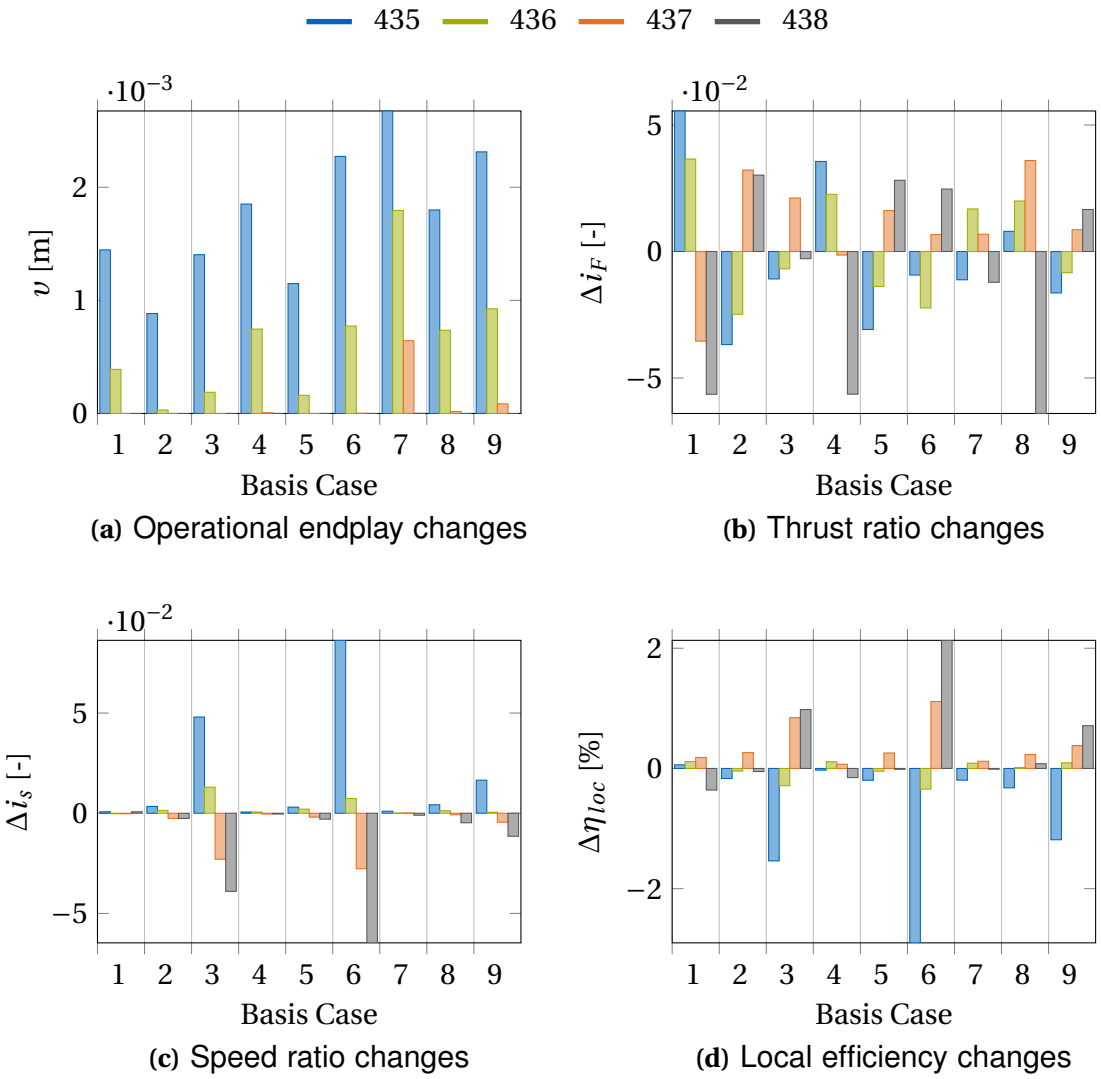

(a) Operational endplay changes

(b) Thrust ratio changes

(c) Speed ratio changes

(d) Local efficiency changes

Figure 4.1: Comparing global values varying the number of real elements in the belt for the cases in Table 3.1. If a Δ-value is shown, the average of all simulations for each case is used as reference.

part (Figure 2.9) for testing. For different belts using different element-geometries as well as rings it probably differs. For the same belt setup using the same elements and rings differences arise due to production as well. No recording is done for the measurements. Furthermore, wear can effectively change the output. It is not known which value for N_{E0} should be used exactly.
Practically, it can be assumed that $v = 0$m while running at low loads. This value changes due to the load. For the given cases of Table 3.1 in combination with the reference geometries practical tests result in a number between 436 and 437. In the following, four different cases with 435, 436, 437 and 438 elements have been used to investigate the influence on the output of the belt.

In all simulations a stationary point is found, i.e. the belt system transfers the applied loads. The resulting global output values are depicted in Figure 4.1. The OEP decreases with N_{E0} until it is 0m, which is always true for $N_{E0} = 438$ (Figure 4.1a). For $v = 0$m the overall push-force level increases within the belt (Figure 4.2b).

The thrust ratio changes show the complexity of the system. For low loads it decreases in OD but increases in MED with N_{E0}. In UD it is not affected but fluctuates only slightly. This results from different mechanisms. The most important ones are treated exemplary in the following. It shows the benefits of the present model, i.e. a detailed analysis of the global effects based on local outputs.
All local curves change with increasing N_{E0}, e.g. the axial force distribution, the spiral running, the push-forces, the relative velocities as well as the element-sheave pitch. The changes influence each other in a complex manner such that not one singular effect can be named. It is out of scope of this work to discuss all local influences in detail. For BC01, BC02 and BC03 local curves are given in Figure C.1 for the following general discussion as an example.

With increasing N_{E0} the ring tension gets higher. In OD the tension forces contribute negatively to the torque equilibrium. Thus, more push-forces have to be build up in the active arc (Figure 4.2b). The differences between tension forces and push-forces decrease effectively. A lower F_P is sufficient reducing i_F consequently.
For MED and UD the ring tension contribution to the torque equilibrium turns around.[1] Remark that the discussed MED configurations all fulfill $i_s > 1$. Thus, the increase of N_{E0} influences i_F in an opposite manner. In MED i_F increases with N_{E0} consequently. In UD further mechanisms become more important as the PRI shortens. The OEP decreases with increasing N_{E0}. The idle arc shortens and thus the active arc becomes longer (Figure C.1 shows negative element-pulley friction forces in longitudinal direction in the PRI for $N_{E0} = 437$ and $N_{E0} = 438$). More push-forces can be build up due to this. The primary clamping force F_P must increase, i.e. i_F increases. This mechanism works against the decrease of i_F due to the ring-tension turnaround. Besides, the slip reduces at the PRI leading to an increased overall belt speed, i.e. a lower i_s (Figure 4.1c). The losses reduce as well (Figure 4.1d).
For increasing loads the rings elongate more and the push-force level increases as well. The OEP increases consequently and thus the differences in the tension forces decrease. The discussed mechanisms become less dominant.

The change in the element-sheave pitch ψ is pointed out here. It can be accessed by measurements and therefore is of interest for the validation. It is affected greatly – especially in the PRI – as given in Figure 4.2a. As the push-forces increase in the PRI the nonlinear behavior of the longitudinal element deformation is a crucial parameter here, which directly follows from Figure 4.2b. One can conclude that ψ is very sensitive to the force and with it to all parameters changing this force.

4.2 Element-Pulley Contact

It has been emphasized before that the contact between element and pulley-sheaves is a crucial part within the modeling. It is parametrized with values, that cannot be measured and thus are updated, i.e. identified with simulations, in practice. The two crucial parameters are the position of the contact point along the flank height and the stiffness of the element in axial direction. The influences are discussed in the following starting with the position.
It is remarked, that both approaches for the flank coupling (Subsection 2.2.2) lead to very similar results. A maximal deviation of 0.05 in i_F and 0.23% in η_{loc} result. For the simplified approach the simulation times reduce up to 7%.

[1] see e.g. element-ring longitudinal friction forces pointing in opposite direction

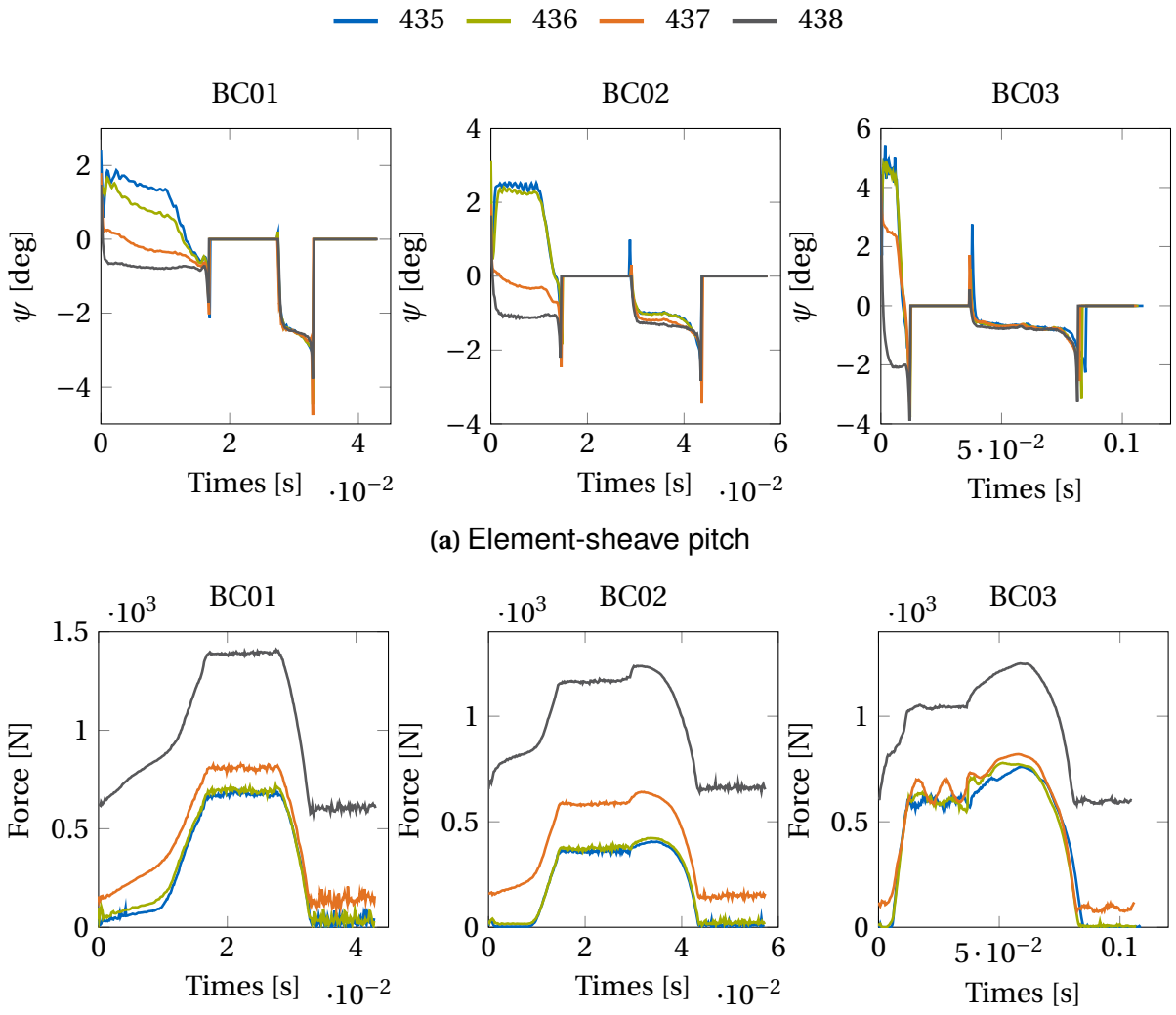

(a) Element-sheave pitch

(b) Element-element normal forces

Figure 4.2: Comparing local values varying the real elements. The first three cases of Table 3.1 are presented.

4.2.1 Contact Position

In fact the contact force between flank and sheave is a pressure distribution that arises due to deformation of the contacting partners. For the CVT model one contact point is used. Besides the contact search, the solution of the contact force law is more efficient enabling fast integration times. It gets unclear where the contact point in the simulation should be. A sensitivity analysis is therefore presented. An optimized estimation for measurements results. It may further serve as basis for improvement strategies.

To compare the influence of the contact height, it is varied along the flank (Figure 4.3). The relative height $\bar{h}_F$ is defined to be the ratio of the actual height h_F of the contact point on the flank to the height of the saddle h_P [54, Figure 2.3]. It is varied linearly from $\bar{h}_F = 1$, i.e. contact at the saddle, to $\bar{h}_F = 0.6$. For smaller values the simulations show increasing oscillations, which results in partly unusable output.

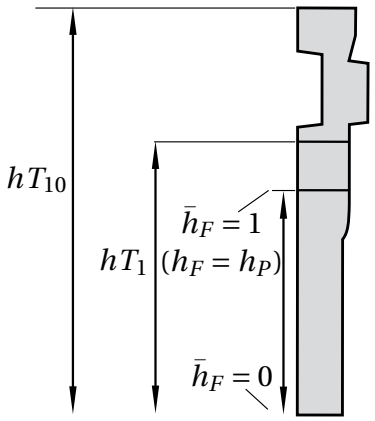

Figure 4.3: Element height measures

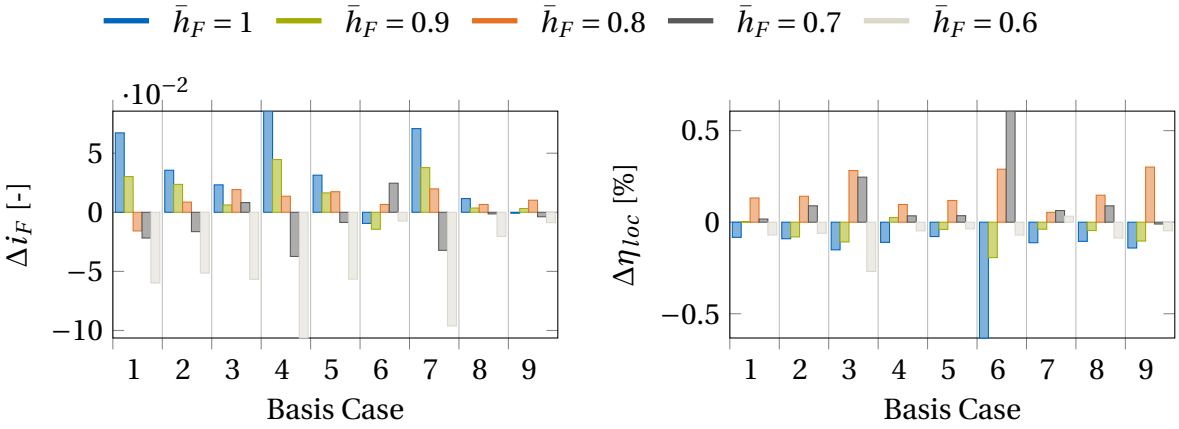

(a) Thrust ratio changes

(b) Local efficiency changes

Figure 4.4: Comparing global outputs varying the flank contact point heights $\bar{h}_F$ at the element flank. The average of all simulations for each case is used as reference.

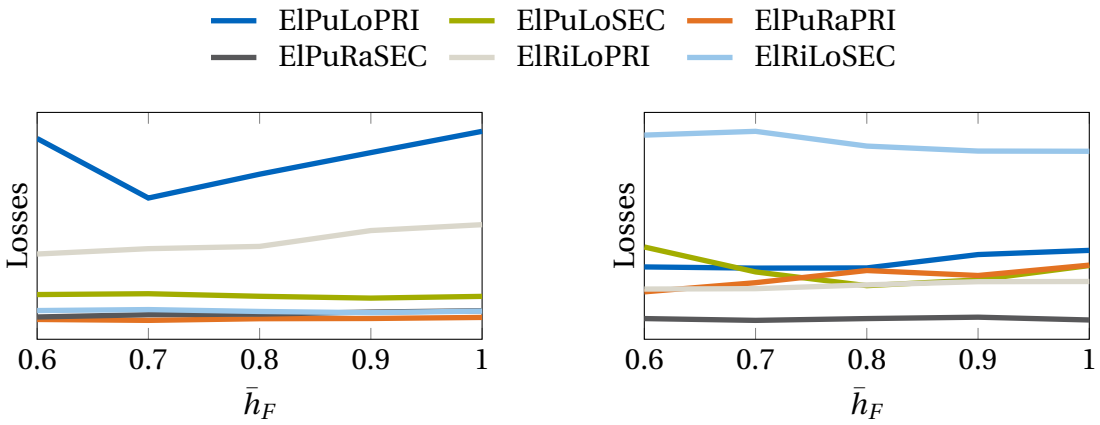

(a) Main losses for BC04

(b) Main losses for BC06

Figure 4.5: Main losses for two different ratios varying the flank contact point heights $\bar{h}_F$.

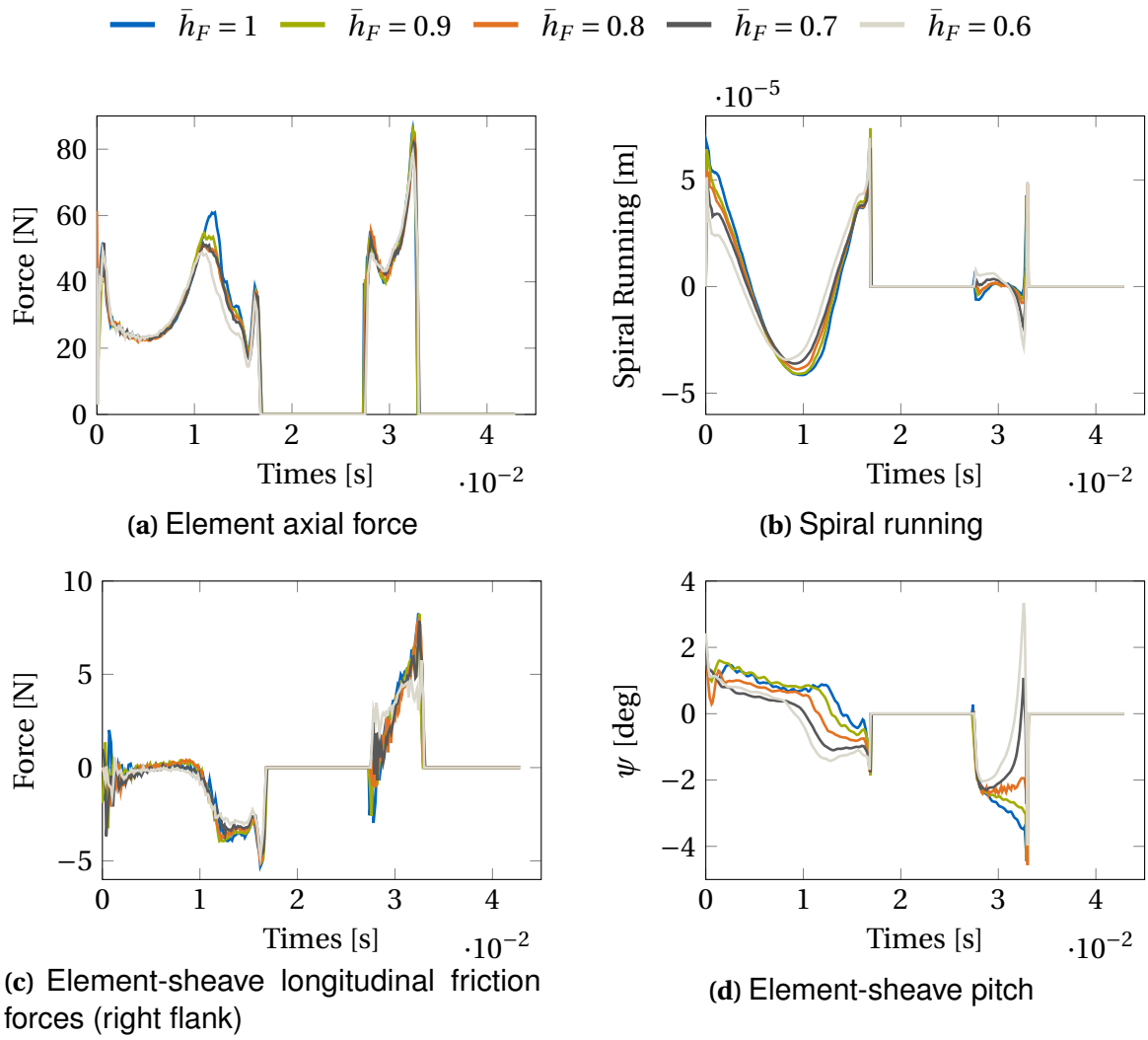

(a) Element axial force

(b) Spiral running

(c) Element-sheave longitudinal friction forces (right flank)

(d) Element-sheave pitch

Figure 4.6: Local output curves of BC01 varying $\bar{h}_F$.

The TR decreases with $\bar{h}_F$ (Figure 4.4a). This effect is stronger in MED and OD and for low loads. Besides, the efficiency is affected. It has a maximum[2] for $\bar{h}_F \approx 0.75$ and decreases for higher or lower contact points. The loss mechanisms impact the efficiency differently for the cases as shown in Figure 4.5 proving the benefits of a nonlinear model. It offers the possibility to investigate the system to enable further optimization.

Due to the variation of $\bar{h}_F$, two principle changes are done within the system. The influences are exemplary discussed for BC01. The corresponding curves are presented in Figure 4.6.
On the one hand the contact radii along the sheaves are changed. A new distribution of the element axial forces results directly impacting i_F (Figure 4.6a). It also affects the spiral running (Figure 4.6b). Together with the shifted contact point, the lever arms for the longitudinal friction forces change. The contribution to the torque equilibrium is altered. The longitudinal friction force contributes less to the torque equilibrium for decreasing $\bar{h}_F$. Due to the constant boundary conditions in the SEC, i.e. F_S = const. and M_S = const., the distribution of the frictional forces adapts correspondingly in longitudinal direction (Figure 4.6c).
On the other hand the local kinematics of the elements are changed due to the lever arm. The element-sheave pitch changes analogously (Figure 4.6d) which influences the local kinematics as well. Altogether, a new stationary point is found. The frictional forces in

[2] depending on the case

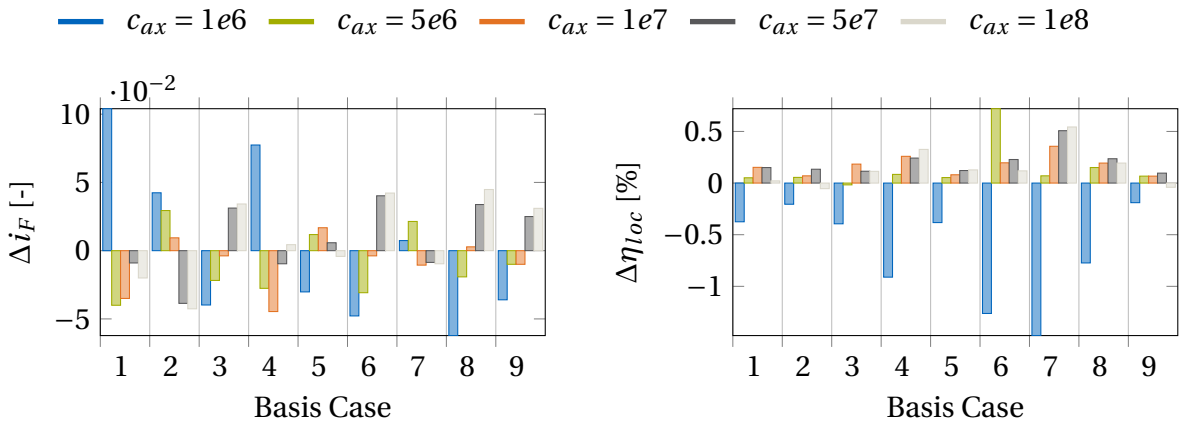

(a) Thrust ratio changes

(b) Local efficiency changes

Figure 4.7: Comparing global outputs for different axial stiffness c_{ax} of the element. The average of all simulations for each case is used as reference.

longitudinal direction between flank and sheave in the PRI are reduced. Less clamping force F_P is sufficient lowering i_F. The discussion serves as an example, that the nonlinear effects, which are active within the system, depend on the boundary conditions as well as the parameter setup.

4.2.2 Element Axial Stiffness

Besides varying the height position along the flank, the axial stiffness c_{ax} of the element is investigated. Estimating it with $c_{ax} \approx \frac{EA}{l}$ where E is the Young's modulus, A the cross-section of the flank in axial direction and l the local width of the element, it is bounded to approximately $c_{ax} \in [1e6\frac{\mathrm{N}}{\mathrm{m}}, 1e8\frac{\mathrm{N}}{\mathrm{m}}]$. Global outputs for a linear variation of c_{ax} in this range are presented in Figure 4.7.
The efficiency increases with c_{ax}. This is consistent to the results of [39, section 5.2.2]. The present model allows deeper analysis of the losses which is exemplary done in the following for BC07.
The TAP shifts in negative longitudinal direction in the PRI when c_{ax} increases. This reduces the longitudinal frictional forces (Figure 4.8a). This coincides with the results from the present model (Figure 4.8b[3]) and with [39]. However, the relative velocities do not increase and thus the losses in the PRI in longitudinal direction are barely affected (Figures 4.8c and 4.8e).[4]
These losses decrease for stiffer elements in the SEC as the relative velocity decreases. Furthermore, the spiral running in the SEC decreases and consequently the radial losses. This is identified as the main contribution for the overall reduced losses (Figures 4.8b and 4.8e). The normal forces between element and rings reduce as the radial frictional forces are affected (Figures 4.8b and 4.8d). This reduces the longitudinal friction force and with it the overall losses.

As discussed, the force distributions are influenced by the spiral running. To explain the differences in i_F one has to analyze the axial forces. In the SEC this distribution is not affected. In the PRI it is. The TAP shifts and with it the distribution. In case of a low level of F_P the

[3] marked by the sign change from negative to positive
[4] In other cases these losses are even increased as the active arc is larger for higher stiffness!

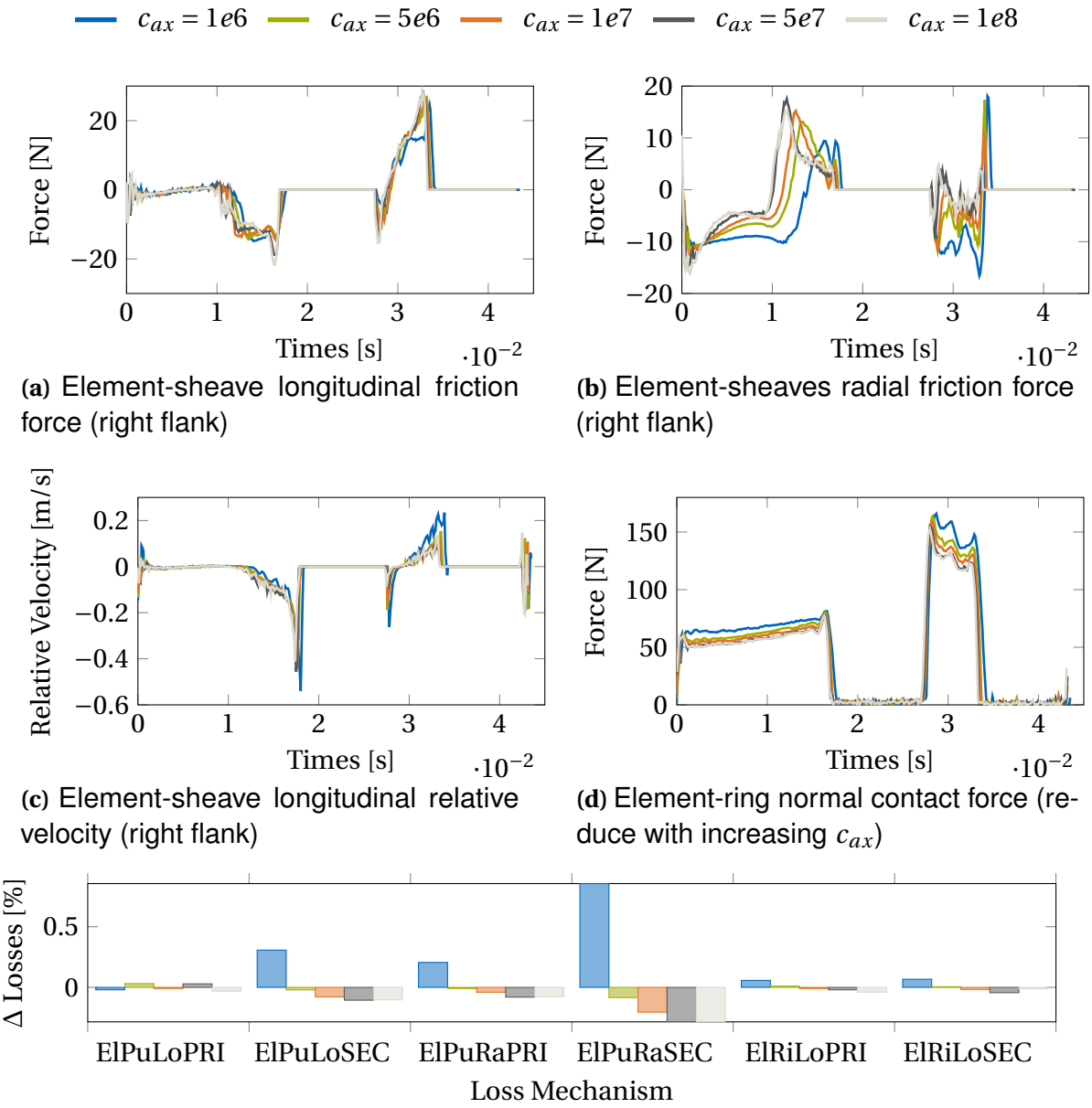

(a) Element-sheave longitudinal friction force (right flank)

(b) Element-sheaves radial friction force (right flank)

(c) Element-sheave longitudinal relative velocity (right flank)

(d) Element-ring normal contact force (reduce with increasing c_{ax})

(e) The three main loss mechanisms within the pushbelt CVT for PRI and SEC. The average of all simulations for each case is used as reference.

Figure 4.8: Comparing local results varying the axial stiffness c_{ax} for case BC07.

peak at the TAP stays low. It only shifts decreasing[5] i_F (Figure 4.9a). For high clamping forces the peak increases as well, which is a result from the solution of system (2.34). In this case i_F increases (Figures 4.9b to 4.9d).
For small running radii at the PRI, i.e. in UD, the clamping force at the PRI F_P is always at a high level. Thus, the TR does increase with the stiffness. For large running radii, i.e. in MED and OD it depends on the load case. For high loads F_P is at a high level as well and i_F is increased. For low loads F_P is at a low level and i_F decreases.

[5]The small differences in BC01 for 5e6 and 1e7 result from numerical post-processing.

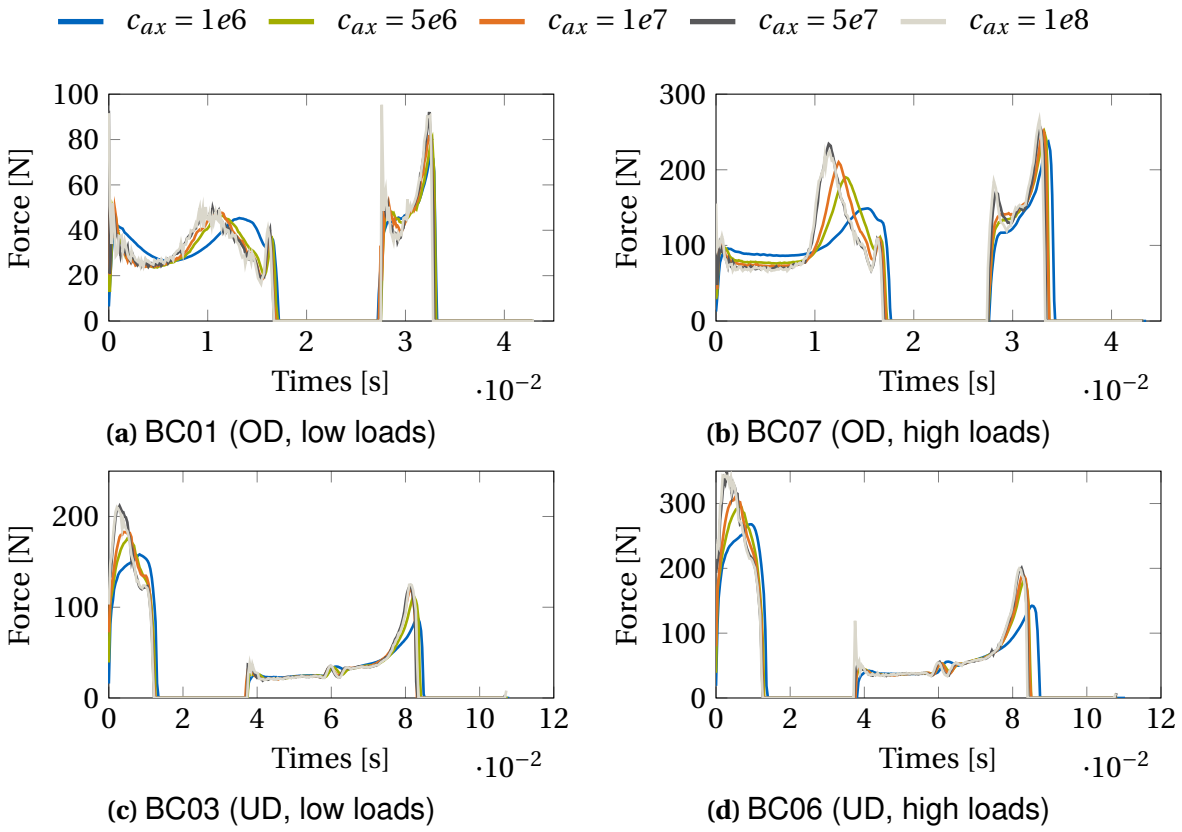

Figure 4.9: Element axial forces along the belt for different cases in OD and UD.

4.3 Element-Element Contact

To measure the push-forces sensors are typically attached at the RE [23, 56]. In the arcs this measures the full force as no contact is active at the head. In a strand however the contact at the head closes. The push-force is divided into forces at the RE and the head. This section treats the contact kinematics at the head varying on the one hand the radial and on the other hand the longitudinal position, i.e. the thickness.

4.3.1 Radial Variation

Four different height positions are presented from a variation of nine linear steps between the height of the ear (hT_1) and the uppermost position (hT_{10}) of the element (Figure 4.3). All cases of Table 3.1 are compared. Figure 4.10 shows the partition of the normal forces for BC01 and BC06. At the upper row the sum of the push-force is depicted. The lower row shows the forces at the RE and the head separately. One can observe, that indeed only in the strands forces are acting at the head. The higher the contact point is the less force is acting at the head. This conclusion is true for all nine cases. Global values are not affected by this. The maximum standard deviation for the thrust ratio is 0.009 and for the local efficiency 0.13%. Thus, the mechanism can be used to update the position for the head contact.
This mechanism explains the flaw in the measurements. However, in the measurements a stronger partition is observed, that cannot exclusively by explained the height position of the contact point. Besides the radial position of the contact point, the longitudinal position, i.e. the thickness, plays an important role for the partition of the forces which is discussed in the

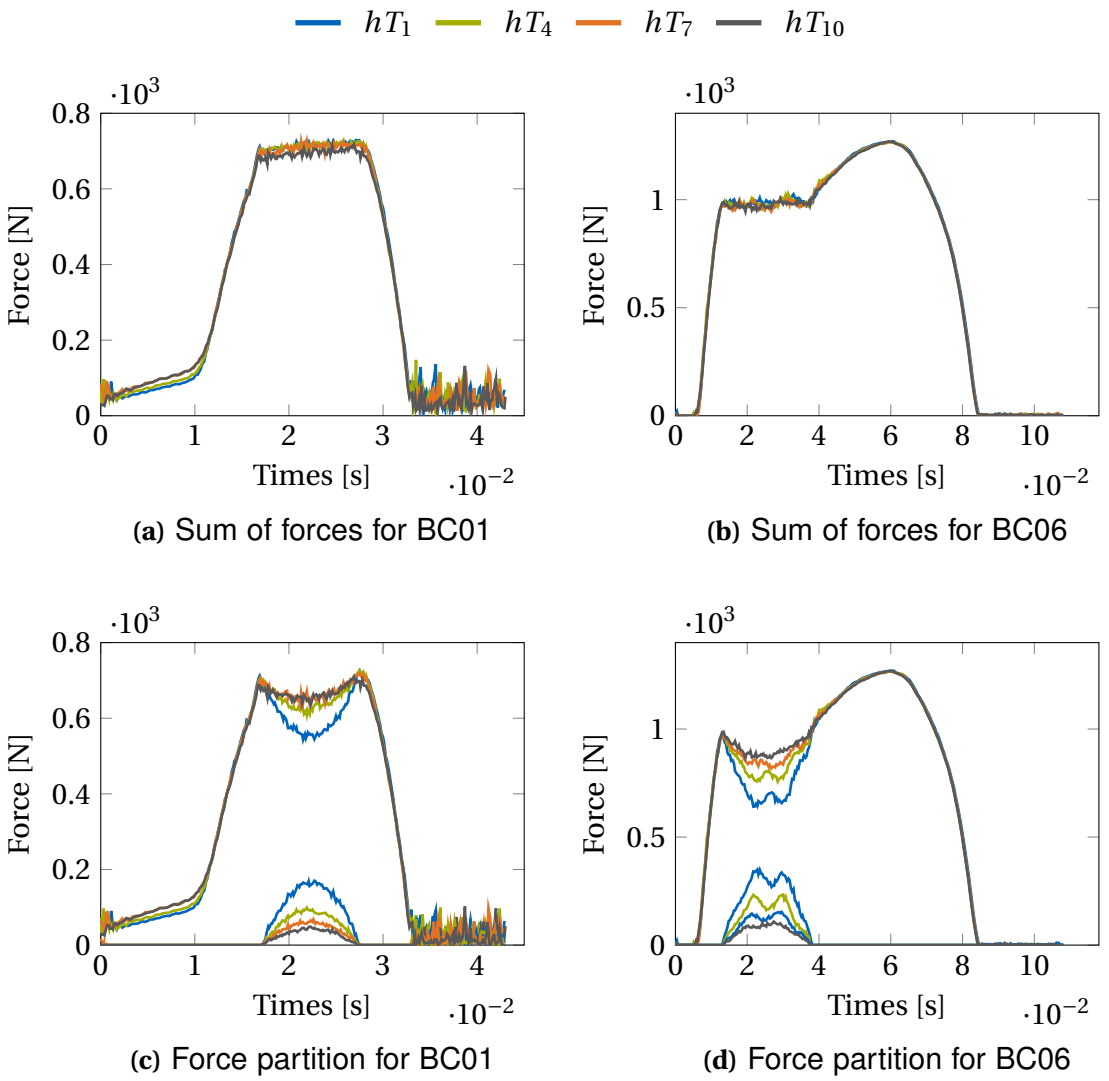

(a) Sum of forces for BC01

(b) Sum of forces for BC06

(c) Force partition for BC01

(d) Force partition for BC06

Figure 4.10: Push-forces, i.e. element-element normal forces, varying the head contact point height. Given is the force partition between the head and the RE (lower row) as well as their sum (upper row).

following.

4.3.2 Longitudinal Variation

CEBULLA introduced tapering of the elements to respect manufacturing processes [9]. Effects on the OEP at the head[6] are evaluated. Yet, a deeper analysis is missing to evaluate further influences from this. This section is intended to close this gap.
It is remarked that the initialization process described in [9, Section 4.2] does strongly depend on the respective boundary conditions. The nonlinear system introduced in [54] utilizing the model of [51] cannot be solved robustly. A simpler initialization strategy is therefore chosen pre-stressing the elements. It leads to a longer transition phase, yet to a robust integration.
The reference $tT_1 = 1.5$mm was chosen to be the thickness at the RE making it a flat element. Nine linear steps between tT_1 and $tT_{10} = 1.518$mm are used to analyze the differences be-

[6] CEBULLA uses the phrase “Top”

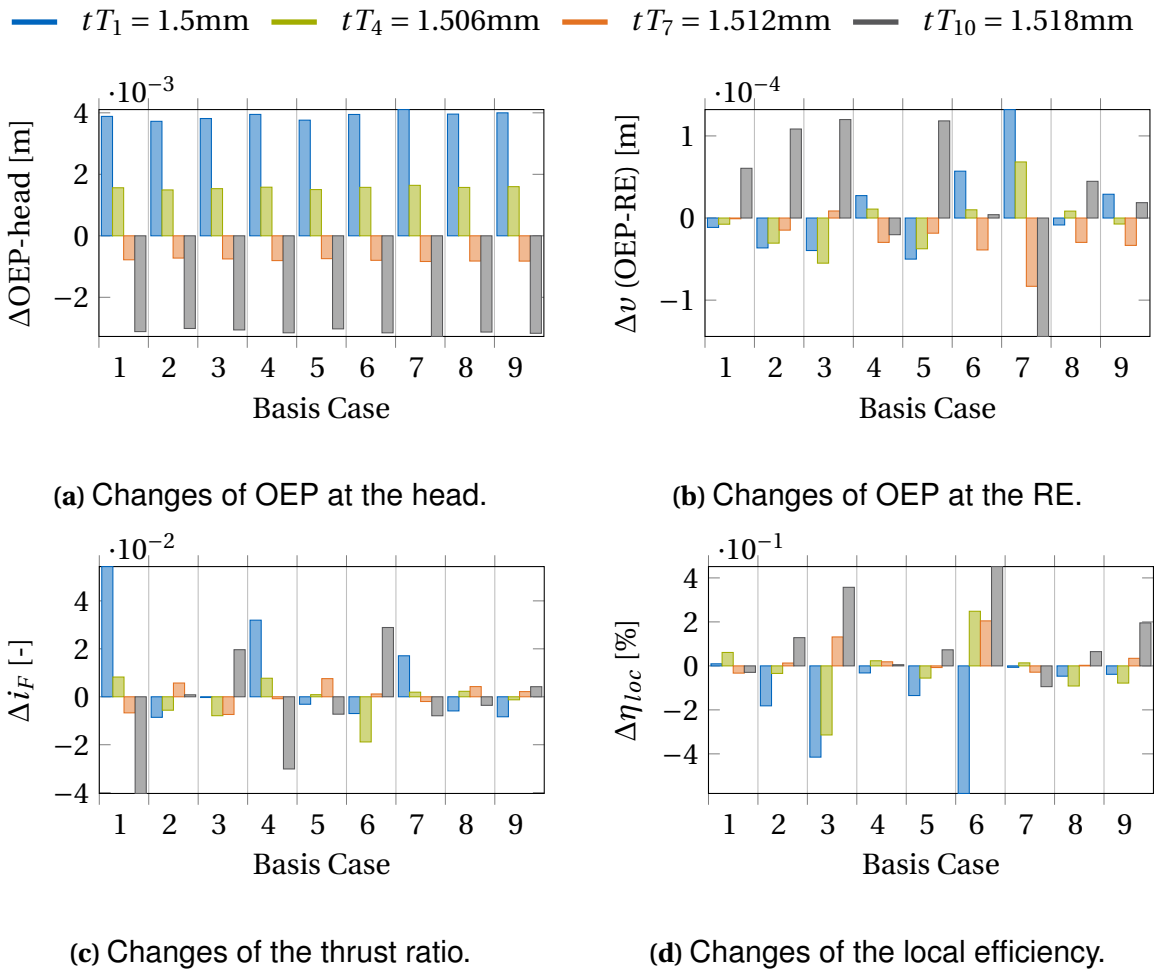

(a) Changes of OEP at the head.

(b) Changes of OEP at the RE.

(c) Changes of the thrust ratio.

(d) Changes of the local efficiency.

Figure 4.11: Comparing global outputs varying the thickness tT of the head. As reference the average value resulting from ten different thicknesses is used.

tween the simulations. The global results are given in Figure 4.11 where the average of all ten cases is used as reference.

Figure 4.11a shows that the OEP at the head reduces in all cases which is clear as the thickness is increased coinciding with the results of [9]. The OEP at the RE is one order of magnitude smaller than the one at the head. No clear trend is visible – the differences arise mainly from numerical calculations.

Figure 4.11d shows that the efficiency increases for MED and UD. For the OD configuration the efficiency is not affected with a clear trend. Figure 4.12a presents the distribution of the losses for BC03. It is clear that the losses get less in the longitudinal direction in the PRI for both contacts, i.e. for element-pulley as well for the element-ring contact. This can be explained by a reduced relative speed of both partners coming from an increased overall element velocity.
In the loose-strand a (small) contact force at the head arises (Figure 4.12b). Therefore, the oscillations are reduced and the elements are guided better along the belt without losing as much energy as when the elements are flat. This increases the overall velocity of the elements (Figure 4.12c). Consequently, the relative velocity between elements and rings in the idle arc of the PRI is reduced and therefore the losses due to this contact (Figure 4.12d). In the active arc this lets the elements decelerate less in the active part of the PRI, which reduces also the relative speeds between flank and sheave (Figure 4.12e). Altogether, the power losses

are reduced. Remark that in the OD configurations this phenomenon is not apparent for all load cases and thus no efficiency gain can be observed.

Besides these discussed effects, which explain the change in the efficiency measures, locally further phenomena arise. The partition between head and RE forces in the push-strand is influenced as one can conclude from Figure 4.12b. The effect is even stronger than for only varying the height positions.
Furthermore, the element-sheave pitch is affected (Figure 4.13). It is reduced in low load cases for increasing thickness. The push-forces in the push-strand are not high and for flat elements the strand is straight. For thicker elements however, the strand gets bended a little due to the higher force at the head and there is contact between elements and rings. Consequently, the pitch angle of the elements is affected which gets reduced in these load cases. Higher loads lead to higher head forces also for flat elements and thus the differences between the simulations vanish (Figures 4.13c and 4.13d).

Global oscillations arise typically in the UD configurations. The signals for the TR and the SR show the same frequency. These overall oscillations, that are active in the system, get reduced, if the thickness is increased. This correlates to the observation above and results from the enhanced guidance in the loose-strand of the elements.
The value for i_F is only affected for low loads in OD (Figure 4.11c). Otherwise the changes are in the order of 10^{-2} and result from numerical influences. Analyzing the local curves yields no clear explanation.

4.4 Friction

In the literature typically an overall friction value of the belt is identified using the Coulomb theory, i.e. a constant value [44]. For the present model however, not only one contact pairing is present, i.e. flank to sheave, but also the contact between elements and rings and element-element contacts are considered.
It is expected that oil has an influence on the friction. A velocity dependent friction coefficient based on Stribeck theory is used. A normal force influence is neglected assuming to be of minor significance compared to the velocity dependency. The following function is used to approximate the friction coefficient μ wrt. the relative tangential velocity v_t in the contact

$$\mu(v_t) = \mu_0 + \frac{\mu_1}{1 + \mu_2 v_t^k} \tag{4.1}$$

where μ_0, μ_1, μ_2 and k are parameters to this function.
In the following the flank-sheave contact is investigated using different constant friction coefficient functions. Then the same parameter variation is done for the element-ring contact. Thereby, velocity dependent friction functions are treated.

4.4.1 Element-Pulley

The friction between the flank of the element and the pulley-sheaves is crucial within the CVT. Higher torques can be transmitted for same clamping forces the higher the friction coefficient

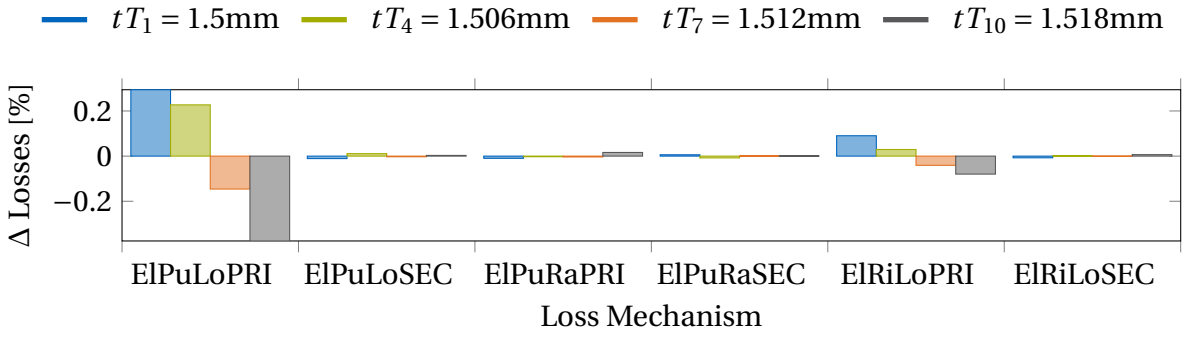

(a) Losses – as reference the average value from the shown cases is used.

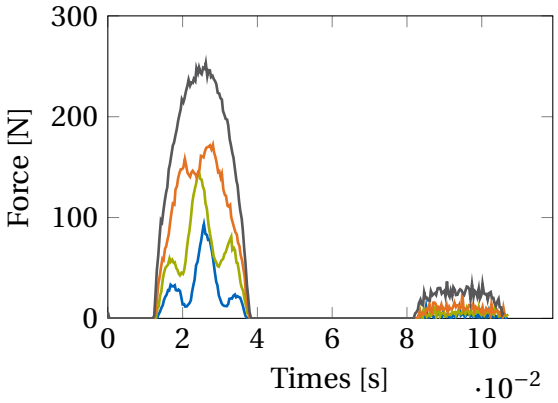

(b) Element-element normal forces at the head

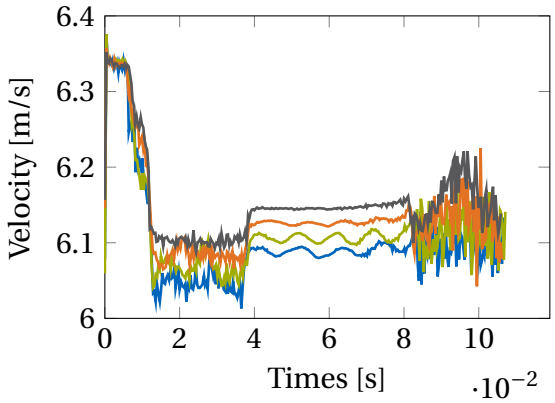

(c) Element velocity along the arc

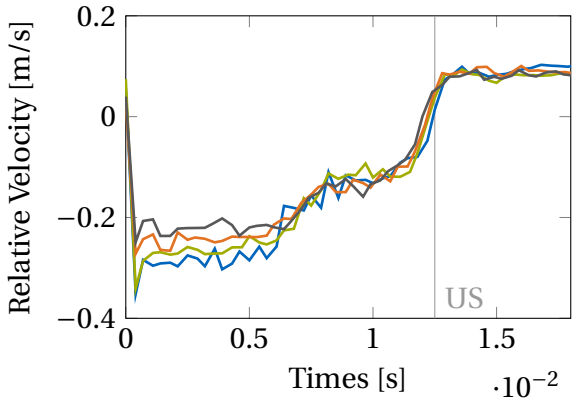

(d) Element-ring longitudinal relative velocity (in the PRI)

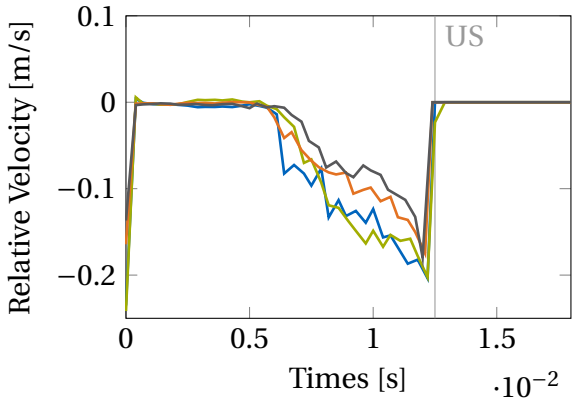

(e) Element-sheave longitudinal relative velocity (right flank in the PRI)

Figure 4.12: Losses of BC03 varying the thickness of the head taking into account relative velocities.

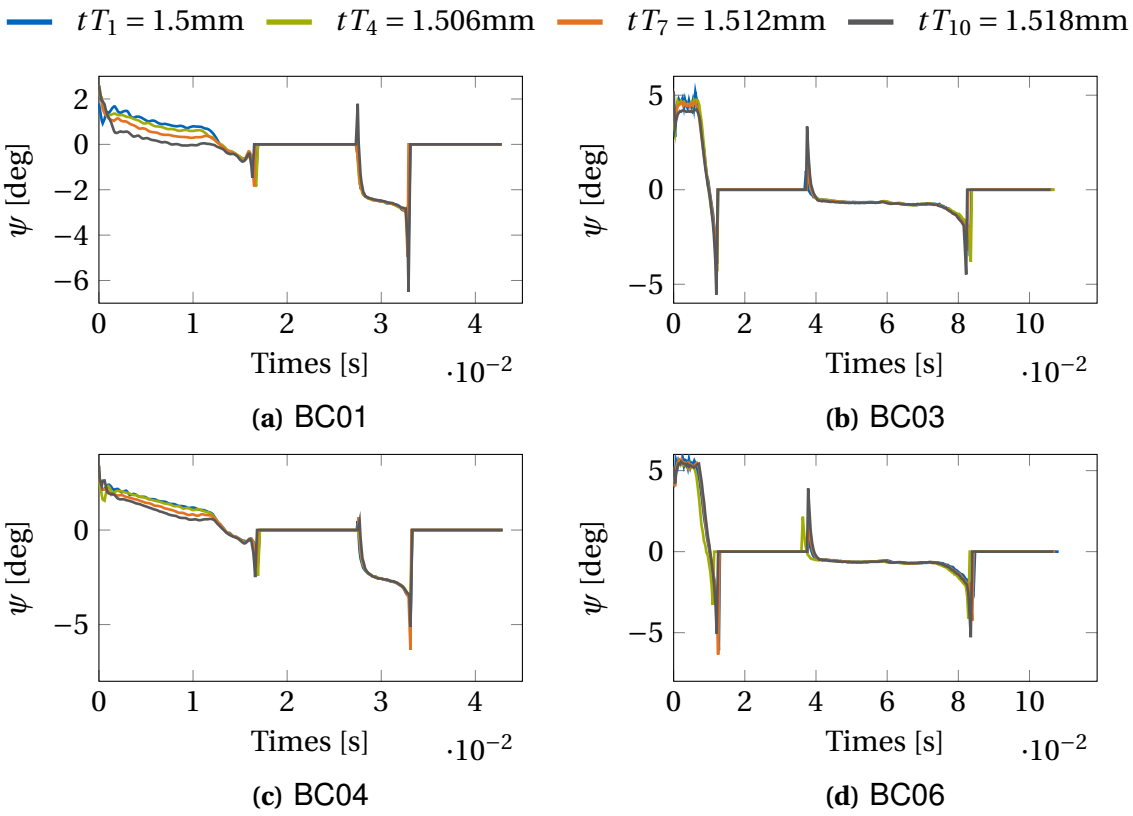

Figure 4.13: Comparing the element-sheave pitch varying the thickness of the head for low and high loads

is. This can reduce the losses that arise from high clamping forces. The internal dynamics of the belt and with it the losses are studied in this section.

For the nine cases of Table 3.1 a constant friction coefficient is varied in the technical range of $\mu = 0.12$ to $\mu = 0.09$. Figure 4.14a shows an decreasing i_F with decreasing friction which is in accordance with the findings of [65, 37]. Keeping in mind, that the boundary conditions are the same for all simulations, i.e. in particular the same torque and clamping force at the SEC, the safety (2.49) is decreased. Figure 4.14c shows a decreased frictional force at the PRI. The idle arc decreases consequently lowering the safety. For increasing loads and increasing i_s the influence gets stronger. In both cases relatively high F_P are necessary for the torque transmission pronouncing this effect. It is remarked, that for a constant safety value the necessary clamping forces will reduce when increasing the friction coefficient. This is a typical enhancement strategy for the system [63]. It would make another boundary condition variation necessary which ensures the same safety.
The overall efficiency is affected due to competing mechanisms. Due to the longer active arc, the relative sliding duration between element and sheave within the arc is longer as well. The force however is reduced decreasing the power loss again. Besides, the internal dynamics is affected. Especially for BC06 this is evident. Belt oscillations are induced for increasing μ leading, for $\mu = 0.12$,[7] to an overall changed dynamics of the system (Figure 4.14d for the speed ratio). The model suggests, that a short active arc in a high load case leads to an excitation of the push-strand. The mechanism yields similar results as the “scratch” phenomenon [46]. Yet, it arises for high load conditions for which the NVH phenomenon “gear rattle” does not result. However, it is an interesting parameter to study in future works.

[7] for higher friction coefficients the same behavior is observed

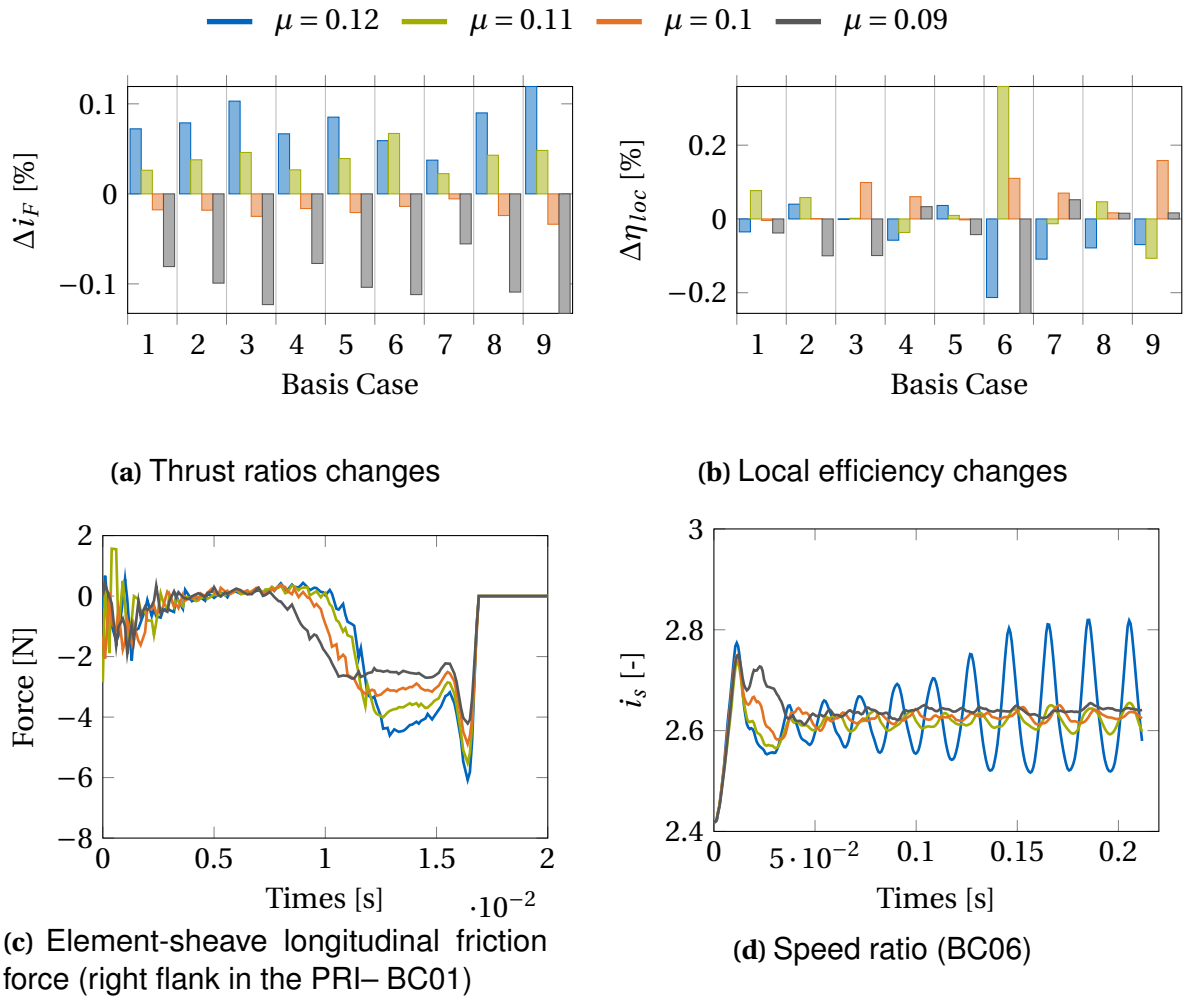

(a) Thrust ratios changes

(b) Local efficiency changes

(c) Element-sheave longitudinal friction force (right flank in the PRI– BC01)

(d) Speed ratio (BC06)

Figure 4.14: Comparing local curves varying the Coulomb coefficients for the element-pulley contact for the cases of Table 3.1. The average of all simulations for each case is used as reference for the global comparison.

4.4.2 Element-Ring

While the rings guide the elements, the (relative) velocity between the partners is driven by the friction. It thus defines the tension differences in the rings and with it the push-forces in the strands. Furthermore, it is assumed to be an important parameter to the phenomenon of "gear rattle" [46].

Coloumb

Constant values are varied between $\mu = 0.08$ and $\mu = 0.12$. The value of i_F is not affected by the change with a maximum standard deviation of 0.009. The local efficiency is however affected differently for varying i_s and loads (Figure 4.15a). In the MED cases no changes are expected. The rings have low relative velocities in the arcs and thus the losses are small. The tension difference is of minor importance for the global torque equilibrium. This is confirmed by the simulations.
In case of UD or OD this is not true. The losses between elements and rings increase with higher friction in both cases. Also the tension difference in the rings increases more. This

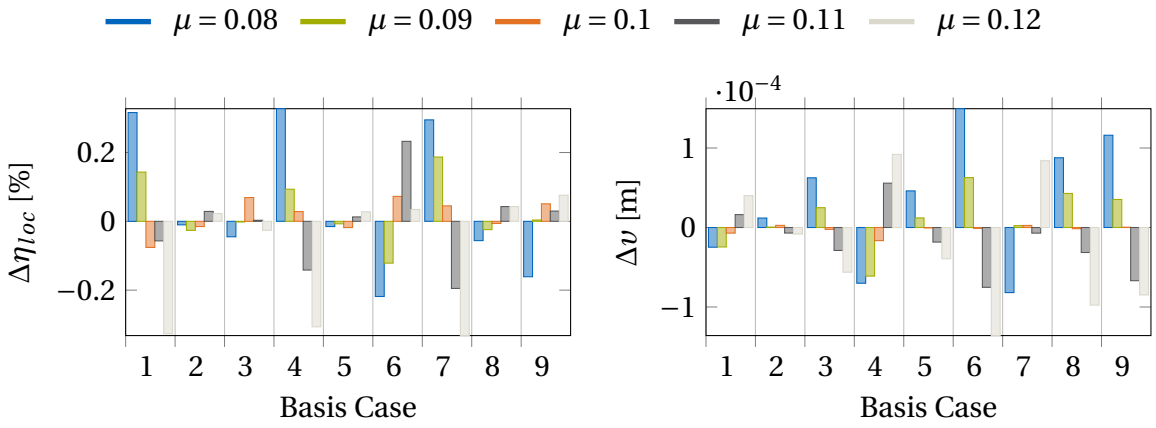

(a) Local efficiency changes

(b) Operational endplay changes

Figure 4.15: Comparison of global outputs comparing different constant Coulomb friction coefficients for the element-ring contact for the cases of Table 3.1. The average of all simulations for each case is used as reference.

results in differences in the push-forces in the push-strands which directly affects v (Figure 4.15b). For UD configurations this is beneficial in terms of efficiency. The tension difference contributes positively to the torque equilibrium. Less push-forces are build up in the active arc, which reduces the longitudinal losses in the PRI between element and sheave. In high load cases, i.e. BC06, the internal losses may reduce as this effect dominates the increased losses at the element-ring contact.
In OD a higher element-element normal force in the push-strand has to be build up in the active arc. It results in higher losses for the flank-sheave contact and consequently an overall decrease of efficiency.

Stribeck

Three different influence parameter settings have been chosen for a velocity dependent friction function, namely str_0, str_1 and str_2. They cover the technical range [76]. The respective parameter settings are depicted in Figure 4.16 and listed in Table 4.2. The TR stays constant with a maximum standard deviation of 0.02. The changes in efficiency however follow the discussion above where increasing the index i is analogue to decreasing the constant friction coefficient.

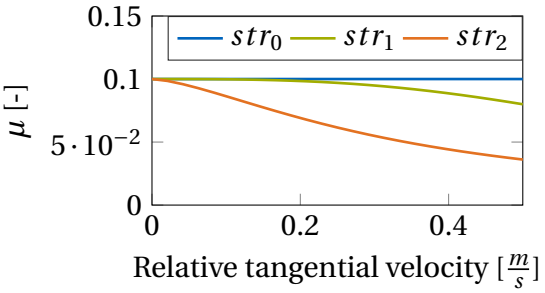

Figure 4.16: Stribeck curves

	μ_0	μ_1	μ_2	k
str_0	0	0.1	0	0
str_1	0	0.1	2	3
str_2	0	0.1	5	1.5

Table 4.2: Stribeck parameters

5 Validation

Every model is an approximation of the reality. Observations are written in mathematical formulas covering the main effects. Numerical calculations, i.e. the simulations, compute these formulas only up to a certain accuracy. A post-processing step calculates interpretable quantities out of the simulation results.
The range of uncertainty is discussed in the previous chapters as not all parameters are known. It is therefore important to assess the following results together with the discussion in Chapters 3 and 4. In this chapter results of the present model are compared to measurements. It shows the range of validity of the model.

Following the ideas of post-processing, the two main aspects, i.e. local and global results of the model, are compared. A qualitative overview about the local forces is discussed at first. Two further force distributions for varying boundary conditions are compared quantitatively. Besides, local kinematics, i.e. spiral running and element-sheave pitch, yield further quantitative matches.
Four different variator geometries are used to compare global values while varying the boundary conditions. Quantitative matches are gained for well identified parameters whereas parameter uncertainties only allow for qualitative discussion. Further properties of the system are discussed qualitatively. Slip-curves allow insights to the overall behavior of the system. The endplay tolerance shows the system's robustness.
Finally, dynamical, i.e. instationary, properties are investigated as well. On the one hand the scratch phenomenon is approached as NVH issue. On the other hand shifting dynamics are studied.

5.1 Local Results

Global values, i.e. descriptive numbers for specific setups, are used to optimize the CVT within the global drivetrain. They are based on the internal dynamics and with it on the local outputs of the system. KANEHARA ET. AL. did a variety of measurements for these local curves with a slowly running variator system to study the qualitative behavior [35]. These are the basis for the following qualitative validation for which the boundary conditions for the simulations are taken from [25, p.83, Table 6.1]. As the scaling stays unclear, ω_P was increased tenfold.
The plots show the same array structure as in [35, p.143-145] and are given in Figures C.2, C.4 and C.6 together with the original data in Figures C.3, C.5 and C.7 respectively. The structure along the belt is not adapted. It follows the order of Subsection 2.4.1, i.e. PRI-US-SEC-LS, whereas the reference follows LS-PRI-US-SEC.

These remarks hold for the analysis:

Pulley normal force on V-surface These are the normal forces between element flank and sheaves. One finds a good correlation between measurements and simulation. Higher forces are acting in the smaller arc and the typical peaks at the entry and the exit of each arc can be found. For high loads at $i_s \approx 2$ the intermediate peak at the TAP in the PRI is shifted a little too far to the left and for $i_s \approx 0.5$ the TAP is pronounced stronger as in the measurements. Altogether however, a good correlation is found which is also quantitatively proven in Subsection 5.1.1.

Block compression force These are the element-element normal forces. For the comparison only the forces at the RE are taken from the simulation to match it with the measurements. The influence of the external loads, i.e. the torque, is presented well as the push-strand switches with the load in UD. The partition of the forces between RE and head in this strand, i.e. the dip, is present as well in all cases (Section 4.3).

Transmitting force These are the frictional forces in longitudinal direction for the flank-sheave contact. As GEIER points out the integral over this curve has to be equal to zero for stationary cases which is not the case for the measurements. Assumingly the measurements are disturbed by the contact forces at the saddle between element and ring [25, p. 88, cond. A) and p. 92]. A good correlation is found for the trends. Increasing transmitting force for increasing loads in the SEC are correlated pointing against the applied torque. In the PRI strong oscillations with high frequency is observed for simulations in UD which is discussed below. Otherwise, the trends fit to the measurements and the qualitative discussion, i.e. the integral-condition is fulfilled.

Radial friction force These are the frictional forces in radial direction for the flank-sheave contact. The qualitative match between simulations and measurements is apparent. Especially in the big arcs the curves fit well and show the same dependency on the torques. In the small arcs the simulation shows more oscillatory behavior which is directly connected to the "Transmitting force". The direction directly depends on the spiral running. In the small radii its extend is less. Other oscillatory effects, e.g. coming from the ring dynamics, influence the output curves. Further discussion on spiral running is found in Subsection 5.1.2.

Ring traction These are the frictional forces in longitudinal direction for the element-ring contact. As stated for the "Transmitting force" the integral along the arc for these forces should be zero in stationary cases which is not the case for all measurements [25, p. 88, cond. B)]. Nevertheless, the trends are represented correctly and the integral condition is fulfilled for the simulations. Furthermore, the simulations show the same dependency on external torques, i.e. the turnaround peaks at the end of the SEC in OD and MED. The sign change between OD and UD is given as well.

Saddle normal force These are the normal forces between element and ring. They are represented very well showing the correct inner trends, e.g. decreasing and increasing along the arc in MED, as well as the peaks at the running in and out of the arcs. Furthermore, the dependency on the torque is the same as for the measurements.

	OD			UD			
	A	B	C	F	G	H	J
i_s / ω_P	0.5 / 1000RPM			2.3 / 2000RPM			
M_S	0Nm			0Nm	−110Nm	−205Nm	−345Nm
F_S	6.2kN	12kN	18kN	40kN			

Table 5.1: Boundary conditions used to validate the element axial forces

5.1.1 Forces

Element Axial Forces

As shown by CEBULLA in [9] the correct representation of the element axial forces, i.e. the flank forces projected into the axial direction, are crucial for the whole system dynamics. To not solely rely on qualitatively results, additional quantitative measurements were made available by BTT. The measurements were conducted for boundary conditions that fit to running conditions in practice. Besides clamping forces and torques also the speed ratios and angular velocities are varied. No direct measurements of the boundary conditions are available. For the simulation these values have been approximated and adapted from the measurement load definitions. The seven different cases are listed in Table 5.1.

Figure 5.1a shows the results for OD and UD. One can see that the measurements follow qualitatively the ones of [35]. The peaks for entering and exiting the small arcs are apparent as well as the peaks at the end of the large arcs. Simulations agree with the measurements qualitatively and quantitatively. However, the peaks are not as high as in the measurements especially for higher loads in the small arcs and low loads in the greater arcs. The force distributions directly result from the influence functions used in (2.34). Fourier series are used to compute the influence numbers [9, eq. (5.54)]. The coefficients are provided by BTT and result from FE analysis. Taking into account more functions would allow to represent strong local deformation changes better, which is needed to represent the higher peaks.
For low loads in UD the force level does not fit as well. It indicates that the TR is not the same for simulation and measurement. This global value depends on different unknown parameters (Chapter 4). For an overall analysis it is referred to Section 5.2.
It is pointed out that the averaging technique (Subsection 2.4.1) improves the results as well. Peaks arise in all cases which is not the case for (all) single elements [9]. Altogether, the current approach including the force law and post-processing has been proven successfully. On basis of this, further investigation are performed in the following.

Element-Element Forces

Besides the axial forces, the push-forces in between the elements have been measured in realistic settings as well. An UD configuration with $i_s \approx 1.3$ has been chosen to check also the influence of transition torque. The boundary conditions follow measurements as well as the torque ratio factor r. Results are shown in Figure 5.1b.
A qualitative and quantitative match is observed. The push-strand switches between $r = 0.15$ and $r = 0.60$ where $r = 0.30$ is close to a transition torque situation. The dip due to the force partition between head and RE is present in all cases. The force increase and decrease within the arcs is given. For $r = 0.30$ (nearly) no forces act within the strands but an increase within

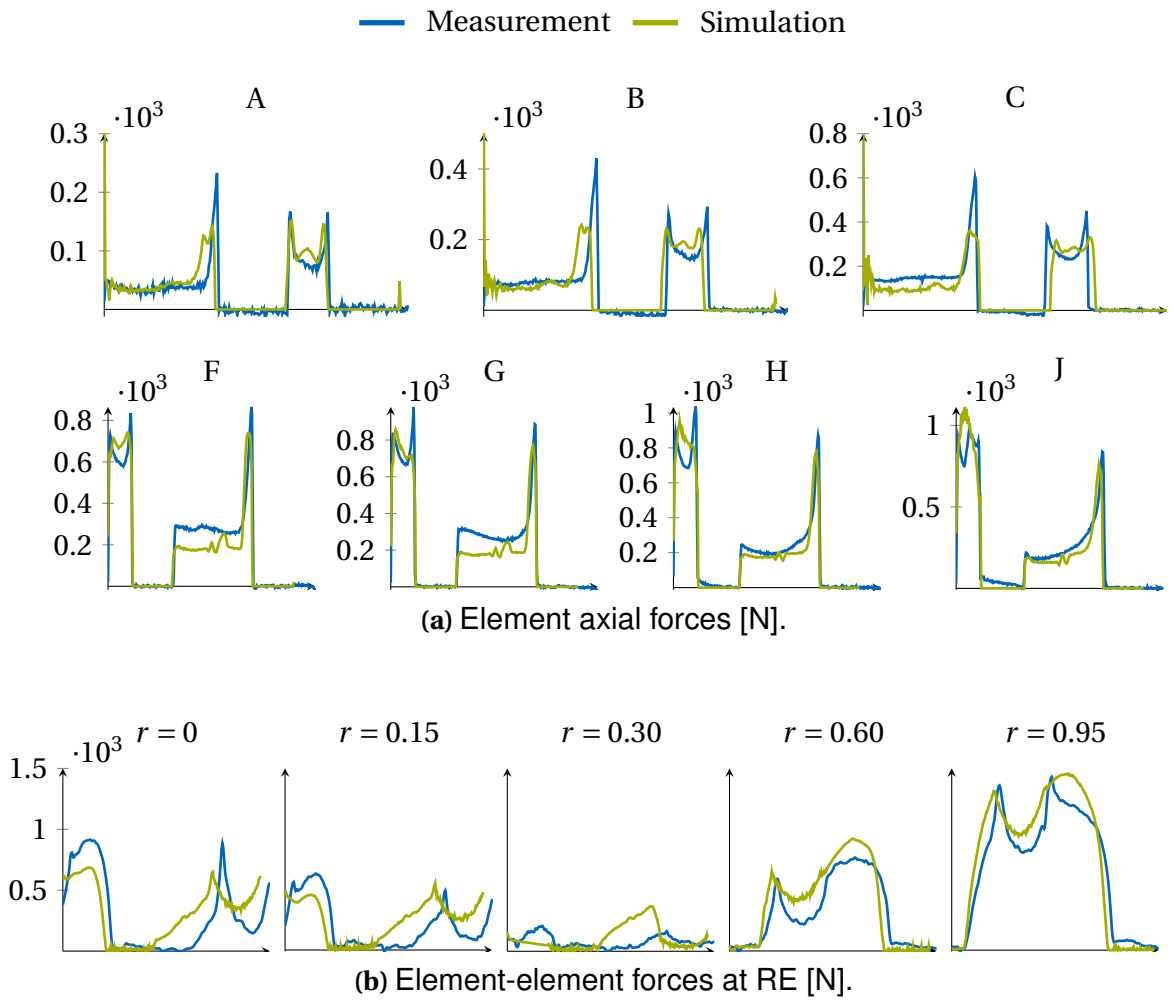

(a) Element axial forces [N].

(b) Element-element forces at RE [N].

Figure 5.1: Forces along the belt. Measurements were made available by BTT.

the PRI and SEC is observed in simulations and measurements that results from the torque equilibria in the respective arcs. Thus, it relies on correct presentation of the friction between flanks and sheaves as well as saddle and rings. Further deviation in the absolute values result from the parameter uncertainties, i.e. in particular the stiffness curves and the number of elements in reality. Parameter identification using specific measurement setups as described in Subsection 2.2.3 can help to identify the parameters.

5.1.2 Kinematics

The deformation of the sheaves and the elements define the running-in and -out of the belt into the pulley-groove. The correct representation of the forces between element and pulley directly impacts the extend of the spiral running. It leads to frictional losses in radial direction and bounds the overall torque capacity of the variator system. Its correct representation is therefore crucial within the simulation.
Quantitative measurements were conducted by BTT by measuring the upper surface of the rings. Different clamping forces and torques for varying speeds of the variator were used in 25 different cases. The boundary conditions of the simulations are given in Table 5.2. All results are depicted in Figure C.8.
For the cases of Table 5.2 also the element-sheave pitch is compared. Specific elements are

	UD1	UD2	UD3	UD4	UD5	UD6	UD7
ω_P	1000RPM			2000RPM			
M_S	0Nm	−54.3Nm	−170Nm	0Nm	−54.3Nm	−99.1Nm	−170Nm
F_S	16.435kN			16.459kN			

	UD8	UD9	UD10	UD11
ω_P	4000RPM			
M_S	0Nm	−54.3Nm	−99.1Nm	−170Nm
F_S	16.558kN			

(a) UD ($i_s \approx 2.4$)

	OD1	OD2	OD3	OD4	...	OD13	OD14
ω_P	1000RPM				...	4000RPM	
M_S	40.4Nm	26.4Nm	0Nm	−80Nm	...	0Nm	−79.6Nm
F_S	15.952kN				...	19.042kN	

	OD5	OD6	OD7	OD8	OD9	OD10	OD11	OD12
ω_P	2000RPM							
M_S	43.4Nm	34.4Nm	28.3Nm	20.8Nm	0Nm	−28.3Nm	−56.5Nm	−79.6Nm
F_S	16.57kN							

(b) OD ($i_s \approx 0.5$)

Table 5.2: Boundary conditions used to validate the arc kinematics

used in measurements with three marked points on the head. A device that is attached at a certain radius measures the position of the three points along the arc. The radial direction v_1 (Figure 2.20) is defined due to the device. Triangulation gains the orientation, i.e. the local longitudinal, radial and axial direction, of the element. With (2.50) the value for ψ follows. The comparison between measurement and simulation outputs is presented in Figure C.9. Both local kinematical outputs are discussed in the following.

Spiral Running

The spiral running in the large arcs is at least one order of magnitude greater as in the small arcs in measurement and simulation. A long running-in of the belt into the pulley-groove follows a turnaround, i.e. the minimum point, and a short running-out. An overall scaling can be seen with negative torques M_S for simulation and measurements. The spiral running increases with the torques, whereas positive torques M_S do not increase the extend of the spiral running.
In UD and for low loads the turnaround span is longer, i.e. the minimum is wide. In simulations not the minimum is affected, but a short area before is more shallow, i.e. the running-in is reduced (UD1,2,4,5,8,9). For higher torques the differences vanish.
In the small arcs the curves agree very well. The spiral running is reduced as the sheaves are stiffer at the center. Furthermore, a stiffer numerical behavior results, i.e. oscillations in the forces, as discussed above. In the simulations a short running-out at the beginning can

be observed which is not apparent in the measurements. In the strands the contact forces between element and rings are small. They increase in this short part suddenly which leads to an running-out of the element as it penetrates the rings. In measurements this change is not detected as the smooth surface of the rings is measured.
In OD this difference at the beginning of the small arc, i.e. the PRI, is observed as well. Overall, in case of small or positive torques M_S, the curves for simulations and measurements coincide very well in both arcs. The spiral running deviates for high negative torques M_S and higher speeds, i.e. OD4, OD11-OD14. Parameter uncertainties especially in c_{ax} and the Fourier coefficients (Subsection 2.2.2) lead to the deviations.

Element-Sheave Pitch

It is not clear where the contact between element and pulley-sheave closes, i.e. where the transition between strand and arc is. Therefore, the pitch angle of the element is measured in the inner parts of the arcs only. The simulation directly detects this position due to the contact forces. These forces impact the dynamic equilibrium which also lead to kinematical changes. The model suggests a sudden pitch change of the element which cannot be matched with the measurements as the data is missing.
Within the arcs, measurement and simulation show only small deviations from a constant value. This average value is denoted as to be $\psi^{m/s}_{PRI/SEC}$ depending on the arc for measurements (m) and simulations (s).

A shift s_ψ between ψ^m and ψ^s is observed for both arcs respectively, i.e. $\psi^m_{PRI} - \psi^s_{PRI} = s_{\psi,PRI}$ and $\psi^m_{SEC} - \psi^s_{SEC} = s_{\psi,SEC}$. The measurements yield a $\psi^m \approx 0°$ in all UD configurations and $\psi^m > 0$ for OD. The simulations yield only negative values, i.e. $\psi^s < 0$.
The radial reference vector v_1 (Figure 2.20) is defined by the COG-position of the element in the simulations. The device's position is used in the measurements. As these positions are not collinear with the sheave center a shift results.

The gap between the two arcs in the simulation is not observed in the measurements, i.e. $\psi^s_{PRI} - \psi^s_{SEC} \neq \psi^m_{PRI} - \psi^m_{SEC}$. This cannot be explained with the theory above, i.e. that the position of the element's COG is not collinear with the device position and the sheave center. A possible flaw in modeling and parameter uncertainties are assumed to be the reason.
The contact force actually results from a pressure distribution along the flank-area. Therefore, a relative change of the element's pitch induces torques for this contact which are transmitted between flank and pulley. This is a flaw in the present model and should be considered in the future. Smaller relative pitch angles are expected due to this frictional based torque as it is opposed to the relative movement. Besides, ψ is sensitive to different uncertain parameters, e.g. the element-element longitudinal stiffness, the number of elements in simulation and reality, the head geometry and the element-flank contact position.

Yet, the qualitative behavior is correct. For UD the level of the constant part in the PRI is below the one in the SEC. For OD it is vice versa. This can be explained by the different direction of the saddle-ring frictional forces which point in inverse direction for OD and UD. Exemplary, the UD configuration is discussed. The force in the PRI points in negative longitudinal direction. It tends to pitch in negative direction around the RE contact position. In the SEC the force points in positive longitudinal direction leading to a positive pitching. Therefore, $\psi_{SEC} > \psi_{PRI}$ in UD which is confirmed by the simulations and the measurements.

	VAR_{REF}	VAR_A	VAR_B	VAR_C
Center distance [mm]	155	173	173	173
Element width [mm]	24	28	24	24
Element thickness [mm]	1.5	1.8	1.5	1.5
Ring layers	9	12	12	12
Sheaves	flat	flat	flat	curved
Number of Boundary Conditions	85	42	30	30

Table 5.3: Variator setups for global validation

5.2 Global Results

The previous section presents qualitative and quantitative matches between simulations and measurements. Small deviations in the forces and higher deviations in the local kinematics, i.e. especially for the pitch angle of the elements in the arcs, are presented comparing the absolute numbers. In the following, global results from the simulations are compared to measurements showing quantitative matches and qualitative trends.[1]
At first four different variator setups are studied wrt. thrust ratio and efficiency trends varying speed ratio, applied torque and angular velocity. Besides these two scalar measures, slip-curves are used to compare the dependency on the applied torque. The endplay tolerance shows the system's behavior when less elements are used in reality, i.e. a robustness against for example wear.

5.2.1 Thrust Ratio and Efficiency

Two typical measures to assess the state of a variator are the thrust ratio i_F and the efficiency, i.e. the losses. BTT made available measurements of the four different variator setups of Table 5.3. Thereby, the reference setup is VAR_{REF}. The parameters of VAR_{REF} have been updated based on experience such that the simulations yield the best results. The other three variator setups show the quality of the model for unknown parameters to emphasize the necessity of further parameter investigations. The curved sheaves of VAR_C use the polynomial description of Subsection 2.2.2. The corresponding flanks of the elements are represented by a sphere.
Boundary conditions are varied wrt. to speed ratio, applied torque, the angular velocity and the safety yielding different global values. Different numbers of cases result which are listed in Table 5.3 as well. The resulting trends in the measurements are compared in the following to the ones of the simulations.

Reference Setup

The discussion in Chapters 3 and 4 as well as in Section 5.1 are yielded with the reference setup VAR_{REF}. The unknown parameters could be updated due to this knowledge. Therefore, the following validation shows the quality of the model that is achievable with good identified parameters.

[1]The support of the student workers Martin Schweizer and Christoph Drexler for the following analysis is highly acknowledged.

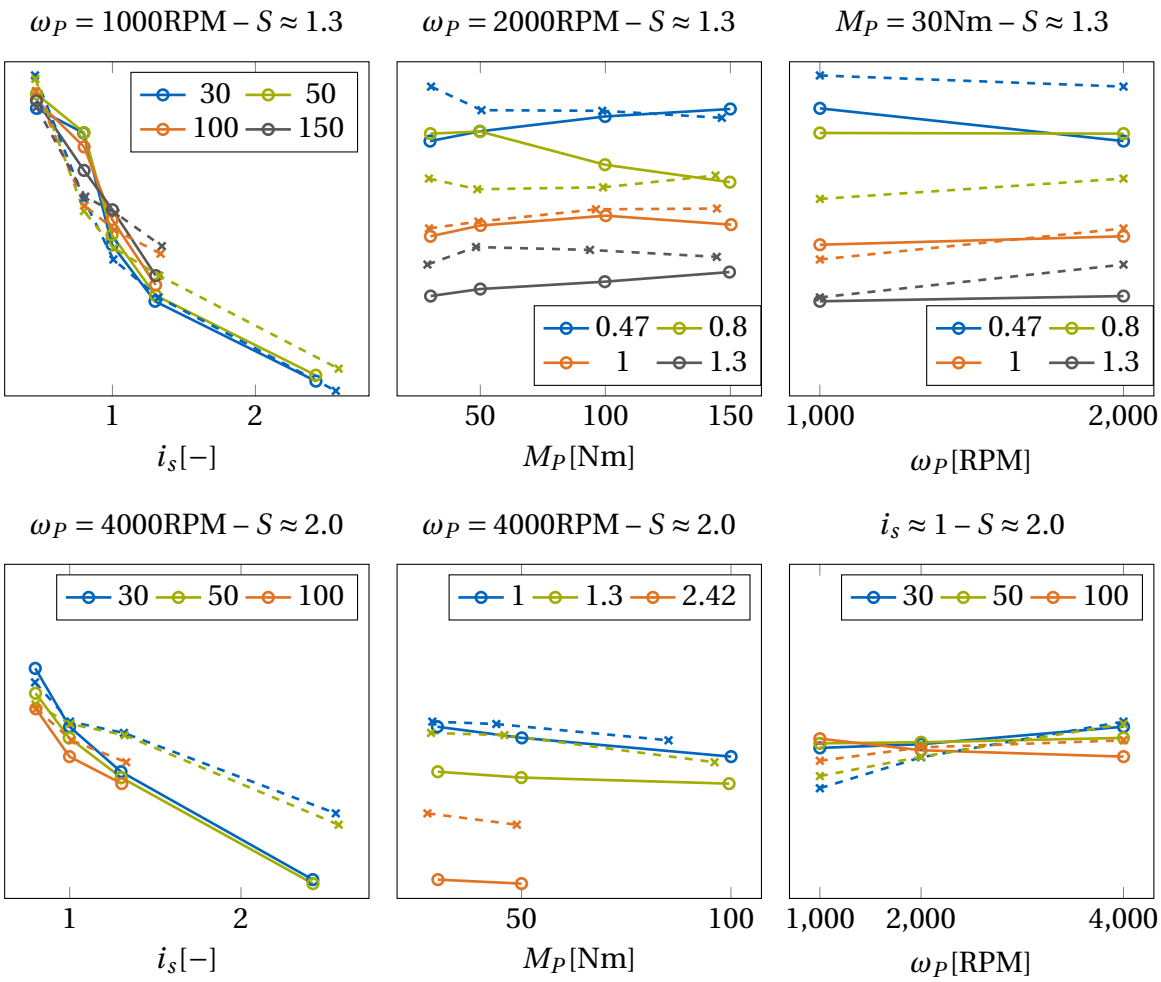

Figure 5.2: Thrust ratio validation. Comparing measurement data (solid lines) with simulation data (dashed lines). The upper row shows the case with $S \approx 1.3$ and the bottom row with $S \approx 2.0$. On the left column i_F is given wrt. i_s for different M_P at a fixed ω_P. In the center columns i_F is plotted wrt. M_P for different i_s with a fixed ω_P. At the right column i_F is presented wrt. ω_P where in the upper plot i_s is varied and in the lower plot M_P. All plots are scaled between $i_F = 0.9$ and $i_F = 1.8$. Measurements were made available by BTT.

Figure 5.2 compares values of i_F for varying boundary conditions between measurements (solid lines) against simulations (dashed lines). It is out of scope to depict all trends but a broad spectrum is given. It can be seen that all trends are covered qualitatively. The influences of i_s (left column), torque (center column) and angular velocity (right column) are included. The TR overall decreases with i_s. It is slightly too high in the simulations for extreme ratios, whereas for an approximate MED ratio it is not the case. For $i_s \approx 0.8$ the TR is too low in the simulations. Yet, for increasing primary torque the differences vanish. For the other ratios an increase with M_P is observed which coincides with the measurements. Simulations and measurements show only minor dependency on the angular velocity. The TR increases with ω_P slightly in both cases.

Furthermore, the losses are investigated for VAR_{REF}. Exemplary graphs are given in Figure 5.3, where measurements are presented with solid lines and simulations with dashed ones. For the measurements only overall values exist, i.e. η_m. Thereby, losses are included that are not represented in the simulations (Section 2.4). In the upper left corner a comparison between

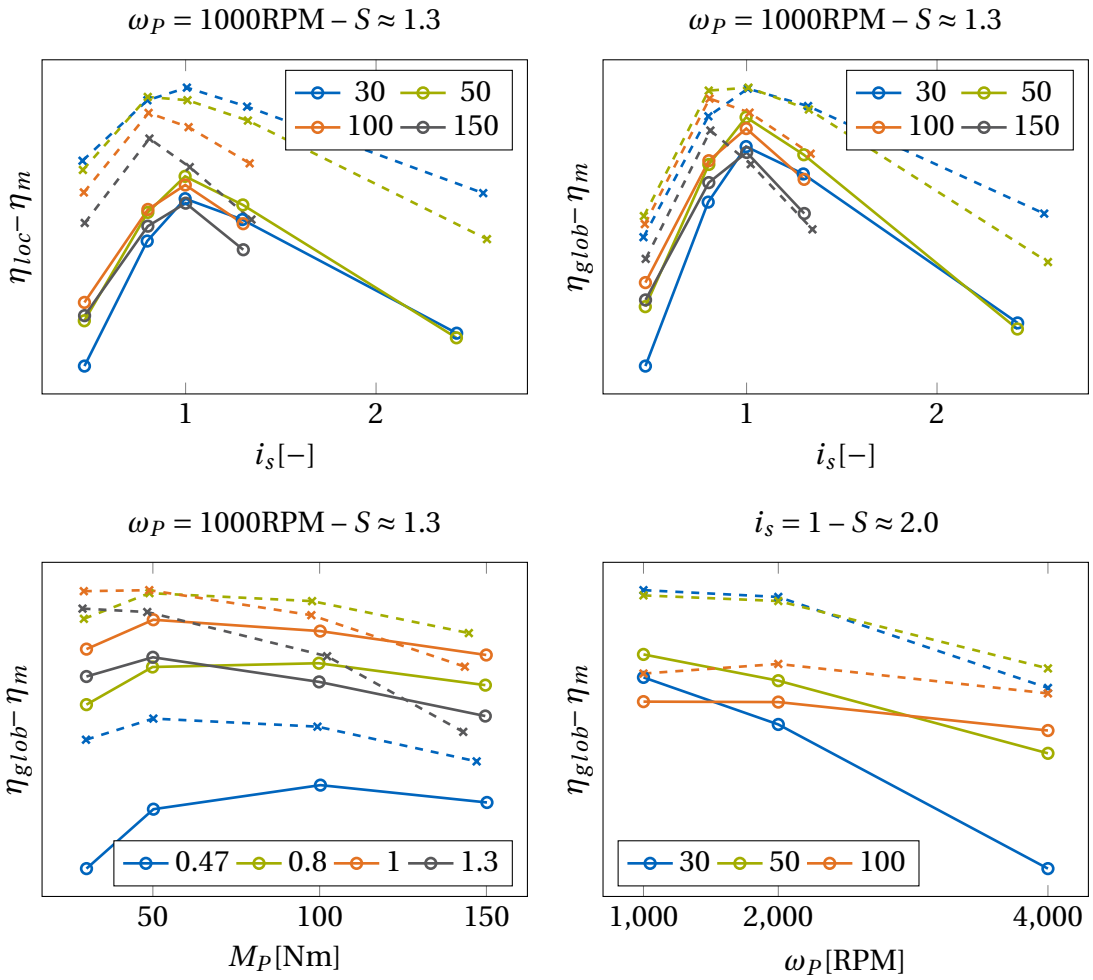

Figure 5.3: Efficiency validation. Comparing measurement data (solid lines – η_m) with simulation data (dashed lines – η_{loc}/η_{glob}). The first row shows the comparison between η_{loc} (left) and η_{glob} (right) compared to measurements. The second row validates the model concerning the influence on primary torque for varying i_s (left) and primary speed for varying M_P (right). Measurements were made available by BTT.

η_{loc} and η_m is given. It is evident that the trends are presented well by η_{loc}. In the upper right plot η_{glob} is given instead of η_{loc}. The values compare well in number with the measurements. The trends along all curves are the same.
The lower row presents the efficiency plotted against M_P (left) and ω_P (right). In both cases the trends are presented very well, i.e. the efficiency finds a maximum value for a certain torque. For increasing ratio the torque for the maximum efficiency decreases.
Increasing the belt speed, i.e. ω_P, leads to less efficiency for both – the simulation and measurement results. As the absolute belt speed increases so do the relative velocities. Resulting from increased inertia forces in the arcs, the normal contact forces and therefore the frictional forces do increase as well. Higher losses result.

Altogether it is concluded that an updated model, i.e. with well identified parameters, yields precise results. More importantly the trends for different boundary conditions are included which make the presented approach suitable for design optimization. Nevertheless, it is important to identify the parameters correctly which is emphasized in the following.

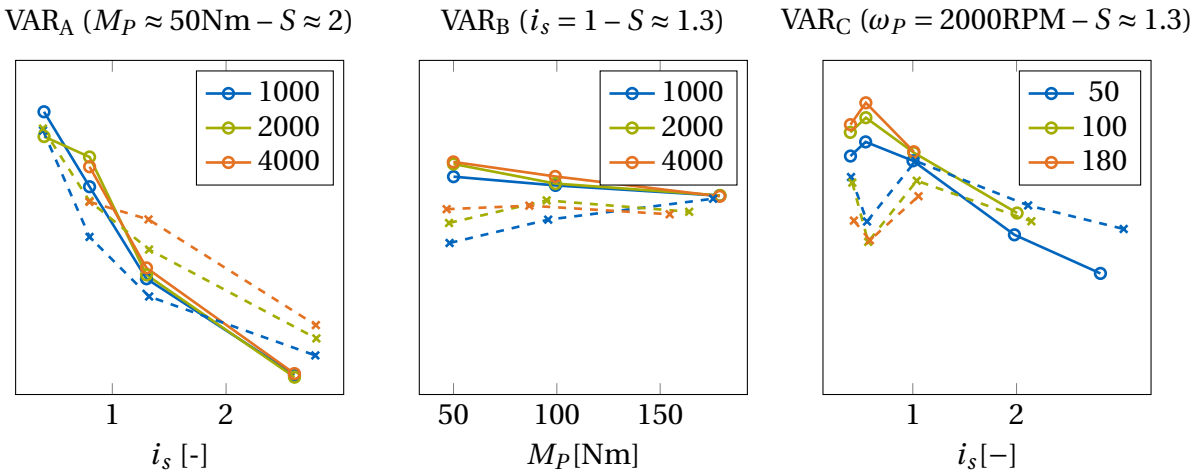

Figure 5.4: Thrust ratio comparison for different variator setups and varying load cases. For the left and center graphs, ω_P is varied in RPM. For the right graph M_P is varied in Nm. All plots are scaled between $i_F = 0.9$ and $i_F = 1.8$. Measurements were made available by BTT.

Additional Setups

Figure 5.4 shows comparisons between measurement and simulation for the additional setups. It is remarked, that these are examples. The following discussion holds not only for the respective case but for all three setups.
The overall trends are correct in the simulations but the deviations to the measurements get higher compared to the results gained with VAR$_{\text{REF}}$. Some trends deviate qualitatively. For example, the influence on ω_P for VAR$_B$ inverts wrt. the measurements. The element-element stiffness parameters, the flank contact point etc. could not be updated with local measurements. This updating process is necessary to gain as precise results as for VAR$_{\text{REF}}$.

The mismatch between simulations and measurements reflect not only in i_F. The applied boundary conditions lead also to different values of i_s or M_P. These differences trigger a change of i_F naturally as it depends on these values. To quantify these changes standard deviations σ_* of the ratio between simulation value (v_*^s) and measurement values (v_*^m) are used, e.g. $\sigma_{i_F} = \frac{i_F^m}{i_F^s}$. The results are given in Table 5.4. Again the previous discussion is confirmed. For VAR$_{\text{REF}}$ the standard deviations are small indicating a good match to the measurements. The additional setups still yield small but higher values for σ. For an automatic updating process this measure is suggested for future works.

5.2.2 Further Aspects

Slip-Curves

Other global measures to test the belt system are slip-curves [46]. For a certain geometric ratio the torque is increased continuously such that more and more slip occurs. For the case of no torque at the SEC the speed ratio is taken as reference i_s^r. The measure for slip is then defined as

$$s = \frac{i_s - i_s^r}{i_s^r} \tag{5.1}$$

	VAR_{REF}	VAR_A	VAR_B	VAR_C
σ_{i_s}	0.022	0.034	0.021	0.024
σ_{i_F}	0.068	0.091	0.085	0.096
σ_{M_P}	0.033	0.039	0.037	0.070

Table 5.4: Standard deviations for the different variator setups

where i_s measures the speed ratio at the current torque level. A typical result from measurements for an UD configuration is shown in Figure 5.5a. The primary torque is increased continuously and the speed ratio is recorded. The slip-curve includes different data about the special belt setup resulting from all parameters. At "A" the transition torque is apparent, i.e. the push-strand switches from LS to US. The height of this step again depends on different parameters, e.g. endplay or friction. Around "B" the breakaway happens, i.e. the switch from micro- to macro slip. Besides these specific points the increase of the slip due to increase of the torque is a further measure that depends on the parameters.
Internal belt oscillations yield a broad band of measurement points. The average values of these points are identified as the final slip-curve. This approach, i.e. to continuously increase M_P, cannot be used efficiently in simulations. The CPU times are too high for a continuous increase of the load combined with a quasi-stationary behavior. The internal oscillations dominate the results. Only discrete points can be gained from simulations. These are deterministic, i.e. one value results for one load. The simulation results are also expected to oscillate around an actual average value which cannot be generated efficiently.

The slip-curve of Figure 5.5a is compared to simulation results in Figure 5.5b. The slip-step, i.e. a transition between LS and US as push-strand, is apparent. This coincides with the results gained in Subsection 5.1.1. The transition torque at "A" matches furthermore between simulation and measurement very well.[2] The slip increases more in the simulations before the slip-step but matches well after "A".
In Section 4.1 the parameter of real elements in the belt N_{E0} was identified as an unknown but sensitive parameter to the simulation. This is confirmed for the slip-curve validation. In case of an pre-stressed belt no slip-step is apparent whereas in case of too few elements the slip-step is very high. A manual adjustment of all parameters was not successful. Besides N_{E0}, the element-ring friction, the contact height, the element's longitudinal stiffness could be identified as crucial parameters.
In OD the ring-tension does negatively contribute to the torque and the push-strand is always the US. Thus, the push-strand does not change the location. No slip-step is expected for $M_P > 0$. This is confirmed in Figure 5.5c. A linear increase of the slip is apparent. The slope is different again, which results from the discussed parameter uncertainties.
For the simulations also the begin of macro-slip, i.e. position "B", can be seen at the end of the curves. This confirms that the model shows qualitative good results. For quantitative matches well identified parameters are necessary.

Endplay Tolerance

Tests with the endplay difference are compared here to further quantify the simulation results. Elements are removed from the belt, i.e. the endplay increases. Otherwise, the boundary conditions are chosen to be constant. For these tests the OD configuration is used. As the

[2] Remark that i_s^t does not match fully and such a small deviation is expected.

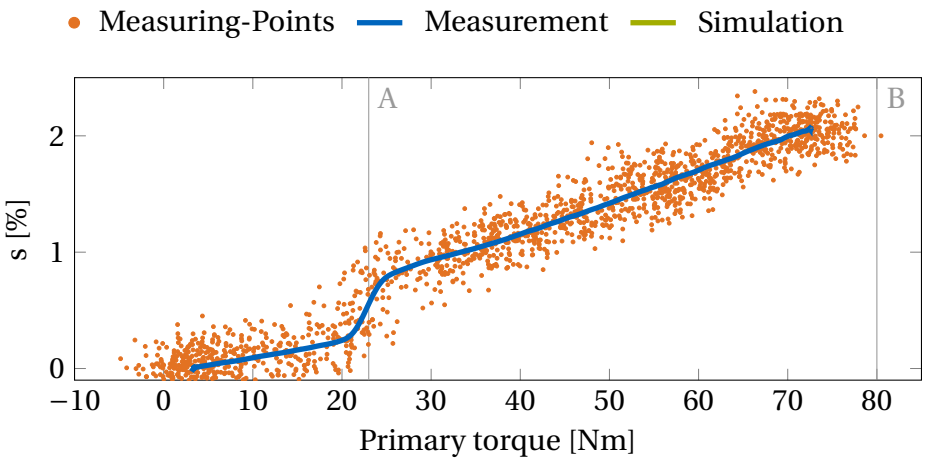

(a) Exemplary slip curve as it results from measurements. The dots symbolize the actually measurements whereas the solid line is the processed slip curve.

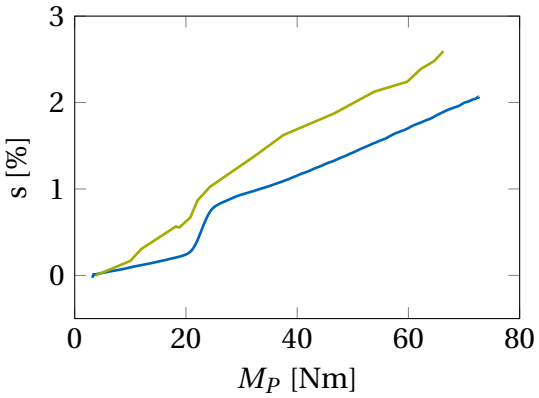

(b) $i_s \approx 2.36$ and $F_S = 16.46$kN

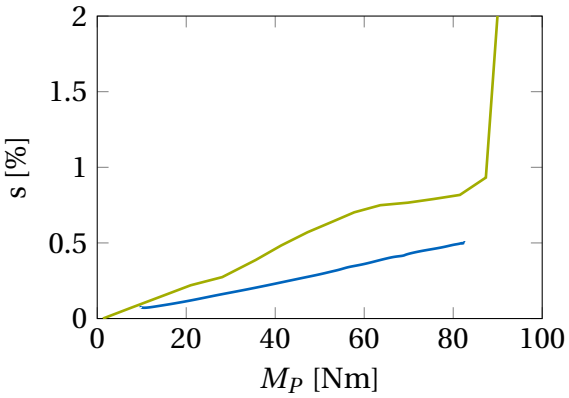

(c) $i_s \approx 0.5$ and $F_S = 5.87$kN

Figure 5.5: Slip-curves. Comparing measurement and simulation for $\omega_P = 2000$RPM. Measurement were made available by BTT.

PRI is long, the length of the active arc can change without influencing the overall system behavior. The slip increase can be studied in more detail.
Measurements are compared to simulation results in Figure 5.6a. In simulation and measurements for both speeds one can observe that the speed stays relatively constant if one (-1el) or two (-2el) are taken out of the belt. The active arc in the PRI is sufficient to build up the full push-force. The torque equilibrium, taking into account the tension forces of the rings, is fulfilled. Increasing the endplay further, i.e. removing more elements, yields that not the full push-forces can be build up anymore (Figure 5.6b). As OEP is apparent in the PRI, the slip increases. This leads to higher relative speeds between rings and elements which results in a decreased ω_S. This result – a constant zone at the beginning and a reduction of ω_S at a certain endplay – are the same for simulations and measurements. Only the qualitative discussion holds as the reference case, i.e. 0el, cannot be matched.

5.3 Instationary conditions

As stated at the beginning, the motivation for the current model is the representation of the full dynamics of pushbelt CVT systems including instationary phenomena. Two conditions

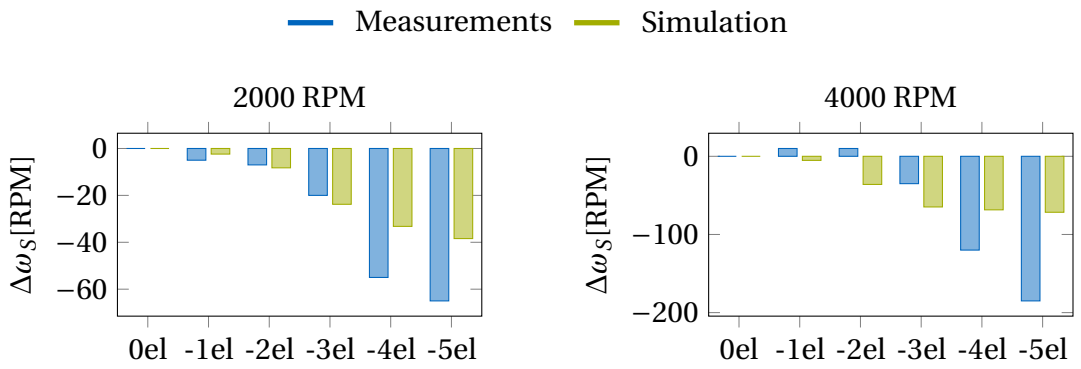

(a) Qualitative comparison of the Endplay tolerance where $\Delta\omega_S$ is plotted and 0el is the reference case. Measurement were made available by BTT.

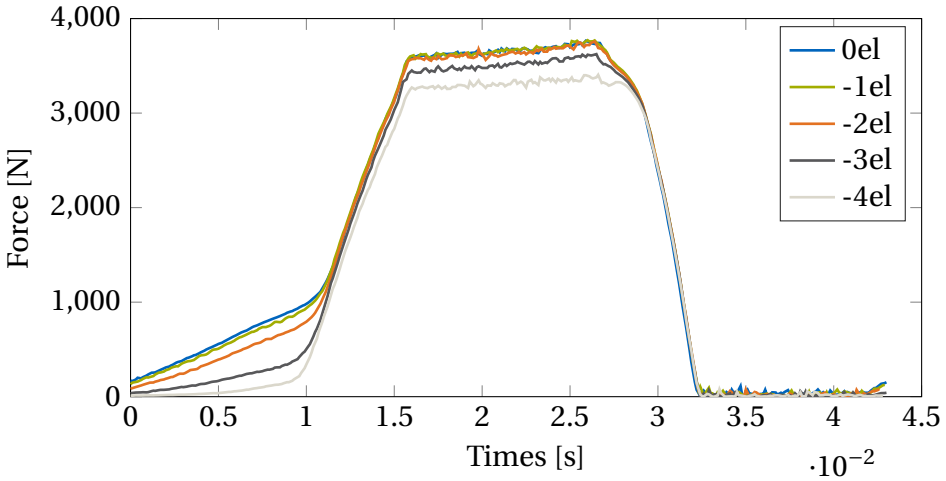

(b) Element-element normal forces for the different cases in the simulations for 2000 RPM.

Figure 5.6: Endplay Tolerance Results. Measurements were made available by BTT.

are analyzed in this section. Both show the applicability of the model for instationary cases. On the one hand the usage of Stribeck curves proves the possibility to represent "scratch". On the other hand shifting behavior is compared to literature values.

5.3.1 Scratch

PENNINGS ET. AL. study the phenomenon "scratch", i.e. gear rattle that is induced by rotational vibrations due to frictional behavior. The element-ring contact is represented with a simple model. Stick-slip is included and the friction coefficient has a negative slope for an increasing relative tangential velocity. In Subsection 4.4.2 it is mentioned that the Stribeck laws as given in Figure 4.15 did not change the overall working principle. Qualitatively the same results are gained with constant friction coefficients.
In the following, the presented model is investigated on this NVH phenomenon. Therefore, ω_P is varied between 1000RPM and 4000RPM and F_P between 0kN and 40kN. The simulations run in UD ($i_s \approx 2.5$) with $M_S = 0$Nm, i.e. the condition when scratch is experienced.
No rotational vibrations can be observed for cases of scr_0 and scr_1. The rotational speed of the SEC stays constant without a visible overlaid oscillation in all test cases. Oscillations are observed however in case of high clamping forces, i.e. $F_P = 40$kN, and when scr_2 is used.

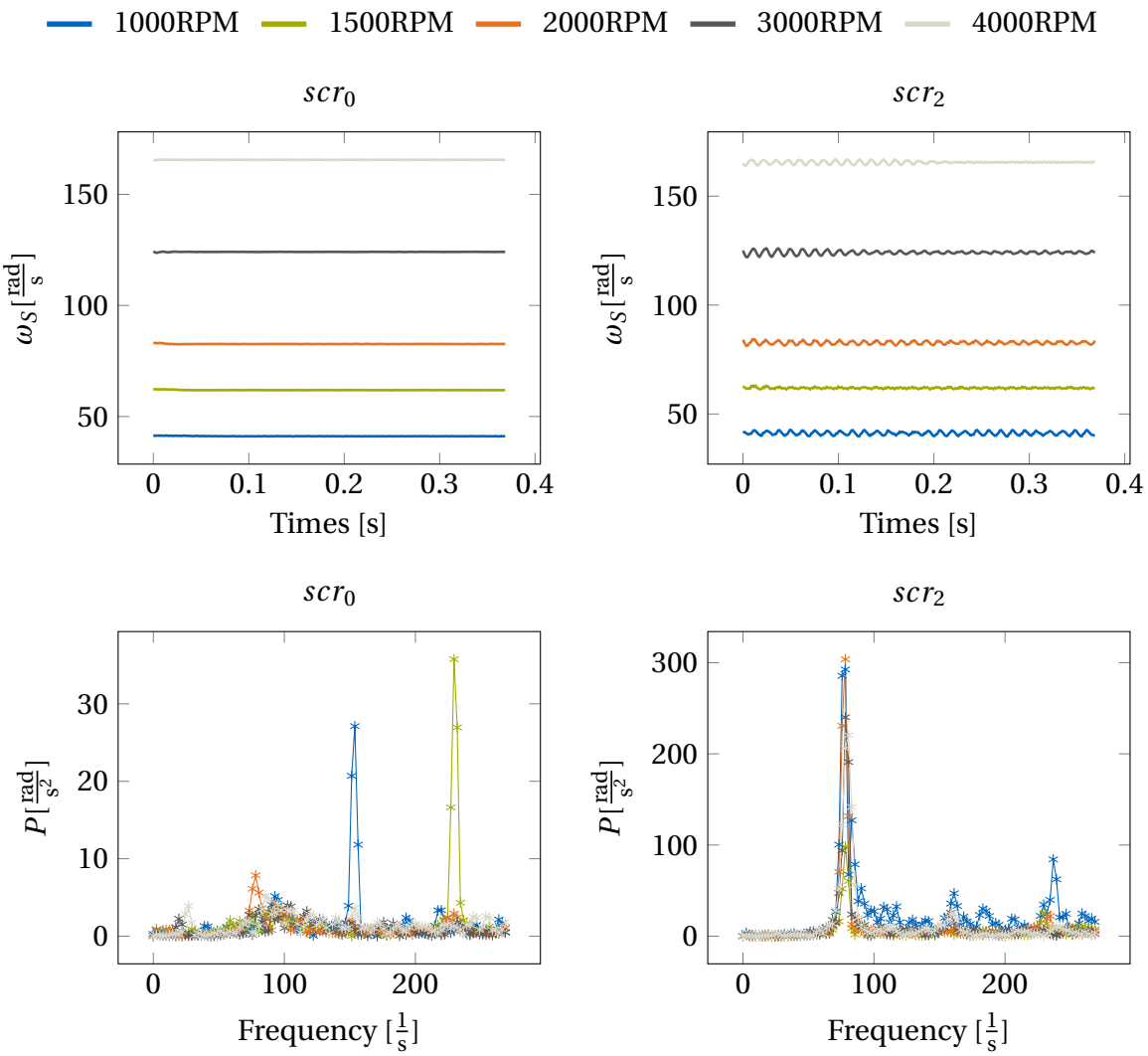

Figure 5.7: Scratch analysis for $F_S = 40\text{kN}$ and varying ω_P. The upper row shows the resulting secondary angular velocities and the lower row shows the respective FFT analysis of the derivative of ω_S.

It holds $v > 0\text{m}$ then, i.e. a loose-strand with $F_{Pu} = 0$ exists. Push-forces couple the two arcs only on one side, which is not the case for $F_P \leq 30\text{kN}$. Figure 5.7 compares the results using either scr_0 or scr_2. The first row shows the resulting ω_S varying ω_P. Besides, the fast Fourier transformation (FFT) of the derivative of ω_S, i.e. P, is presented in Figure 5.7. It is evident that rotational vibrations can be observed when scr_2 is used. The frequency is velocity independent as it is the case for measurements [76]. This is not the case when scr_0 is used as friction function. The FFT analysis shows different peaks at different frequencies with an amplitude which is one order lower than for scr_2. It is concluded that the present model enables further studies concerning the NVH phenomenon of the belt system.

5.3.2 Shifting

Finally the shifting dynamics is investigated. CARBONE ET AL. performed measurements in 2007 and with them validated the CMM model [8]. This improved the findings of [7] by respecting pulley deformation within shifting cases.
In [8] the "geometric speed ratio" $\tau = \frac{R_{DR}}{R_{DN}}$ is defined as the ratio between the primary radius

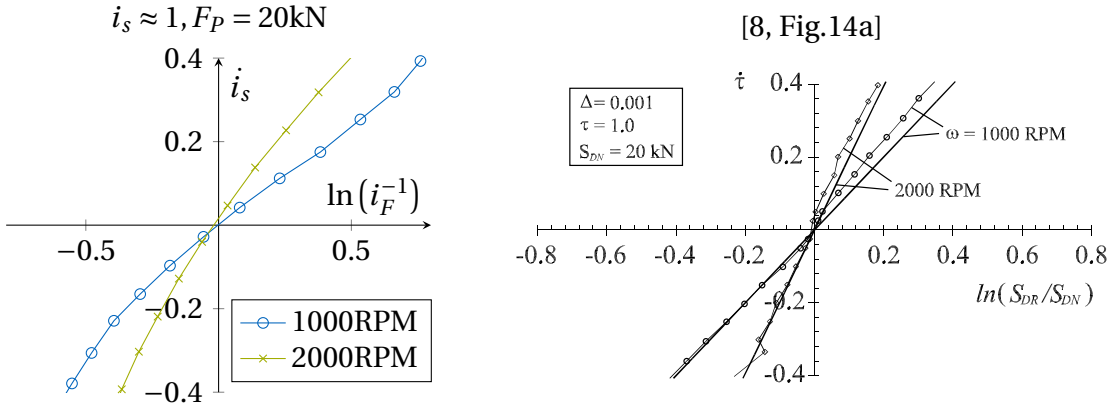

(a) Rate of change of speed ratio $\dot{i}_s$ as a function of $\ln i_F^{-1}$.

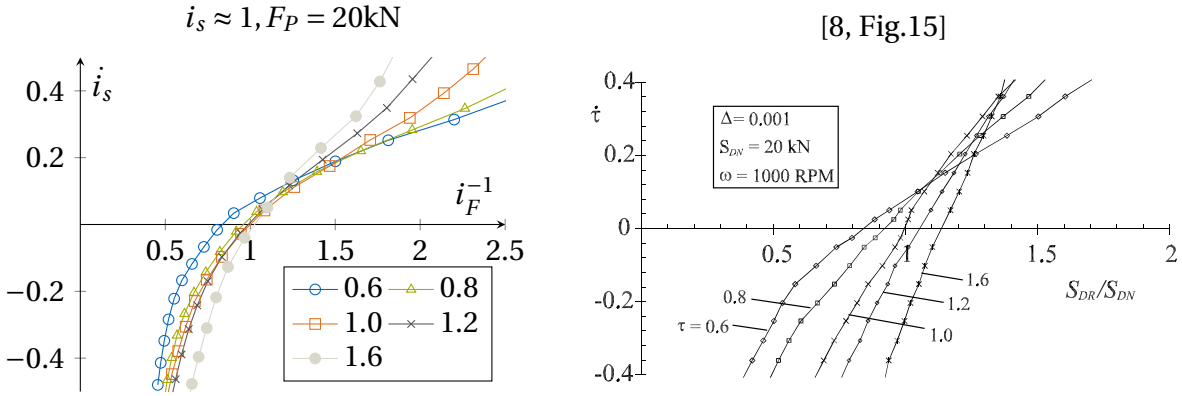

(b) Rate of change of speed ratio $\dot{i}_s$ as a function of i_F^{-1} for different basis ratios i_s.

Figure 5.8: Validation of shift dynamics. Measurements are taken from [8].

R_{DR} and R_{DN}. Its time derivative is $\dot{\tau}$. The thrusts are S_{DR} and S_{DN} for the primary and secondary pulley respectively. It is assumed, that in the plots of [8] do not show the thrust ratio $i_F = S_{DR}/S_{DN}$ but its inverse.[3] Therefore, this work uses i_F^{-1} to enable a visual comparison. As precise parameters are not available for the variator of [8], only a qualitative analysis is possible. Therefore, the setup VAR_{REF} is used as it yields the best results.

Figure 5.8a shows the influence on ω_P in the creep-mode, i.e. slow shifting velocities. On the one hand the linear dependency of $\dot{i}_s$ on the natural logarithm of i_F^{-1} is confirmed. On the other hand the slope of the line increases with the angular velocity. It is furthermore remarked that this linear relationship only holds for creep-mode. In the slip-mode the model suggests a deviation from the linear slope.

IDE ET. AL. suggests in [30] a linear relation, i.e. $\dot{i}_s \propto i_F$, whereas [8] proves that this is only valid for $i_s > 1$. Figure 5.8b validates this dependency between $\dot{i}_s$ and i_F^{-1}. For negative shift speeds i_F is greater[4] for decreasing i_s. This means a higher primary clamping force F_P is needed to shift from e.g. $i_s = 0.5$ to $i_s = 0.4$ than from $i_s = 1.6$ to $i_s = 1.5$. For the inverted case, i.e. the (high) positive shift speeds, i_F decreases with i_s. The single curves do not cross for

[3] Following [8, Fig.15] (Figure 5.8b) for $\dot{\tau} = 0$ the system is in the equilibrium, i.e. the thrust ratio S_{DR}/S_{DN} has the value of the steady state. As shown in this work and validated with measurements, it holds that $i_F > 1$ for $i_s < 1$. This is not the case for the results of [8, Fig.15]. Using the inverse, i.e. i_F^{-1}, yields reasonable results for the stationary case.

[4] i.e. i_F^{-1} is smaller

$\dot{i}_s = 0$ as for the steady state the respective i_F values differ for different speed ratios. Thus, a shift is observed to a slightly positive shift speed $\dot{i}_s > 0$ which is also represented very well for the model. Furthermore, the nonlinear relationship between $\dot{i}_s$ and i_F^{-1} is represented well by the present model which is one of the major findings in [8].

6 Conclusion

This thesis described the pushbelt CVT – its modeling and simulation. This chapter first summarizes the results and the conclusions and then describes possible avenue for future research.

6.1 Summary

Chapter 1 explains why detailed insights into the system pushbelt continuously variable transmission (CVT) are required to further improve the system. The increased driving comfort for stop-and-go traffic in modern cities and the decreased CO_2-footprint motivate this improvement. A compact overview about the phenomena within the pushbelt is given and the most important concepts to describe the system's state are introduced. The state of literature about dynamics of CVTs is presented distinguishing between stationary and shifting models. This thesis understands a pushbelt CVT as a multibody system (MBS) which enables an overall model approach including stationary and instationary states. Prior models using multibody systems which are validated and enhanced here are summarized as well. An overview about the structure and objectives of this thesis concludes the first chapter. It is emphasized, that the validation of the model is indeed an iterative process which treats the different aspects in a logical order. Yet, all chapters have to be seen in a whole to grasp the results of the work.

Modeling ideas are discussed in Chapter 2. The dynamics of the elements, sheaves and rings are discussed first. Elements and sheaves should be treated as rigid bodies considering their deformation in the interactions. The rings require a deformable model. An arbitrary Lagrangian-Eulerian (ALE) model is derived using two reference degrees of freedom (DOFs), i.e. the rings velocity and its ratio, to describe the nonlinear deformation. Overlaid deformations, which also could be incorporated only kinematical, lead to a highly adaptable and fast model.
Next interactions are discussed beginning with the element's thickness as it changes the stiffness of the element which has to be respected in the normal contact laws. Then the three contact positions are treated separately. For the element-pulley contact a new kinematical description enables arbitrary convex shaped sheaves and the coupling of both pulley-sheaves in one contact law reduces the dimension of the contact law. To respect the nonlinearity of the element's longitudinal deformation a contact law with physically interpretable parameters is introduced. The Push-Force-Tester system uses parts of the complete CVT to enable identification of these parameters which are unknown from the overall system. The contact at the element's saddle is discussed in more detail for spatial models. On the one hand the prior contact kinematics are enhanced to avoid unphysical torques around the center line of the rings. On the other hand a tracking law balances the rings and the elements in case of

misalignment respecting the normal force influence.
To reduce simulation time three numerical techniques are presented. The initialization respects the force equilibrium instead of solely the kinematics which reduces the transition phase at the beginning of every simulation. A reformulation of the linear complementarity problem that is used for the representation of the pulley-deformation with projection functions yields faster simulations in case of a compatible contact kinematics. Using algorithms for sparse matrices in combination with specific properties of the integrator reduce the time to set up the mass-action matrix in case of a non-smooth representation of contact laws.
Finally, the steps for post processing are shown. This forms the basis to yield local and global results which are compared in the subsequent chapters.

Parameter studies are performed to check the accuracy of the model. Numerical aspects are treated in Chapter 3. The number of elements that are used to represent the real number of elements in the belt is studied first. A minimal number of 200 elements is needed to achieve results close to a reference of 400 elements. Set-valued contact laws resulting in non-smooth equations of motions are studied next. It is shown that for the element-ring friction it is useful to incorporate non-smooth effects. For all other cases the simulation time increases strongly and the benefit is unclear. Finally, different models for the rings are investigated. It is shown that the ALE model performs very well. The results match with a previously validated ring model but the CPU time is reduced. Robust integration in spatial situations in reasonable simulation time is only possible with the ALE model. The stiff DOFs in axial direction can be incorporated on a kinematical level which is not possible for classical models.

Physical based parameters are varied and discussed in Chapter 4 and serve as the basis for parameter identification as well as for design optimizations. The most important parameters are treated showing their main influences on the system's behavior. These are the number of elements that exist in the belt assembly, the contact position at the element's flank as well as the axial stiffness, the geometry of the element's head in terms of the contact position and the friction parameters for the contact at the flank as well as at the saddle. The complex interactions, which vary for different ratios and load conditions, are discussed qualitatively using exemplary local phenomena.

In Chapter 5 validating results are presented. A qualitative overview about the most important local measures along the belt validates the model's approach. Quantitative matches are gained comparing the element's axial forces in the arc as well as the longitudinal forces along the belt. Furthermore, kinematical behavior shows good correlation in terms of spiral running for different ratio and load cases. The pitch angle of the elements within the arcs however, only agrees qualitatively.
The thrust ratio and efficiency match quantitative for well identified parameters. Further setups lack precise parameters. Qualitative accordance results. Slip-curve experiments fit their virtual counterparts approximately, i.e. a slip-step is apparent as well as a maximum torque. Large parameter sensitivity is found with respect to the parameters discussed in Chapter 4. Similarly, the endplay tolerance shows qualitatively good correlation but the precise parametrization remains unclear.
Finally, instationary phenomena are investigated. The "scratch" phenomenon, which causes gear rattle is linked to Stribeck friction when operational endplay is apparent in the belt. For shifting cases, the time derivative of the speed ratio is in line with measurements in the literature.

6.2 Outlook

This thesis demonstrates that modeling the pushbelt CVT as a MBS is a useful approach to study the internal dynamics as a whole. Yet, it became clear that further research and development is required for a fully detailed model.
The correct identification of the system's parameters is an essential requirement to obtain correct results. As shown for the nonlinear stiffness of the elements, special measuring devices could be used to avoid a full integration of the system which involves all parametric influences.

For well identified variator models the simulations can be used for design optimization. The model's broad field of design parameters leaves room for more influence studies beyond those performed for the validation within this thesis.
The element-sheave pitch is one example that shows a need for it. The nonlinear push-force functions, the contact position at the element flank as well as the number of elements in the belt require more dedicated identification. Similarly to the Push-Force-Tester system, submodel testing seems to be a promising approach.
Therefore, a further reduction of simulation times is useful. Parallel as well as implicit integration schemes that focus on the efficient evaluation of the nonlinear contact kinematics could reduce the simulation time.
This enables the efficient treatment of the pushbelt CVT as a spatial system incorporating for example misalignment as well. The proposals for contact kinematics and ring tracking could be tested in practice. The expected influence on the force distributions along the belt could be used in post-processing to minimize for example the stresses in the elements.

Based on the ALE technique efficient models for shifting dynamics could be derived. The two reference DOFs have proven to efficiently incorporate the major effects that are apparent within the CVT. By projecting the masses of the elements onto this model, similarly to ideas presented in [6], an efficient and easily adaptable model could be derived for the application in control, i.e. drivetrain models.

A Eulerian Description for a One Dimensional Closed Continuum

In the following the transformation between the Eulerian description and the Lagrange description is shown for a one dimensional continuum. For the general case IRSCHIK and HOLL derive the equations [32]. The following derivation holds for a one dimensional closed continuum and thus is simpler to grasp.[1]

A.1 Preliminaries

The position of a particle along a curve $\bar{x}$ is described with its original position ξ and its motion along the curve $s(t)$ with

$$\bar{x} = \xi + s(t), \qquad \frac{d\bar{x}}{d\xi} = \frac{\partial \bar{x}}{\partial s} = 1, \qquad \frac{d\bar{x}}{dt} = \frac{ds}{dt} \tag{A.1}$$

where ξ is the Eulerian coordinate describing a fixed point in space and $\bar{x}$ is the Lagrangian coordinate following the particle over time.
A function f is defined as an integral over $g(\bar{x})$ with time depending limits $l = l(t), u = u(t)$.

$$f = \int_l^u g(\bar{x}, t) d\bar{x}$$

The absolute time derivative of f is given by the Leibniz integral rule.

$$\frac{\mathrm{d}f}{\mathrm{d}t} = \frac{\partial f}{\partial l}\frac{\mathrm{d}l}{\mathrm{d}t} + \frac{\partial f}{\partial u}\frac{\mathrm{d}u}{\mathrm{d}t} + \int_l^u \frac{\mathrm{d}g}{\mathrm{d}t} d\bar{x} = -g(l)\frac{\mathrm{d}l}{\mathrm{d}t} + g(u)\frac{\mathrm{d}u}{\mathrm{d}t} + \int_l^u \frac{\partial g}{\partial \bar{x}}\frac{\mathrm{d}\bar{x}}{\mathrm{d}t} d\bar{x} + \int_l^u \frac{\partial g}{\partial t} d\bar{x} \tag{A.2}$$

A.2 Direct Approach

Starting with the Lagrangian $\mathscr{L} = \mathscr{T} - \mathscr{V}$ and the standard Lagrange equation

$$\frac{\mathrm{d}}{\mathrm{d}t}\frac{\partial \mathscr{L}}{\partial \dot{q}_k} - \frac{\partial \mathscr{L}}{\partial q_k} = 0$$

a direct method to get the EOMs can be derived. With the kinetic energy

$$\mathscr{T} = \frac{1}{2}\int_\Omega v^T v \rho d\Omega = \frac{1}{2}\rho \int_\Omega v^T v d\Omega \tag{A.3}$$

[1] The derivation was done together with my co-worker Thorsten Schindler and I want to acknowledge his support and contributions [28].

where Ω is the original volume for the integration, ρ is the constant density of the material and v the current velocity field, it follows the expression for the Lagrange equation.

$$\frac{\mathrm{d}}{\mathrm{d}t}\frac{\partial \mathcal{T}}{\partial \dot{q}_k} - \frac{\partial \mathcal{T}}{\partial q_k} = Q_k \quad \text{with} \quad Q_k = -\frac{\partial \mathcal{V}}{\partial q_k} \tag{A.4}$$

For the given situation of a beam, the integral is constant in the two cross-section directions resulting in the area A. Only the integral over the length from limit l to limit u has to be calculated along the beam in direction $\bar{x}$. Inserting this into the Lagrange equation, it follows

$$\begin{aligned}\frac{\mathrm{d}}{\mathrm{d}t}\frac{\partial \mathcal{T}}{\partial \dot{q}_k} &= \frac{\mathrm{d}}{\mathrm{d}t}\frac{\partial}{\partial \dot{q}_k}\left(\frac{1}{2}\rho A\int_l^u v^T v\, d\bar{x}\right) = \frac{1}{2}\rho A\left(\frac{\mathrm{d}}{\mathrm{d}t}\int_l^u \frac{\partial (v^T v)}{\partial \dot{q}_k} d\bar{x}\right) = \frac{\rho A}{2}\frac{\mathrm{d}}{\mathrm{d}t}\int_l^u g_v\, d\bar{x} \\ &= \frac{1}{2}\rho A\left(-g_v(l)\frac{\mathrm{d}l}{\mathrm{d}t} + g_v(u)\frac{\mathrm{d}u}{\mathrm{d}t} + \int_l^u \frac{\partial g_v}{\partial \bar{x}}\frac{\mathrm{d}\bar{x}}{\mathrm{d}t} d\bar{x} + \int_l^u \frac{\partial g_v}{\partial t} d\bar{x}\right)\end{aligned} \tag{A.5}$$

Remark that the limits of the integral do not depend on the generalized velocities $\dot{q}_k$ but just on the transformation with s.

A.3 Closed Curve

For a closed curve it holds $\frac{\mathrm{d}l}{\mathrm{d}t} = \frac{\mathrm{d}u}{\mathrm{d}t}$ and $g_v(l) = g_v(u)$. Thus, the first two terms in (A.5) cancel each other. Following the fundamental theorem of calculus, the first integral of it is zero as well.

$$\int_l^u \dot{s}\frac{\partial g_v}{\partial \bar{x}} d\bar{x} = \dot{s}(g_v(u) - g_v(l)) = 0$$

A transformation of variables to integrate along ξ with $u = L + s$ and $l = 0 + s$ and the length L of the beam yields finally

$$\frac{\mathrm{d}}{\mathrm{d}t}\frac{\partial \mathcal{T}}{\partial \dot{q}_k} = \frac{1}{2}\rho A\int_0^L \frac{\partial g_v}{\partial t} d\xi \tag{A.6}$$

where the relative[2] time derivative is needed.
Using the same ideas, the derivative of the kinetic energy wrt.. the generalized positions follows.

$$\frac{\partial \mathcal{T}}{\partial q_k} = \frac{1}{2}\rho A\frac{\partial}{\partial q_k}\int_l^u v^T v\, d\bar{x} = \frac{\rho A}{2}\int_0^L \frac{\partial v^T v}{\partial q_k} d\xi$$

The potential energy can be represented as an integral over the volume $V = \int_l^u g_V\, d\bar{x}$ as well. Thus, the last term of (A.4) is defined as well.

$$\frac{\partial \mathcal{V}}{\partial q_k} = \left(-g_V(l)\frac{\partial l}{\partial q_k} + g_V(u)\frac{\partial u}{\partial q_k} + \int_l^u \frac{\partial g_V}{\partial q_k} d\bar{x}\right) = \int_0^L \frac{\partial g_V}{\partial q_k} d\xi$$

Therefore, all expression are written in Eulerian description and for this special case of a closed beam structure the transformation does not yield additional terms.

[2] The absolute time derivative is incorporated already. Only a direct time dependency is left and the relative time derivative is needed.

B Equations for the ALE Ring Model

The derivation in Subsection 2.1.2 states the most important ideas as well as the integrals that result from the derivation. For their evaluation more explicit expressions are given for completeness as it may serve future works as reference.
The single gradients of $\mathbb{P}$ are

$$\frac{\partial \mathbb{P}}{\partial s} = \frac{\partial \begin{bmatrix} r' & \frac{\mathrm{d}r}{\mathrm{d}\Theta} & \mathbb{B} \end{bmatrix}}{\partial s} = \begin{bmatrix} 0 & \dots & 0 \\ 0 & \dots & 0 \\ 0 & \dots & 0 \end{bmatrix} \tag{B.1a}$$

$$\frac{\partial \mathbb{P}}{\partial \Theta} = \frac{\partial \begin{bmatrix} r' & \frac{\mathrm{d}r}{\mathrm{d}\Theta} & \mathbb{B} \end{bmatrix}}{\partial \Theta} = \begin{bmatrix} \frac{\mathrm{d}r'}{\mathrm{d}\Theta} & \frac{\mathrm{d}^2 r}{\mathrm{d}\Theta^2} & \frac{\mathrm{d}\mathbb{B}}{\mathrm{d}\Theta} \end{bmatrix} \tag{B.1b}$$

$$\mathbb{P}_{dqfi} = \frac{\partial \mathbb{P}}{\partial q_{fi}} = \frac{\partial \begin{bmatrix} r' & \frac{\mathrm{d}r}{\mathrm{d}\Theta} & \mathbb{B} \end{bmatrix}}{\partial q_{fi}} = \begin{bmatrix} \mathbb{B}'_i & \left(\frac{\partial \mathbb{B}}{\partial \Theta}\right)_i & \begin{bmatrix} 0 & \dots \\ 0 & \dots \\ 0 & \dots \end{bmatrix} \end{bmatrix} \tag{B.1c}$$

and for the relative time derivative of $\mathbb{P}$ one yields

$$\begin{aligned} \frac{\partial \mathbb{P}}{\partial t} &= \frac{\partial \mathbb{P}}{\partial s}\dot{s} + \frac{\partial \mathbb{P}}{\partial \Theta}\dot{\Theta} + \frac{\partial \mathbb{P}}{\partial q_f}\dot{q}_f \\ &= \begin{bmatrix} 0 & \dots \\ 0 & \dots \\ 0 & \dots \end{bmatrix} + \begin{bmatrix} \frac{\mathrm{d}r'_{Ref}}{\mathrm{d}\Theta} + \frac{\mathrm{d}\mathbb{B}'}{\mathrm{d}\Theta} q_f & \frac{\mathrm{d}^2 r}{\mathrm{d}\Theta^2} & \frac{\mathrm{d}\mathbb{B}}{\mathrm{d}\Theta} \end{bmatrix} \dot{\Theta} + \sum_i \begin{bmatrix} \mathbb{B}'_i & \left(\frac{\partial \mathbb{B}}{\partial \Theta}\right)_i & \begin{bmatrix} 0 & \dots \\ 0 & \dots \\ 0 & \dots \end{bmatrix} \end{bmatrix} \dot{q}_{fi}. \end{aligned}$$

The derivative of the strain energy follows with

$$\frac{\partial}{\partial q_k}\mathcal{V}_\gamma = EA\int_0^L (r'^T t - 1)\frac{\partial}{\partial q_k}(t^T r')d\xi + \sum_{*\in n,b} GA_* \int_0^L (r'^T *)^T \frac{\partial}{\partial q_k}(*^T r')d\xi \tag{B.2a}$$

$$= EA\int_0^L (r'^T t - 1)\frac{\partial}{\partial q_k}(t^T r')d\xi \tag{B.2b}$$

$$= EA\int_0^L (\sqrt{r'^T r'} - 1)\frac{\partial}{\partial q_k}\sqrt{r'^T r'}d\xi \tag{B.2c}$$

$$= EA\int_0^L (\sqrt{r'^T r'} - 1)\frac{1}{\sqrt{r'^T r'}} r'^T \frac{\partial}{\partial q_k} r' d\xi \tag{B.2d}$$

$$= EA\int_0^L (1 - \frac{1}{\sqrt{r'^T r'}}) r'^T \begin{bmatrix} \begin{bmatrix} 0 \\ 0 \\ 0 \end{bmatrix} & \frac{\mathrm{d}r'}{\mathrm{d}\Theta} & \mathbb{B}'_1 & \dots & \mathbb{B}'_n \end{bmatrix} d\xi. \tag{B.2e}$$

To derive the simplifications for the curvature energy the following derivations of $\mathbb{A}$ are used. The reference directions have unit length.

$$\mathbb{A} = \begin{bmatrix} t_{Ref} & n_{Ref} & b_{Ref} \end{bmatrix} \tag{B.3}$$

For a planar reference curve this matrix can be written depending on one rotation angle ϕ.

$$\mathbb{A} = \begin{bmatrix} \cos\phi & \sin\phi & 0 \\ -\sin\phi & \cos\phi & 0 \\ 0 & 0 & 1 \end{bmatrix} \tag{B.4}$$

Thus, it follows for the derivatives

$$\mathbb{A}' = \begin{bmatrix} -\sin\phi & \cos\phi & 0 \\ -\cos\phi & -\sin\phi & 0 \\ 0 & 0 & 0 \end{bmatrix} = \begin{bmatrix} -n_{Ref} & t_{Ref} & 0 \end{bmatrix} \tag{B.5}$$

$$\mathbb{A}'' = \begin{bmatrix} -\cos\phi & -\sin\phi & 0 \\ \sin\phi & -\cos\phi & 0 \\ 0 & 0 & 0 \end{bmatrix} = \begin{bmatrix} -t_{Ref} & -n_{Ref} & 0 \end{bmatrix} \tag{B.6}$$

which simplifies when multiplied with the reference directions.

C Additional Plots

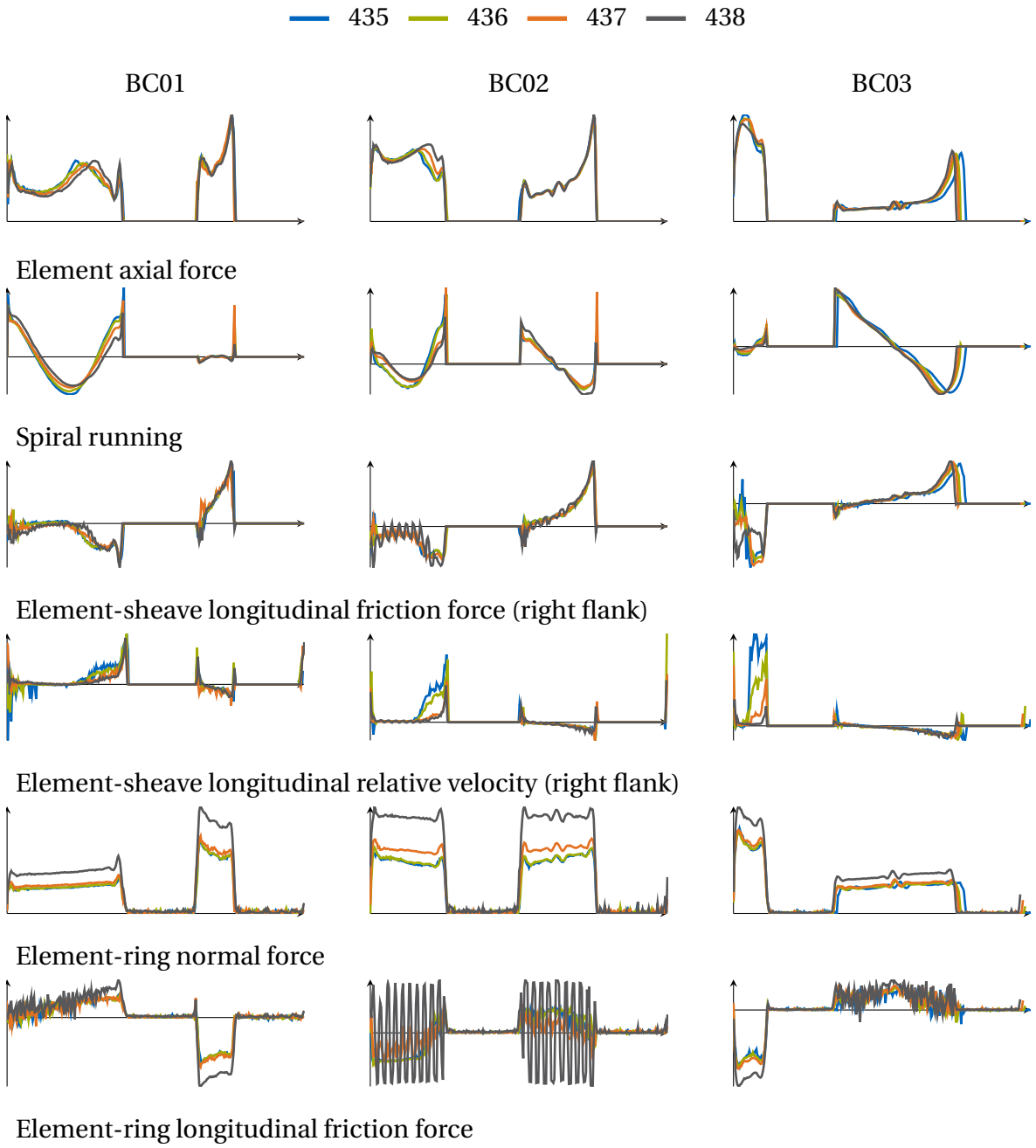

Figure C.1: Local curves for varying the number of real elements N_{E0}. Shown are the cases BC01, BC02, BC03.

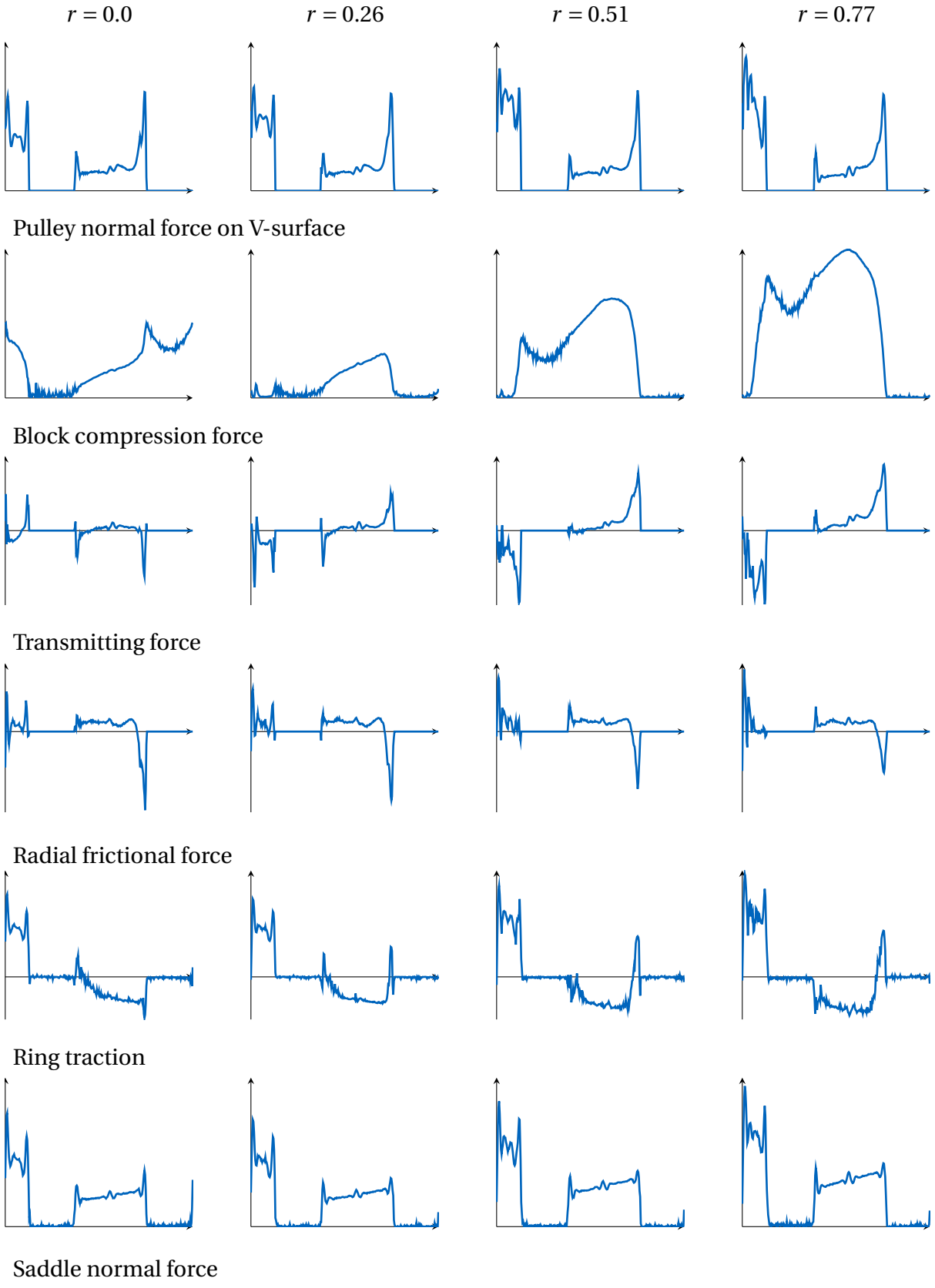

Figure C.2: Local simulation results in underdrive ($i_S \approx 2.0$) which correspond to Figure C.3

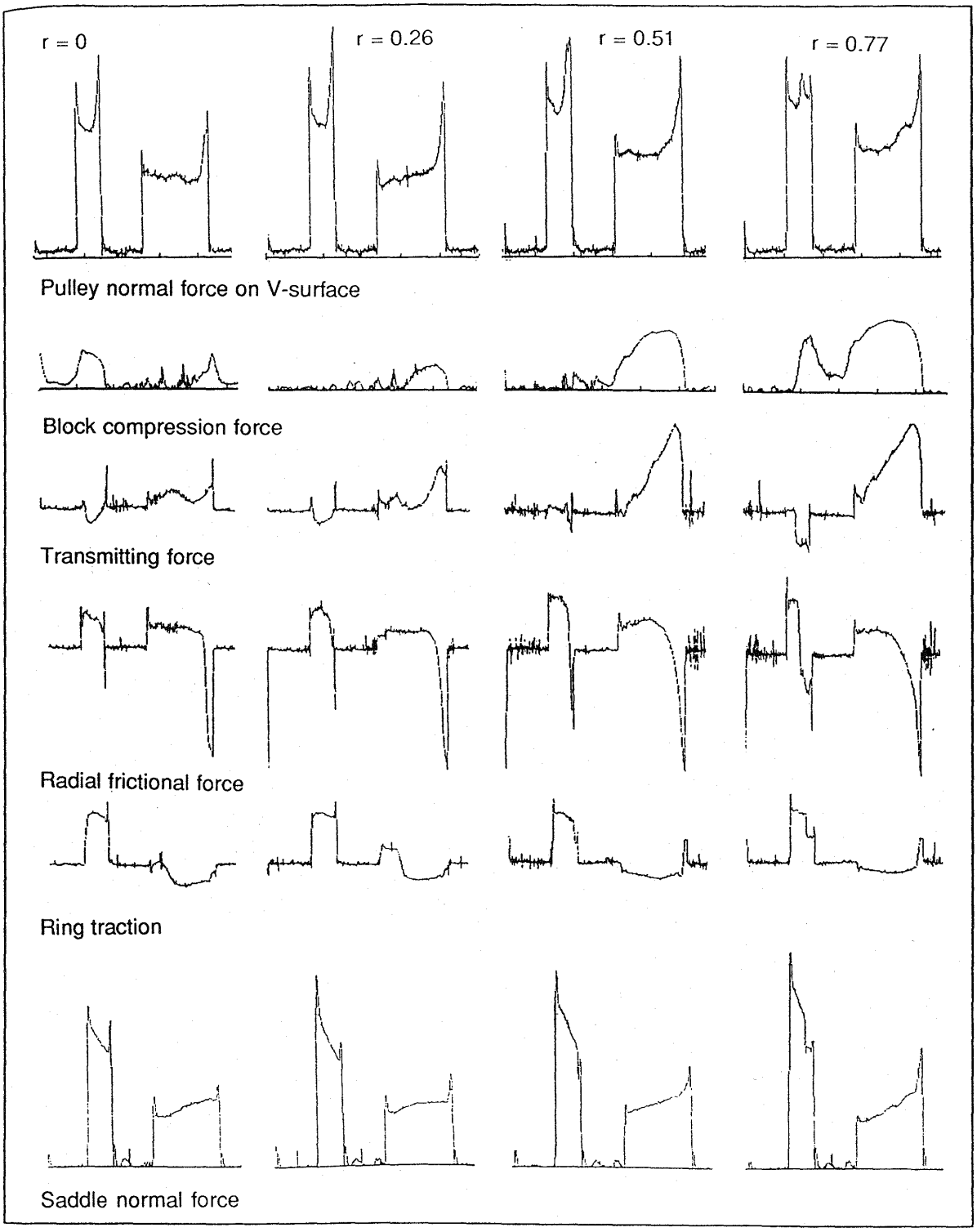

Fig.9 Distribution of the six forces acting on blocks (Speed ratio i = 2.0)

143

Figure C.3: Local measurement results in underdrive from [35, p. 143]

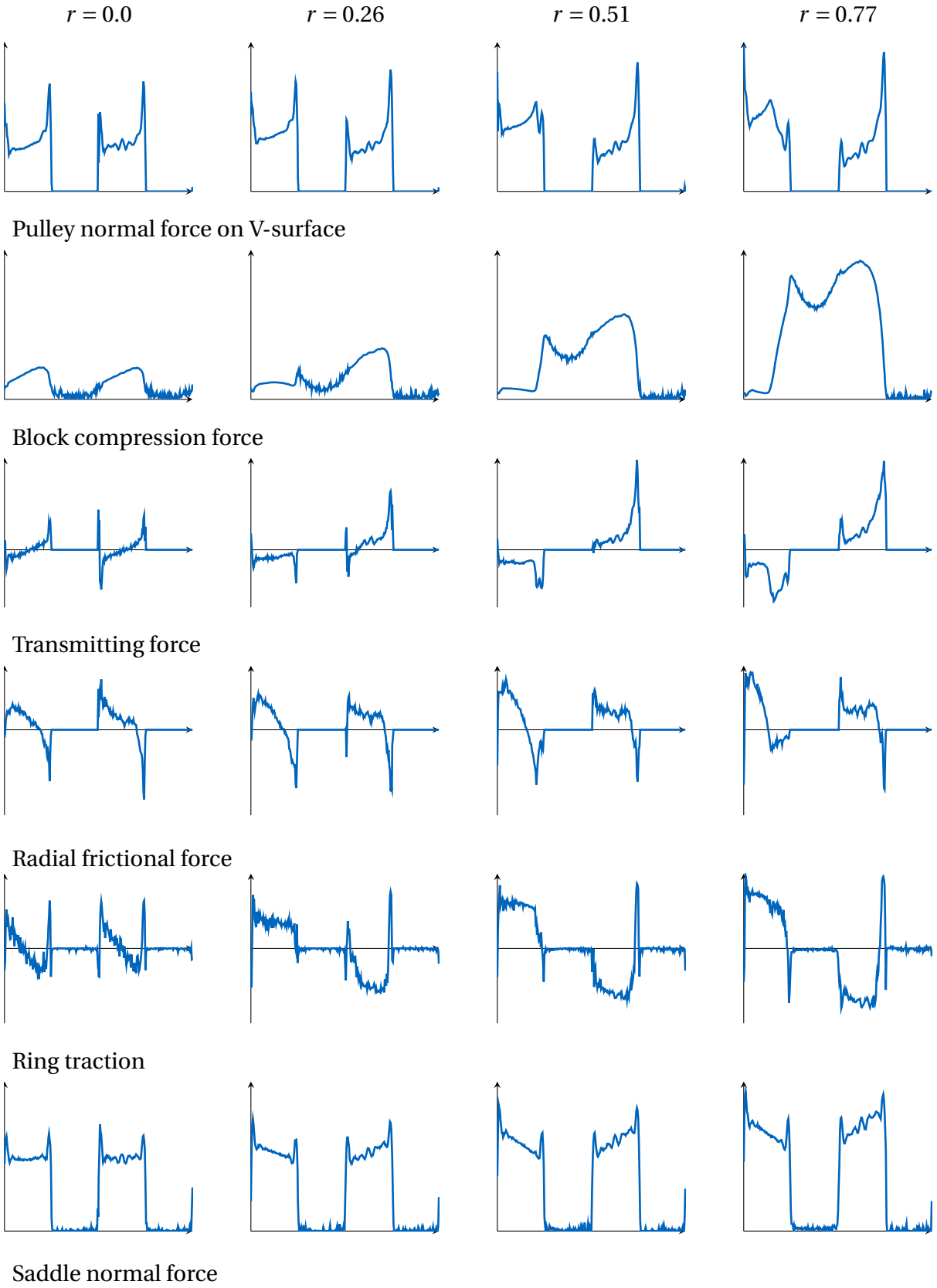

Figure C.4: Local simulation results in medium ($i_S \approx 1.0$) which correspond to Figure C.5

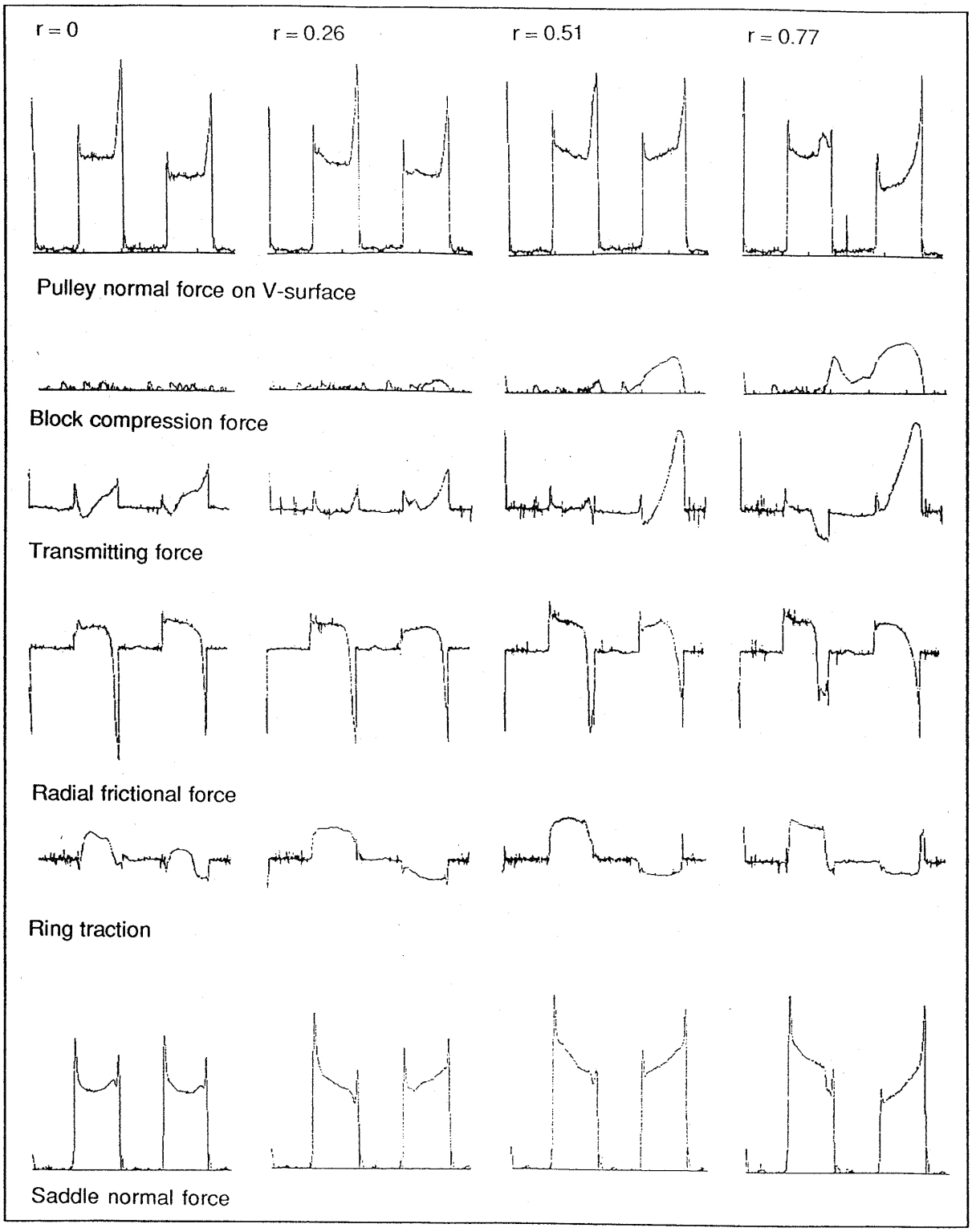

Fig.10 Distribution of the six forces acting on blocks (Speed ratio i = 1.0)

144

Figure C.5: Local measurement results in medium from [35, p. 144]

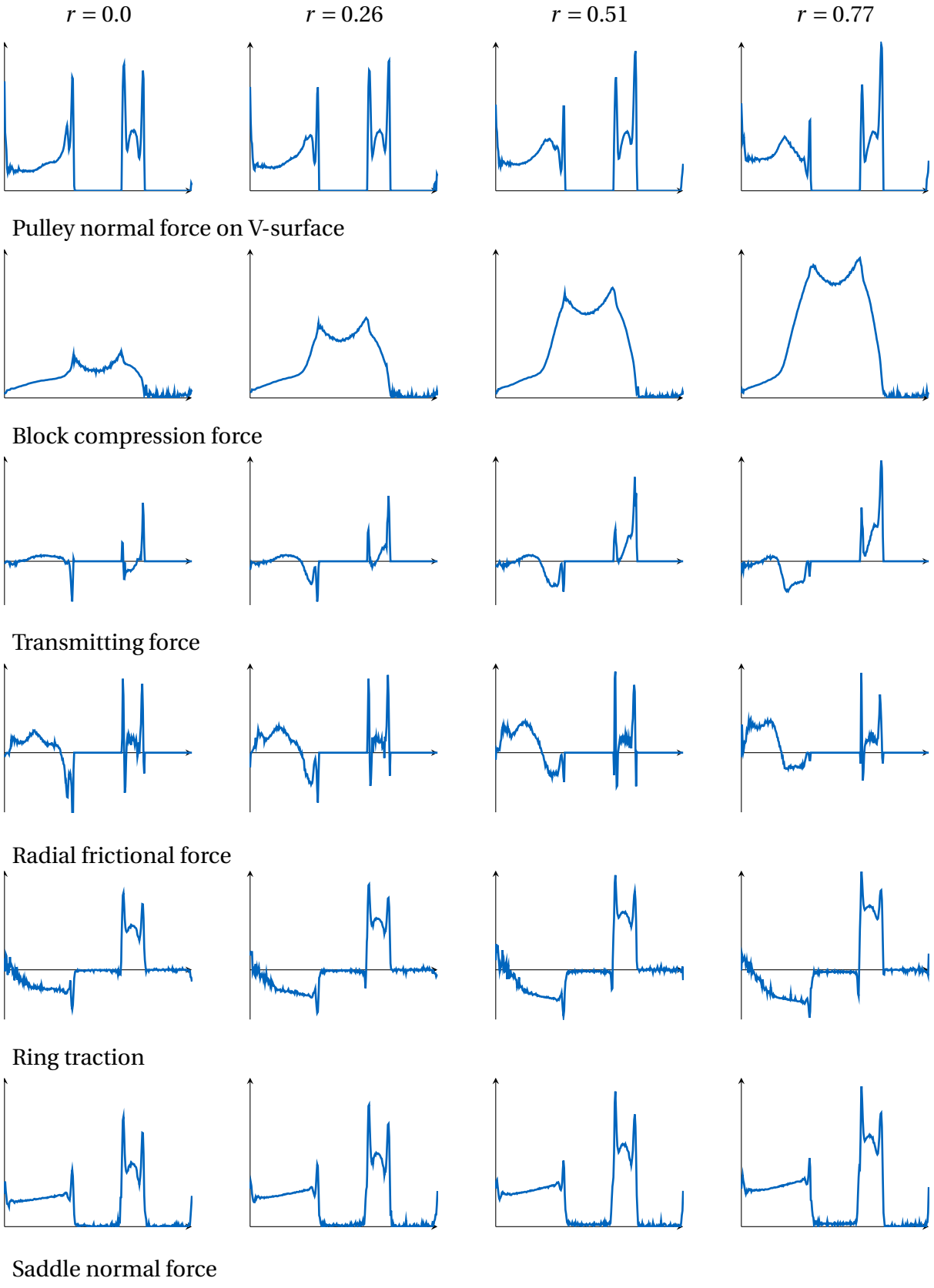

Figure C.6: Local simulation results in overdrive ($i_S \approx 0.5$) which correspond to Figure C.7

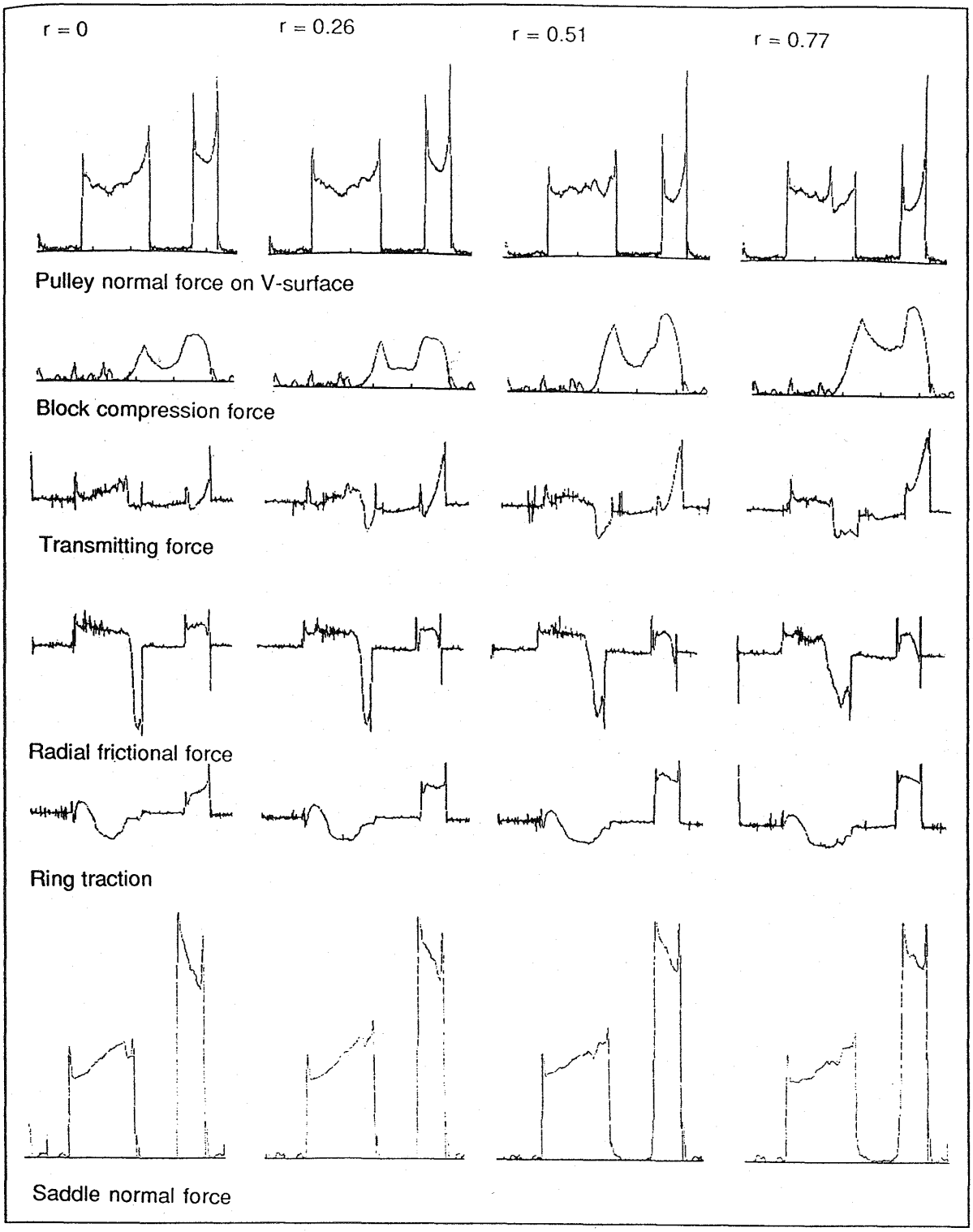

Fig.11 Distribution of the six forces acting on blocks (Speed ratio i = 0.5)

145

Figure C.7: Local measurement results in overdrive from [35, p. 145]

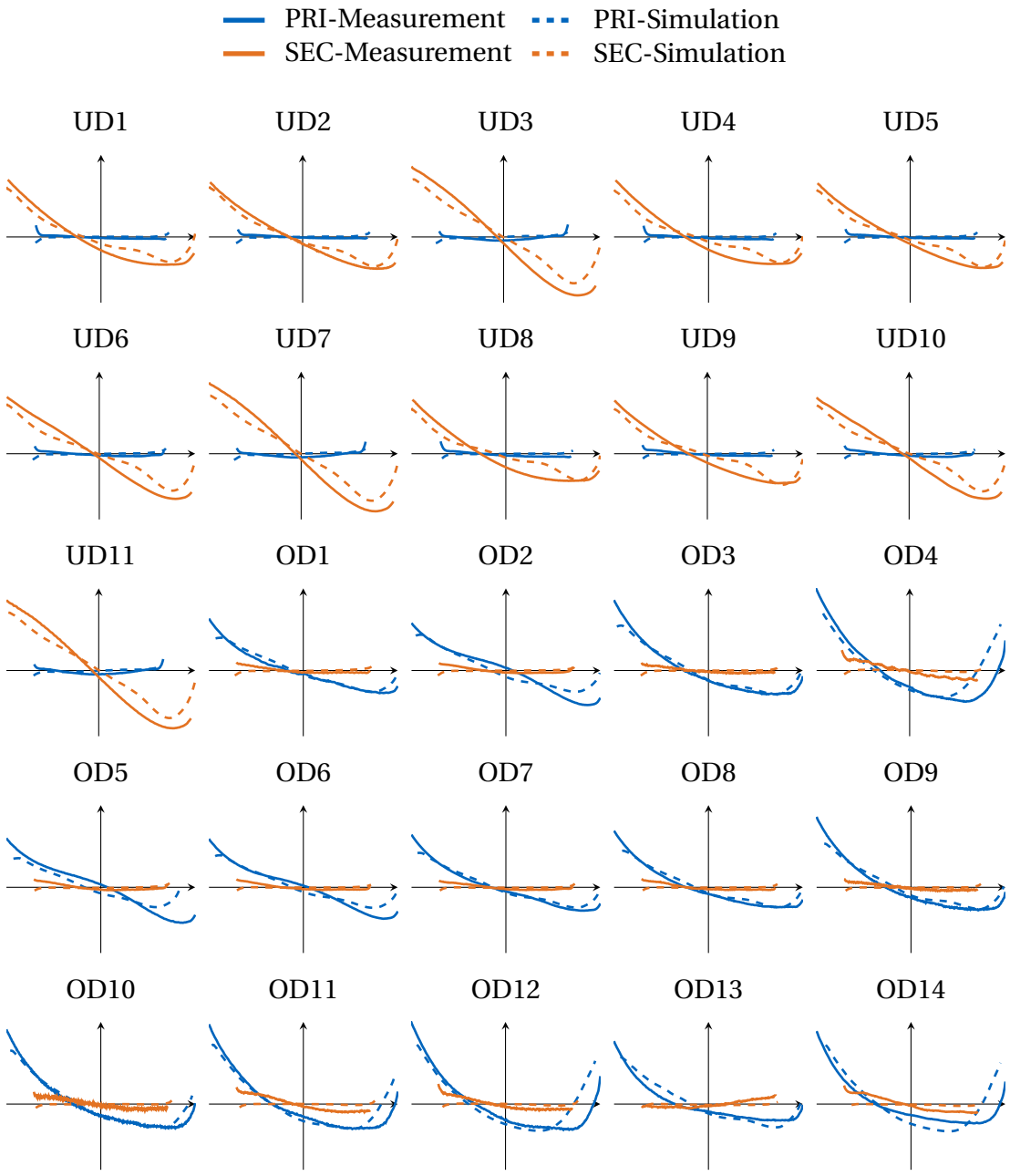

Figure C.8: Validation for arc kinematics of the cases in Table 5.2 for spiral running. Every ordinate is scaled linearly between $0.5\mathrm{mm}$ and $-0.4\mathrm{mm}$. Measurements were made available by BTT.

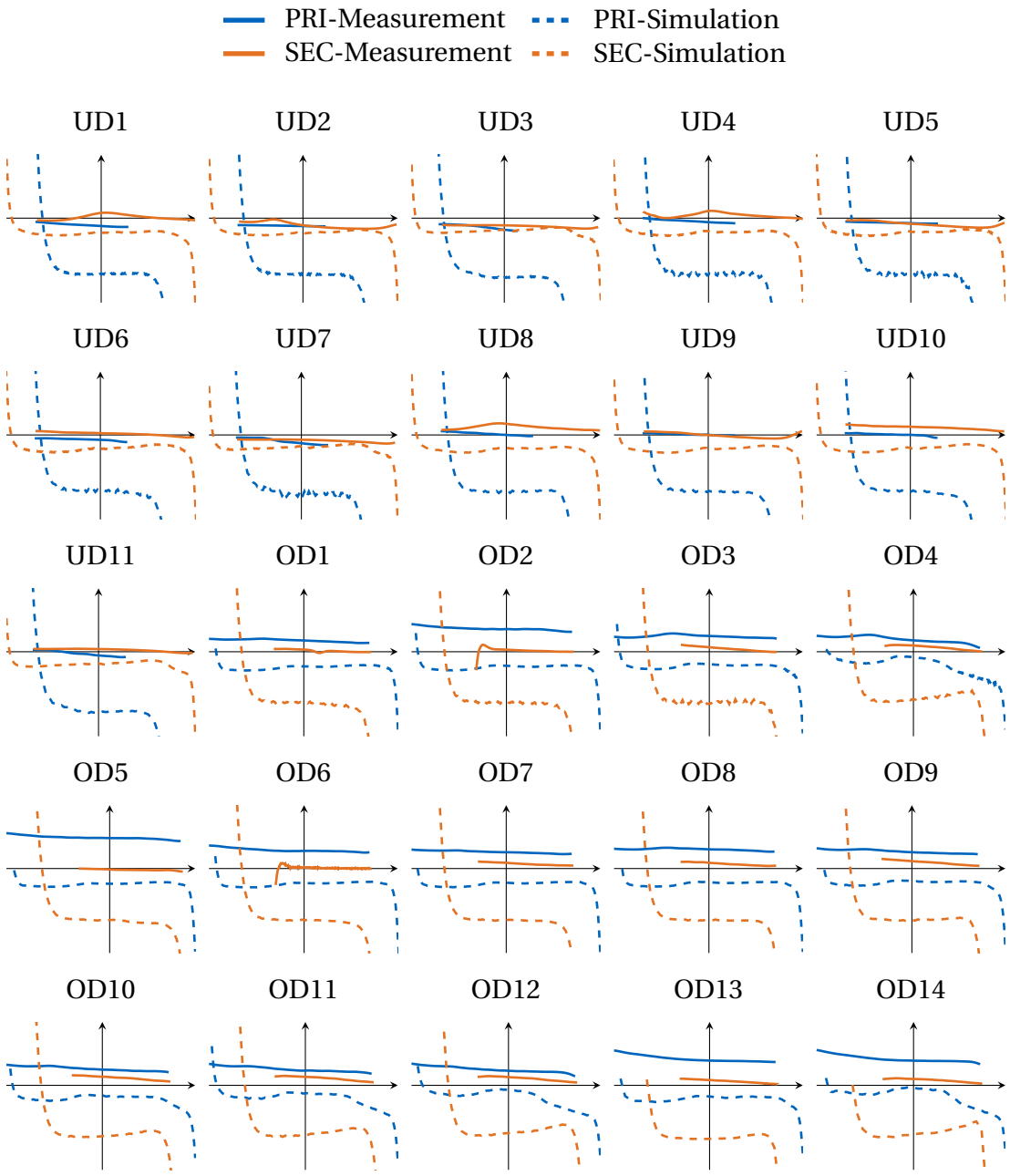

Figure C.9: Validation for arc kinematics of the cases in Table 5.2 for element-sheave pitch. Every ordinate is scaled linearly between $3°$ and $-4°$. Measurements were made available by BTT.

Bibliography

[1] Vincent Acary and Bernard Brogliato. *Numerical Methods for Nonsmooth Dynamical Systems: Applications in Mechanics and Electronics*. Springer, 2008. 529 pp. ISBN: 9783540753926.

[2] Sam Akehurst et al. “Modelling of loss mechanisms in a pushing metal V-belt continuously variable transmission. Part 1: Torque losses due to band friction”. In: *Proceedings of the Institution of Mechanical Engineers, Part D: Journal of Automobile Engineering* 218.11 (Nov. 1, 2004), pp. 1269–1281. ISSN: 0954-4070, 2041-2991. DOI: 10.1243/0954407042580020.

[3] Sam Akehurst et al. “Modelling of loss mechanisms in a pushing metal V-belt continuously variable transmission: Part 2: Pulley deflection losses and total torque loss validation”. In: *Proceedings of the Institution of Mechanical Engineers, Part D: Journal of Automobile Engineering* 218.11 (Nov. 1, 2004), pp. 1283–1293. ISSN: 0954-4070, 2041-2991. DOI: 10.1243/0954407042580101.

[4] Sam Akehurst et al. “Modelling of loss mechanisms in a pushing metal V-belt continuously variable transmission. Part 3: Belt slip losses”. In: *Proceedings of the Institution of Mechanical Engineers, Part D: Journal of Automobile Engineering* 218.11 (Nov. 1, 2004), pp. 1295–1306. ISSN: 0954-4070, 2041-2991. DOI: 10.1243/0954407042580002.

[5] Richard Benson and John D’Errico. “The Deflection of an Elastic Web Wrapped Around a Surface of Revolution”. In: *Journal of Structural Mechanics* 19.4 (1991), pp. 457–476.

[6] Markus Bullinger. “Dynamik von Umschlingungsgetrieben mit Schubgliederband”. Dissertation. München: Technische Universität München, 2005.

[7] Giuseppe Carbone, Luigi Mangialardi, and George Mantriota. “The influence of pulley deformations on the shifting mechanism of metal belt CVT”. In: *Journal of mechanical design* 127.1 (2005), pp. 103–113.

[8] Giuseppe Carbone et al. “CVT dynamics: Theory and experiments”. In: *Mechanism and Machine Theory* 42.4 (2007), pp. 409–428.

[9] Thomas Cebulla. “Spatial Dynamics of Pushbelt CVTs: Model Enhancements to a Non-smooth Flexible Multibody System”. Dissertation. München: Technische Universität München, 2014.

[10] Thomas Cebulla and Thorsten Schindler. “Application of Cosserat Rods in the Nonsmooth Spatial Simulation of Pushbelt CVTs”. In: *Preparation* (2015).

[11] Thomas Cebulla et al. *Spatial Dynamics of Pushbelt CVTs: Model Enhancements*. SAE Technical Paper 2012-01-0307. Warrendale, PA: SAE International, Apr. 16, 2012.

[12] Tim Davis. *Direct Methods for Sparse Linear Systems*. Fundamentals of Algorithms. Society for Industrial and Applied Mathematics, Jan. 1, 2006. 228 pp. ISBN: 978-0-89871-613-9.

[13] Otto Dittrich. "Theorie des Umschlingungstriebes mit keilförmigen Reibscheibenflanken". Dissertation. Karlsruhe: Technische Hochschule Karlsruhe, 1953.

[14] Jack Dongarra et al. *A sparse matrix library in C++ for high performance architectures*. 1994.

[15] drivelinenews. *Push Belt CVT | DrivelineNEWS.com*. PUSH BELT CVT (HD). 2015. URL: http://drivelinenews.com/videos/push-belt/?HD=1 (visited on 01/16/2015).

[16] Martin Egger. "Laufverhalten von Flachbändern". In: *Verlag Stahleisen GmbH, Düsseldorf* (2008).

[17] *EN | Bosch Continuously Variable Transmission*. In collab. with Bosch Mobility Solutions. Aug. 7, 2013. URL: https://www.youtube.com/watch?v=dp8lHBDFhpo&feature=youtube_gdata_player (visited on 01/15/2015).

[18] Johann Albert Eytelwein. *Handbuch der Statik fester Körper; mit vorzüglicher Rücksicht auf ihre Anwendung in der Architektur*. 1st ed. Vol. 2. 3 vols. Berlin, 1808. 454 pp.

[19] Zang Faye and Wu Zhihong. "Control study on the CVT metal V-belt's axial-misalignment of car". In: *2009 IEEE Intelligent Vehicles Symposium*. 2009 IEEE Intelligent Vehicles Symposium. June 2009, pp. 1389–1393. DOI: 10.1109/IVS.2009.5164488.

[20] Martin Förg. "Mehrkörpersysteme mit mengenwertigen Kraftgesetzen: Theorie und Numerik". Dissertation. VDI-Verlag, 2007.

[21] Martin Förg et al. *MBSim - Multi-Body Simulation Software*. MBSim is a multi-body simulation software. 2015. URL: https://github.com/mbsim-env (visited on 05/07/2015).

[22] Toru Fujii, Takemasa Kurokawa, and Shigeru Kanehara. *A study of a metal pushing V-belt type CVT-part 1: relation between transmitted torque and pulley thrust*. SAE Technical Paper, 1993.

[23] Toru Fujii, Takemasa Kurokawa, and Shigeru Kanehara. *A study of a metal pushing v-belt type CVT-Part 2: compression force between metal blocks and ring tension*. SAE Technical Paper, 1993.

[24] Kilian Funk. *Simulation eindimensionaler Kontinua mit Unstetigkeiten*. VDI-Verlag, 2004.

[25] Thomas Geier. "Dynamics of Push Belt CVTs". Dissertation. München: Technische Universität München, 2007.

[26] Göran Gerbert. *Influence of band friction on metal V-belt mechanics*. Chalmers University of technology, Division of machine elements, 1985.

[27] Christoph Glocker. *Dynamik von Starrkörpersystemen mit Reibung und Stößen*. Als Ms. gedr. Verein Deutscher Ingenieure: [Fortschrittberichte VDI / 18] ; 182. Düsseldorf: VDI-Verl., 1995. VI, 220 S. : graph. Darst. ISBN: 3-18-318218-1.

[28] Kilian Grundl and Thorsten Schindler. "ALE beam using reference dynamics". In: *Preparation* (2015).

[29] Kilian Grundl et al. “The Maxwell-Contact”. In: *PAMM* 12.1 (2012), pp. 73–74. ISSN: 1617-7061. DOI: 10.1002/pamm.201210028.

[30] T. IDE, A. UDAGAWA, and R. KATAOKA. “Simulation Approach to the Effect of the Ratio Changing Speed of a Metal V-Belt CVT on the Vehicle Response”. In: *Vehicle System Dynamics* 24.4 (June 1, 1995), pp. 377–388. ISSN: 0042-3114. DOI: 10.1080/00423119508969098.

[31] Sebastian Idler. *Die Fresstragfähigkeit stufenloser Umschlingungsgetriebe*. 1. Aufl. Ingenieurwissenschaften. München: Verl. Dr. Hut, 2014. XII, 146 S. ISBN: 978-3-8439-1824-4.

[32] Hans Irschik and Helmut Holl. “The equations of Lagrange written for a non-material volume”. In: *Acta Mechanica* 153.3 (2002), pp. 231–248.

[33] Gordan Jelenić and Miran Saje. “A kinematically exact space finite strain beam model - finite element formulation by generalized virtual work principle”. In: *Computer Methods in Applied Mechanics and Engineering* 120.1 (1995), pp. 131–161.

[34] J. Ji et al. “Power transmission dynamics in micro and macro slip regions for a metal v-belt continuously variable transmission under external vibrations”. In: *International Journal of Automotive Technology* 15.7 (2014), pp. 1119–1128.

[35] Shigeru Kanehara, Toru Fujii, and Takashi Kitagawa. *A Study on a Metal Pushing V-Belt Type CVT (Part 3: What Forces Act on Metal Blocks?)* SAE Technical Paper, 1994.

[36] Takashi Kitagawa, Toru Fujii, and Shigeru Kanehara. *A Study on a metal pushing V-Belt Type CVT (Part 4: Forces act on Metal Blocks when the Speed Ratio is changing)*. SAE Technical Paper, 1995.

[37] Shinya Kuwabara, Toru Fujii, and Shigeru Kanehara. “Study on a metal pushing V-belt type CVT: band tension and load distribution in steel rings”. In: *JSAE Review* 20.1 (Jan. 1999), pp. 55–60. ISSN: 0389-4304. DOI: 10.1016/S0389-4304(98)00040-X.

[38] Holger Lang, Joachim Linn, and Martin Arnold. “Multi-body dynamics simulation of geometrically exact Cosserat rods”. In: *Multibody System Dynamics* 25.3 (Mar. 1, 2011), pp. 285–312. ISSN: 1384-5640, 1573-272X. DOI: 10.1007/s11044-010-9223-x.

[39] Wolfram Lebrecht. *Dynamische Effekte bei CVT-Umschlingungsgetrieben*. Als Ms. gedr. Fortschritt-Berichte VDI : Reihe 12, Verkehrstechnik/Fahrzeugtechnik ; 637. Düsseldorf: VDI-Verl., 2007. XI, 143 S. ISBN: 978-3-18-363712-6.

[40] HoYoung Lee et al. *A Study on Clamping Force Control in Pulley of CVT for Fuel Efficiency*. SAE Technical Paper, 2014.

[41] Remco Leine and Tom Windandy. “Nonexpansivity of the Newton’s Cradle Impact Law”. 86th Annual Meeting of the International Association of Applied Mathematics and Mechanics. Lecce, Iatly, Mar. 26, 2015.

[42] George Martine, Alex Marshall, and UNFPA. *State of world population 2007: unleashing the potential of urban growth*. 2007. URL: http://www.bvsde.paho.org/bvsacd/cd65/sowp2007/sowp2007.html (visited on 04/23/2015).

[43] MATLAB. *8.4.0.150421 (R2014b)*. Natick, Massachusetts: The MathWorks Inc., 2014.

[44] Erik van der Noll et al. “Geräuschoptimierung von CVT-Schubgliederbändern”. In: *ATZ - Automobiltechnische Zeitschrift* 117.2 (Jan. 15, 2015), pp. 56–61. ISSN: 0001-2785, 2192-8800. DOI: 10.1007/s35148-015-0382-1.

[45] Astrid Pechstein and Johannes Gerstmayr. “A Lagrange–Eulerian formulation of an axially moving beam based on the absolute nodal coordinate formulation”. In: *Multibody System Dynamics* 30.3 (2013), pp. 343–358.

[46] Bert Pennings et al. *Van Doorne CVT Fluid Test: A Test Method on Belt-Pulley Level to Select Fluids for Push Belt CVT Applications*. SAE Technical Paper 2003-01-3253. Warrendale, PA: SAE International, Oct. 27, 2003.

[47] Les Piegl and Wayne Tiller. “The NURBS book. 1997”. In: *Monographs in Visual Communication* (1997).

[48] Toshihiro Saito. “Development of Metal Pushing V-Belt Stress Simulation for CVT”. In: *VDI BERICHTE* 1709 (2002), pp. 371–382.

[49] Toshihiro Saito and Koji Miyamoto. “Application of Technique for Prediction of Stress in Elements of Metal Pushing V-belt by Simulation of Dynamic Behavior, Paper”. In: *Transmission and Driveline 2006*. SAE 2006 World Congress. Detroit, 2006, pp. 227–233. ISBN: 978-0-7680-1736-6.

[50] Toshihiro Saito, Koji Miyamoto, and Tetsuhiko Kajiwara. *Study of Effect of CVT Pulleys on Strength and Transmission Efficiency of Metal Pushing V-belts*. SAE Technical Paper 2011-01-1426. Warrendale, PA: SAE International, Apr. 12, 2011.

[51] Heiko Sattler. “Stationäres Betriebsverhalten stufenlos verstellbarer Metallumschlingungsgetriebe”. PhD thesis. Universität Hannover, 1999.

[52] Uwe Schäfer. *Das lineare Komplementaritätsproblem: eine Einführung*. Springer-Verlag, 2008.

[53] Werner Schiehlen. “Multibody System Dynamics: Roots and Perspectives”. In: *Multibody System Dynamics* 1.2 (June 1, 1997), pp. 149–188. ISSN: 1384-5640, 1573-272X. DOI: 10.1023/A:1009745432698.

[54] Thorsten Schindler. “Spatial Dynamics of Pushbelt CVTs”. Dissertation. München: Technische Universität München, 2010.

[55] Thorsten Schindler et al. “Analysing dynamical phenomenons: Introduction to MBSim”. In: *The 1st Joint International Conference on Multibody System Dynamics, Lappeenranta, Finland* (2010).

[56] Thorsten Schindler et al. “Dynamics of pushbelt CVTs”. In: *VDI BERICHTE* 1997 (2007), p. 389.

[57] Thorsten Schindler et al. “Spatial simulation of pushbelt CVTs with time-stepping schemes”. In: *Applied Numerical Mathematics*. Selected Papers from NUMDIFF-12 62.10 (Oct. 2012), pp. 1515–1530. ISSN: 0168-9274. DOI: 10.1016/j.apnum.2012.06.022.

[58] Ahmed A. Shabana. *Dynamics of multibody systems*. 3rd ed. Cambridge ; New York: Cambridge University Press, 2005. 374 pp. ISBN: 0521850118.

[59] Ahmed A. Shabana. “Flexible Multibody Dynamics: Review of Past and Recent Developments”. In: *Multibody System Dynamics* 1.2 (June 1, 1997), pp. 189–222. ISSN: 1384-5640, 1573-272X. DOI: 10.1023/A:1009773505418.

[60] Hirofumi Shimizu et al. *Development of 3-D Simulation for Analyzing the Dynamic Behavior of a Metal Pushing V-Belt for Cvts*. SAE Technical Paper 2000-01-0828. Warrendale, PA: SAE International, Mar. 6, 2000.

[61] Friedrich W. Simonis. “Theorie der Umschlingungsgetriebe mit keilförmigen Umlaufflächen”. In: *Stufenlos verstellbare mechanische Getriebe*. Springer Berlin Heidelberg, Jan. 1, 1959, pp. 130–134. ISBN: 978-3-642-47373-9, 978-3-642-47371-5.

[62] Sjoerd W. H. Simons et al. “Shift dynamics modelling for optimisation of variator slip control in a pushbelt CVT”. In: *International Journal of Vehicle Design* 48.1 (2008), pp. 45–64.

[63] Francis van der Sluis, Erik van der Noll, and Hendrik de Leeuw. “Key Technologies of the Pushbelt CVT”. In: *target* 25 (2013), p. 50.

[64] Nilabh Srivastava. “Modeling and simulation of friction-limited continuously variable transmissions”. PhD thesis. United States – South Carolina: Clemson University, 2006. 329 pp.

[65] Nilabh Srivastava and Imtiaz Haque. “A review on belt and chain continuously variable transmissions (CVT): Dynamics and control”. In: *Mechanism and Machine Theory* 44.1 (Jan. 2009), pp. 19–41. ISSN: 0094-114X. DOI: 10.1016/j.mechmachtheory.2008.06.007.

[66] Nilabh Srivastava and Imtiaz Ul-Haque. “On the transient dynamics of a metal pushing V-belt CVT at high speeds”. In: *International journal of vehicle design* 37.1 (2005), pp. 46–66.

[67] Nilabh Srivastava and Imtiaz Haque. “Transient dynamics of the metal V-belt CVT: Effects of pulley flexibility and friction characteristic”. In: *Journal of computational and nonlinear dynamics* 2.1 (2007), pp. 86–97.

[68] Jürgen Srnik. *Dynamik von CVT-Keilkettengetrieben*. Als Ms. gedr. Verein Deutscher Ingenieure: [Fortschrittberichte VDI / 12] ; 372. Düsseldorf: VDI-Verl., 1999. XII, 148 S. : Ill., graph. Darst. ISBN: 3-18-337212-6.

[69] Armin Sue. “Betriebsverhalten stufenloser Umschlingungsgetriebe unter Einfluss von Kippspiel und Verformungen”. PhD thesis. Hannover: Universität Hannover, 2003.

[70] D. C. Sun. “Performance Analysis of a Variable Speed-Ratio Metal V-Belt Drive”. In: *Journal of Mechanisms Transmissions and Automation in Design* 110.4 (1988), p. 472. ISSN: 07380666. DOI: 10.1115/1.3258947.

[71] Heinz Ulbrich. *Maschinendynamik*. Auflage: 1996. Stuttgart: Teubner Verlag, Jan. 1, 1996. 307 pp. ISBN: 9783519032335.

[72] Michael Ulbrich. “Nonsmooth Newton-like methods for variational inequalities and constrained optimization problems in function spaces”. PhD thesis. Habilitation thesis, Fakultät für Mathematik, Technische Universität München, 2002.

[73] Jacobus Van Rooij and Willy Schaerlaeckens. “Kräfte und Wirkungsgrad beim Schubgliederband, Teil 1: Allgemeine Kräftebetrachtungen”. In: *Antriebstechnik* 32 (1993), pp. 55–58.

[74] Jacobus Van Rooij and Willy Schaerlaeckens. “Kräfte und Wirkungsgrad beim Schubgliederband, Teil 2: Im Band Auftretende Kräfte”. In: *Antriebstechnik* 32 (1993).

[75] Jacobus Van Rooij and Willy Schaerlaeckens. “Kräfte und Wirkungsgrade beim Schubgliederband, Teil 3: Leistungsverluste im Schubgliederband und CVT-Getriebe”. In: *Antriebstechnik* 32.10 (1993), pp. 83–86.

[76] Arie van der Velde. “Modeling of counter measures”. Internal Meeting. Tilburg, Mar. 14, 2013.

[77] Zhan Wang. “A Framework for Simulating Deformable Bodies with Complex Geometries in a Multibody System with Sliding Contacts”. Master Thesis. München: Technische Universität München, Mar. 17, 2014.

[78] Roland Zander. *Flexible multi-body systems with set-valued force laws*. Vol. 420. Fortschritt-Berichte VDI: Reihe 20, Rechnerunterstützte Verfahren. Düsseldorf: TU München, 2009. ISBN: 978-3-18-342020-9.